Hemispheric geochemical dichotomy of the mantle is a legacy of austral supercontinent assembly and deep subduction of continental crust

M.G. Jackson[1*], F.A. Macdonald[1*]

[1]Department of Earth Science, University of California, Santa Barbara, 93106, USA
(*corresponding authors: jackson@geol.ucsb.edu, francism@ucsb.edu)

Abstract. Oceanic hotspots with extreme enriched mantle radiogenic isotopic signatures—including high $^{87}Sr/^{86}Sr$ and low $^{143}Nd/^{144}Nd$ indicative of ancient subduction of continental crust—are restricted to the southern hemispheric mantle. However, the mechanisms responsible for concentrating subducted continental crust in the austral mantle are unknown. We show subduction of sediments and subduction eroded material, and lower continental crust delamination, cannot generate this spatially coherent austral domain. However, late Neoproterozoic to Paleozoic continental collisions—associated with the assembly of Gondwana and Pangea—were positioned predominantly in the southern hemisphere during the late Neoproterozoic appearance of widespread continental ultra-high-pressure (UHP, >2.7 gigapascals) metamorphic terranes, which marked the onset of deep subduction of upper continental crust. We propose that deep subduction of upper continental crust at ancient rifted-passive margins during austral supercontinent assembly, from 650-300 Ma, resulted in enhanced upper continental crust delivery into the southern hemisphere mantle. In contrast, EM domains are absent in boreal hotspots, for two reasons. First, continental crust subducted after 300—when the continents drifted into the northern hemisphere—has had insufficient time to return to the surface in plumes feeding northern hemisphere hotspots. Second, before the appearance of continental UHP rocks at 650 Ma, upper continental crust was not subducted to great depths, thus precluding its subduction into the northern hemisphere mantle during the Precambrian when continents may have been located in the northern hemisphere. Our model implies a recent formation of the austral EM domain, explains the geochemical dichotomy between austral and boreal hotspots, and may explain why austral hotspots outnumber boreal hotspots.

Introduction

Ocean island basalts (OIB) erupted at hotspots, like Hawaii, reveal the presence of both primordial (1) and ancient subducted continental and oceanic crustal (2,3) reservoirs in the deep mantle (4,5). Early work demonstrated that the distribution of compositional domains in the mantle is not random: Hart (6) showed that a suite of hotspots located primarily in the southern hemisphere exhibit enriched mantle (EM) signatures, including anomalously high $^{87}Sr/^{86}Sr$, that are largely absent in northern hemisphere hotspots. Using radiogenic isotopes, he suggested the presence of a large-scale EM reservoir centered in the southern hemispheric mantle beneath the Atlantic, Pacific and Indian oceans that supplies southern hemisphere hotspots. Called the Dupal (*Dup*ré+*Al*lègre) anomaly (6,7), this southern hemispheric feature is the most geographically widespread geochemical domain in the Earth's deep mantle (8). In spite of its geochemical and geographic prominence, and potential as a tracer for mantle dynamics, the origin of the Dupal mantle domain remains a mystery (6-12).

During Gondwana-Pangea supercontinent assembly from ~650-300 Ma, the continents were located primarily in the southern hemisphere. The spatial coincidence of the Dupal and Gondwana-Pangea was previously identified (6, 10), but Hart (6) noted a potential problem with linking Gondwana-Pangea assembly to the formation of the Dupal: prior to southern hemisphere Gondwana-Pangea, the continents and regions of supercontinent assembly were periodically located in the northern hemisphere over geologic time (13). Therefore, an origin of the Dupal via subduction of continental crust would predict signatures of continental crust recycling in both southern *and* northern hemisphere hotspots, which is not observed.

A second issue that arises with a southern hemisphere Gondwana-Pangea assembly model for the Dupal domain is that it fails to account for the fact that the continents drifted steadily into the northern hemisphere from 300 Ma until present. At face value, this model would predict that EM domains should be visible in the radiogenic isotopic record of northern hemisphere hotspot basalts, but this is not observed. Thus, if southern hemisphere Gondwana-Pangea assembly generated the Dupal domain in the southern hemisphere from 650 to 300 Ma, a key question is why EM domains were not created in the northern hemisphere during continental collisions that occurred as continents drifted northward from 300 Ma to the present day.

In order to resolve these outstanding questions, we refine the Gondwana-Pangea assembly hypothesis for Dupal domain formation to incorporate the temporal coincidence of the appearance of low temperature/pressure subduction in the late Neoproterozoic (14)—linked to the onset of deep subduction of silicic upper continental crust (15)—with the southern hemisphere positioning of continents during Gondwana-Pangea assembly. Given available data for both continental ultra-high-pressure (UHP, defined by rocks exceeding pressures of 2.7 GPa, marking the presence of coesite or equivalent) metamorphic rocks, the first appearance of UHP metamorphic rocks derived from *continental* protoliths is at 650 Ma (14), and subsequent to 650 Ma continental UHP rocks became widespread. (Note that rare occurrences of *oceanic* UHP rocks are identified prior to the first appearance of continental UHP rocks, and oceanic UHP rocks became widespread after 650 Ma). There is no record of subduction of continental rock to UHP depths—and thus no record of deep subduction of rocks with continental crust composition—before 650 Ma, consistent with prior suggestions that silicic continental crust subduction was rare prior to the late Neoproterozoic (15,16). If deep subduction of upper continental crust is required to generate EM domains sampled by hotspots, a hypothesis that we explore in the paper, then the late Neoproterozoic onset of deep continental crust subduction means that earlier episodes of continental assembly and subduction—which occurred prior to

650 Ma when continents were also in the northern hemisphere—did not contribute EM domains to the mantle. Instead, we suggest that the Dupal domain formed after the late Neoproterozoic appearance of continental UHP metamorphism—the product of deep subduction of upper continental crust—when the continents were located in the southern hemisphere. Additionally, we show that continental crust subducted in the past 300 Ma has had insufficient time to be recycled from subduction zones, through the mantle, and into the sources of hotspots. Finally, we examine how focused subduction of continental crust in the southern hemisphere from ~650-300 Ma may give rise to greater austral hemisphere radiogenic heat production, which may explain the greater number of hotspots, and greater overall hotspot buoyancy flux, in the southern hemisphere relative to northern hemisphere. A key implication of our hypothesis is that EM domains are young, and formed by recent (<650 Ma) subduction of ancient continental crust.

Results and Discussion

To address the long-standing problem of the origin of the Dupal domain, we examine a geochemical database of hotspots lavas from the 46 oceanic hotspots that have been geochemically characterized. The geochemical database is compiled in Jackson et al. (12) (Figs. 1 and 2; Dataset S1), and we use the lowest $^{143}Nd/^{144}Nd$ at each oceanic hotspot (Methods) to identify spatial patterns in the distribution of EM domains sampled by hotspots globally. We compare these spatial patterns in hotspot geochemistry with the paleogeography of continents over the past 1000 Ma, the paleogeography of subduction locations of ancient rifted continental passive margins (i.e., loci where continental crust was subducted into the mantle in a manner analogous to the Cenozoic Himalayan collision), and the paleogeography of continental low temperature/high pressure terranes (14) (including UHP terranes) that introduced continental material into the mantle. A full description of each of these parameters is provided in Methods.

Below we propose that the primary path for the delivery of continental crust to the mantle is through the deep subduction of formerly rifted passive margins during arc-continent and continent-continent collisions. Sometime during collisional metamorphism, crust on the lower plate of the collision will detach or break-off (Fig. 3). This crust includes upper and lower continental crust, oceanic crust, transitional crust located between oceanic and continental crust (including significant mafic material), and overlying metamorphosed sediments. As discussed below, some of this crust will enter the mantle and some will be relaminated to the upper plate (17,18). Below we show that, from the late Neoproterozoic to the Paleozoic, continental assembly occurred in the southern hemisphere during onset of deep continental crust subduction, which was made possible by onset of a global late Neoproterozoic transition from shallow to deep slab-breakoff. The coincident timing of continental geography and a global tectonic transition set the stage for focused deep subduction of a formerly rifted passive margins—subducted at continent-continent and arc-continent collision zones—into the southern hemisphere mantle from the late Neoproterozoic through the Paleozoic.

A hemispheric dichotomy in hotspot geochemistry and geographic distribution. The global distribution of the lowest $^{143}Nd/^{144}Nd$ identified in lavas at each of the geochemially characterized oceanic hotspots is shown in Figs. 1 and 2. The advected conduit bases of 11 hotspots located between the deep southern hemisphere and the equator have more geochemically enriched (lower) $^{143}Nd/^{144}Nd$ than any northern hemisphere hotspot (Fig. 2). These 11 geochemically enriched hotspots, here referred to as “EM hotspots”, all have at least one lava with $^{143}Nd/^{144}Nd < 0.512600$. This $^{143}Nd/^{144}Nd$ value is not an arbitrary threshold: it is the $^{143}Nd/^{144}Nd$ value below which there are no northern hemisphere examples (i.e., there are no lavas from northern hemisphere hotspots with $^{143}Nd/^{144}Nd < 0.512600$). Because plume conduits tilt as they up-well (Methods), the northernmost EM hotspot, Hawaii, has a calculated conduit base located near the equator (Dataset S1; Figs. 1 and 2), which does not influence the outcome of the study except to say that the Dupal domain exists primarily in the southern hemisphere and extends to equatorial latitudes. This is similar to the geographic distribution of the "Dupal hotspots" in Hart (1984) (6), who noted that such hotpots tend to be located in the southern hemisphere. Therefore, acknowledging Hart's (6) discovery of a geochemically-enriched southern hemisphere domain, which we identify here using $^{143}Nd/^{144}Nd$, we preserve the original Dupal terminology when referring to the austral mantle EM domain. While the most geochemically enriched ($^{143}Nd/^{144}Nd < 0.512600$) hotspots are in the southern hemisphere, not all southern hemisphere hotspots are geochemically enriched (Fig. 2), indicating the presence of geochemical heterogeneity within the Dupal domain (12).

It is worth noting that our observation of the Dupal domain relies on a geochemical database that includes *all* oceanic hotspots that have been geochemically characterized for $^{143}Nd/^{144}Nd$. As a result, our conclusions differ from a recent study by Doucet et al. (19), who argued against the presence of a geochemically distinct enriched mantle domain in the southern hemisphere mantle. They arrived at this conclusion by excluding hotspots they did not consider be plume related because they 1) are located near trenches, 2) have short-lived hotspot tracks, 3) are not associated with a large igneous province, and 4) exhibit only low $^{3}He/^{4}He$. In contrast, we argue that surface physiographic expressions of hotspots (i.e., hotspot location relative to trenches, longevity of hotspot tracks, and hotspot association with large igneous provinces) and hotspot geochemistry (low hotspot $^{3}He/^{4}He$) cannot be used to reliably exclude a plume origin for such hotspots (12). Instead, we posit that seismic methods are better suited for determining whether a plume exists beneath a hotspot: at least 28 hotspots have been found to be associated with plumes detected using seismic methods (20,21), including key Dupal hotspots excluded by Doucet et al. (19). Furthermore, plumes beneath some hotspots may be undetected because of the resolution of existing global tomographic models and limited data coverage (12). For example, the Yellowstone plume was not detected in global seismic models, but was detected in a regional study that employed the high-density US array (22), suggesting that we cannot exclude the presence of a plume beneath a hotspot simply because it remains undetected in existing (relatively low resolution) global seismic models. Therefore, we refrain from excluding oceanic hotspots from our treatment, and this approach leads us to observe a clear hemispheric dichotomy in the distribution of EM domains.

Further highlighting the northern versus southern hemisphere dichotomy among global hotspots, there are twice as many southern hemisphere hotspots as northern hemisphere hotspots (Fig. 4): the analysis shown in Fig. 4 includes both oceanic *and* continental hotspots (i.e., all 47 oceanic and 11 continental hotspots shown in Dataset S1). If only oceanic hotspots are counted, there are still more than twice as many southern hemisphere hotspots as northern hemisphere hotspots. However, the mechanism responsible for this hemispheric dichotomy in hotspot distribution is unknown (12).

Flux and composition of continental crust into the mantle and Dupal formation. The EM domain, sampled by plume-fed OIB, is widely suggested to form by a contribution from subducted continental crust. However, the exact type of continental material that contributes to the EM mantle—upper continental crust, lower continental crust, or sediment derived from continental crust—is not well constrained (2,23-26). Below we discuss the different mechanisms for introducing continental crust into the mantle and how the geographically restricted distribution of the Dupal domain constrains the origin, and type, of continental crust material that makes up the EM domain.

As outlined in Stern and Scholl (27), continental crust is subducted in one of four principal ways: 1) sediment subduction results in upper continental crust loss, 2) subduction erosion removes upper and lower continental crust, 3) lower crustal foundering removes lower continental crust only, and 4) wholesale continental crust subduction removes upper and lower continental crust. However, the absolute fluxes of continental crust material into the mantle that result from each of these mechanisms are highly uncertain in the present day, as widely acknowledged in work dedicated to the subjectHacker11_Hacker15_Stern&Scholl10_Clift09 (17,18,27,28). For example, as discussed in Hacker et al. (18), Scholl & von Huene (29) estimated that 95% of subducted sediment is returned to the mantle, but Hacker et al. (17) argue that the low density of sediment will result in most (up to 94%) of the subducted sediment simply being relaminated to the underside of the continental crust. Thus, the relamination mechanism hinders sediment delivery into the convecting mantle. Similarly, subduction erosion also has been argued to be efficient at transporting continental crust into the mantle (27,28), but Hacker et al. (17) argue that, due to having relatively low density, most (up to 82%) of the products of continental crust subduction erosion are simply relaminated onto the underside of the continental crust instead of being returned to the mantle. In summary, the low density of sediment and the products of subduction erosion may result in relamination, which greatly reduces loss of this continental crust-derived material to the mantle (17,18), making sediment subduction and delamination unlikely candidates for efficient continental crust delivery to the Dupal domain.

The conclusion that the EM domain is not generated by subduction of sediment and products of subduction erosion is supported by the restricted geographic pattern of the Dupal domain. Pre-650 Ma subduction zones would have occupied a wide range of latitudes, including the northern hemisphere, so subduction of sediment and products of subduction erosion cannot be responsible for generating EM domains in the mantle. Otherwise, EM domains generated by subduction of sediment and products of subduction erosion would be present at all latitudes, not just the southern hemisphere where the Dupal domain is located. This leads us to conclude that subducted sediment and the products of subduction erosion are not efficiently delivered into the mantle.

It could be argued that more recent subduction of sediment and productions of subduction erosion in the southern hemisphere during the late Neoproterozoic and Paleozoic—when continents and subduction zones were positioned in the southern hemisphere, as discussed below—dominate the deep mantle reservoir of continental crust-derived materials by invoking mantle mixing and stirring: such processes are time dependent, and could greatly attenuate earlier-formed heterogeneities while leaving more recently-formed reservoirs less attenuated. However, the long-term survival of *Hadean* ^{142}Nd, ^{182}W, and ^{129}Xe anomalies identified in modern OIB (1,30,31) suggests that the mantle is not an efficient blender. Therefore, it seems difficult to argue that, once subducted, continental crust and its geochemical signatures are easily attenuated in the mantle over time.

As with subduction of sediments and the products of subduction erosion, the geographic distribution of the Dupal domain can also be used to exclude an origin by lower continental crust delamination. Lower continental crust is widely assumed to be mafic in composition (e.g., (32)) (but see Hacker et al. (17,18) for an argument that most—up to ~80%—of the lower continental crust is silicic). Therefore, in contrast to relamination of low-density sediments and products of subduction erosion, delamination of dense mafic lower continental crust results in continental crust loss to the mantle (e.g., (33,34)). Lower continental crust delamination may have been operating since the Archean (e.g., (35)) and, like subduction zones, the continents have been located over a wide range of latitudes since the Archean, including the northern hemisphere. Therefore, if lower continental crust delamination were responsible for generating EM domains, EM mantle reservoirs would be expected at all latitudes, including outside of the southern hemisphere Dupal domain, but this is not observed. A conclusion of this observation is that delaminated lower continental crust does not generate EM domains. There are several possible reasons why this would be the case. First, it is possible that delaminated mafic lower continental crust is too dense to return to the surface in upwelling plumes that source hotspots. However, if lower continental crust does return to the surface, it is possible that lower continental crust does not have geochemical characteristics necessary to incubate EM domains during long-term storage in the mantle. Alternatively, if lower continental crust is more silicic in composition, as suggested by Hacker et al. (17,18), then lower continental crust may be insufficiently dense to enter the mantle in the first place, so is incapable of generating deep mantle EM domains sourced by plumes.

Nonetheless, positive Eu anomalies (i.e., Eu/Eu*>1; see Fig. S1 for definition) in OIB have been used to argue that lower continental crust, which can have Eu/Eu*>1, contributes to some OIB with EM1 (enriched mantle I) signatures (25,26). However, we find that upper *and* lower continental crustal rocks both exhibit examples where Eu/Eu*>1 (Fig. S1), and thus

Eu/Eu*>1 is not diagnostic of lower continental crust in the mantle sources of OIB. Furthermore, high Eu/Eu* values in OIB may not reflect their mantle sources due to diffusive interaction with plagioclase-rich lithologies in the lower oceanic crust (36) or disequilibrium melting (37), two mechanisms that can impart high Eu/Eu* on OIB without involvement of lower continental crust. Thus, existing geochemical constrains do not require lower continental crust recycling for generation of the EM domain.

Having excluded Dupal domain formation by continental crust delivery to the mantle via lower continental crust delamination, or by subduction of sediments and products of subduction erosion, below we consider a different mode of continental crust delivery to the mantle—wholesale subduction of continental crust during subduction of ancient rifted passive margins during continental collisions—to generate the geographically coherent EM domain that is spatially restricted to the southern hemisphere (6) (Fig. 1).

Continental crust subduction at rifted passive margins and attendant UHP metamorphism. In contrast to subducting sediments and products of subduction erosion, the continental and transitional crust along rifted-passive margins are attached to dense down-going mafic slabs (Fig. 3), which confer greater effective density to the subducting package (i.e., the denser oceanic slab is attached to less dense continental crust, and together they form a package with higher density than upper continental crust alone (16) (Fig. 3). In this way, continental crust—including silicic upper continental crust and transitional crust, where the latter is sandwiched between continental and oceanic crust and is composed of silicic and mafic rocks—can descend into the mantle as long as it is attached to the dense oceanic slab. Once the subducting package reaches the point-of-no-return—a mantle depth below which the silicic portion of continental crust undergoes phase transitions to become denser than ambient mantle (17)—the silicic continental crust will continue to sink, even if it detaches from the down-going slab. However, as discussed below, if the slab detaches from the continental crust *before* reaching the depth of no return, the silicic continental crust will simply rise buoyantly. The feasibility of subduction of silicic upper continental crust compositions to depths deeper than the point of no return has been demonstrated with geodynamic modeling (15,35), which shows that silicic continental crust can achieve densities greater than ambient mantle at the point of no return. In contrast to continental crust attached to down-going slabs at ancient rifted-passive margin settings, sediments and the products of subduction erosion are not attached to a down-going slab, so they are buoyant and simply relaminate and, therefore, are not conveyed to great depths.

Of course, both upper and lower continental crust are attached to the down-going slab and will be subducted together during collision. However, as described above, lower continental crust—which has been delaminated at all latitudes since the Archean (35)—cannot explain formation of the of the geographically restricted Dupal domain. Given that delaminated and subducted lower continental crust should have broadly the same composition, we see no reason why lower continental crust delivered to the mantle during continental subduction would contribute to the Dupal domain when delaminated lower continental crust does not. In short, we do not know the fate of lower continental crust after it enters the mantle, but it is not a good candidate for generating EM domains for reasons described above.

Instead, it is the silicic upper continental portion of the subducted ancient rifted-passive margin that is likely to contribute to Dupal formation. This is supported by geochemical evidence consistent with upper continental crust signatures in the EM mantle domain (24,25). We acknowledge that the origin of the geochemical signatures in EM1 (24) and EM2 (25) previously were attributed to the addition of subducted marine sediments to these mantle sources, but much of the sediment budget in the ocean basins (both terrigenous and marine sediment (38,39)) ultimately derives from upper continental crust, and the geochemical arguments used for evaluating the protolith of the continental material in the EM domains do not uniquely distinguish between a recycled upper continental crust signature derived from subducted sediments and one derived from wholesale subduction of upper continental crust. For example, the slope of the correlation between whole rock $^{87}Sr/^{86}Sr$ and olivine oxygen isotopes provided the strongest argument that the mantle source of Samoan EM2 lavas hosts a component of subducted continental sediment that resided in a marine environment prior to subduction (40), but a new study of $^{87}Sr/^{86}Sr$ and oxygen isotopes olivines from Samoan lavas shows that the slope is consistent with continental crust, with no requirement for a marine influence (41). In short, we see no geochemical hurdles to attributing the continental signatures in the EM mantle domains to upper continental crust subduction.

Continent-continent and arc-continent collision zones are nurseries for continental UHP metamorphic terranes that deliver continental crust to extreme depths, and we argue below that these depths extend beyond the point of no return to the deep mantle. Of course, the observation of UHP metamorphic rocks in continental crust settings only provides evidence of rocks that were exhumed from UHP metamorphic depths, and such rocks do not provide evidence that continental rocks were subducted into the mantle. Nonetheless, there is mounting support for the contention that upper continental crust lithologies are subducted beyond the point of no return during UHP metamorphism (see Stern and Scholl (27) for discussion). Additionally, a growing body of evidence suggests that once silicic upper continental crust reaches depths for UHP metamorphism, not all of it is exhumed: some continues past the depth of no return (15,35). If continental crust subduction of ancient rifted-passive margins (Fig. 3) generated the Dupal domain, a key remaining question is why it is geographically restricted to the southern hemisphere.

Southern hemisphere assembly of Gondwana-Pangea during the late Neoproterozoic appearance of continental UHP metamorphic rocks: setting the stage for the Dupal domain.

During the late Neoproterozoic and Paleozoic, geological and paleomagnetic evidence confirm that Gondwana and Pangea were constructed in the southern hemisphere (42,43) (Figs. 1 and 5; Fig. S2), consistent with prior suggestions that the geographically restricted Dupal domain might somehow relate to Gondwana's southern hemisphere position (6,10). During this period, the continents moved deep into the southern hemisphere, and were positioned, on average, south of 15° south latitude (Fig. 5; Dataset S2). This time interval—approximately 650 to 300 Ma—defines a peak in the subduction of ancient rifted-passive margins in Earth history, which was focused in the southern hemisphere (Fig. 5 panel b).

An important question is whether the paleogeography of the continents relative to the paleomagnetic (or spin-axis) reference frame, like that used in Merdith et al. (43), can be used to constrain the latitude of subducted contributions to the mantle. Prior to the Mesozoic, absolute paleogeography is difficult to determine because paleomagnetic data constrains only latitude, not longitude, and because the paleomagnetic reference frame can move relative to a mantle reference frame (i.e., true polar wander). The Neoproterozoic reconstruction of Merdith et al. (43) uses a paleomagnetic reference frame, and relies on geological and kinematic constraints, but is merged into Paleozoic models based on a hybrid mantle reference frame (44,45). A large Paleozoic longitudinal shift in the reference frame is necessary to reconcile these models (43).

Although it would be ideal to use a mantle reference frame, going back to 1000 Ma, to present the Merdith et al. (43) reconstruction, this does not exist. Moreover, there is disagreement whether to use a mantle reference frame with true polar wander around hypothesized fixed LLSVPs (42,46), or if the LLSVPs are mobile on 100 Myr timescales (47). To assess the sensitivity of reference frames on paleolatitude, we compared paleogeographic reconstructions at 100 Myr snapshots in the mantle versus paleomagnetic reference frames in the reconstruction of Torsvik & Cocks (2017) (42), which extends to 600 Ma (Fig. S2). We find that a southern hemisphere dominance of continental latitudes persists in both the paleomagnetic and the modeled mantle reference frame from 600-300 Ma (i.e., the proposed interval of continental crust contribution to the southern hemisphere mantle). Inferring paleolatitudes prior to ~550 Ma is less straightforward because paleomagnetic studies from ca. 582 to 565 Ma rock units have yielded anomalous results (e.g., (48,49)), which have been interpreted to record large-scale true polar wander (e.g., (13,50). However, recent studies suggest that the Ediacaran field was anomalously weak and unstable with high-frequency reversals (e.g, (51,52)). Therefore, a simple interpolation of the paleomagnetic data through this interval (e.g., (43)), with the assumption of no significant true polar wander or difference between paleolatitude in the paleomagnetic and mantle reference frames (Fig. S2), appears to be the most parsimonious approach, supporting a southern hemisphere positioning of the continents from 650 to 550 Ma (Fig. 5).

The pulse of ancient rifted-passive margin subduction from 650-300 Ma is illustrated in Fig. 5 (panel b), which shows that subduction of these margins occurred overwhelmingly in the southern hemisphere from 650-300 Ma. Critically, this maximum in ancient rifted-passive margin subduction events from 650-300 Ma occurred on the heels of the breakup of Rodinia, a breakup marked by a peak in the generation of rifted-passive margins (Fig. 5), which exposed

Archean and Proterozoic cratonic and transitional crust on margins (53) (Fig. 3). During Gondwana and Pangea construction, many of these ancient rifted-passive margins were on the lower, down-going plate of collisional orogens (see (54)) which provides many examples of Archean to Proterozoic crust along margins on the lower plate during the assembly of Gondwana), setting the stage for their subduction into the mantle during collision. Additionally, UHP metamorphic terranes with continental protoliths—which record continental crust delivery to great depths—can provide long-term records of deep continental subduction; the reconstructed paleolatitude of continental UHP terranes shows that, from at least 600-300 Ma (42) (Fig. S2), and likely back to 650 Ma (43) (Fig. 5), virtually all such terranes were located between the southern hemisphere and the equator. Thus, these terranes were loci of deep continental subduction—where continental crust entered the mantle in the same range of latitudes as the modern Dupal domain (Figs. 1 and 2)—during Gondwana and Pangea supercontinent assembly (42,43) (Fig. 5). Incidentally, it should not be surprising that, from 650-300 Ma, continental UHP and low temperature/high pressure terranes are both concentrated in the southern hemisphere (Fig. 5, panel d) because collisions in which ancient rifted-passive margins are subducted (Fig. 5, panel c)—which were also overwhelmingly located in the southern hemisphere from 650-300 Ma—are loci for high pressure metamorphism of continental crust.

While we propose that the period from 650-300 Ma represents a major episode of upper continental crust subduction in Earth's history, we emphasize that continental subduction of ancient rifted-passive margins prior to 650 Ma—when continents were also in the northern hemisphere—did not efficiently deliver continental material to the mantle: while Precambrian collisional orogens likely occurred over a wide range of latitudes that included the northern hemisphere, these events did not deliver upper continental crust past the point of no return, otherwise they would have also generated EM domains in the northern hemisphere of the Earth's mantle, which is not observed. This hypothesis is supported by observations from the rock record, which shows that continental crust did not reach depths required for UHP metamorphism until the ~650 Ma (i.e., the oldest known UHP metamorphic rock with a continental protolith (14)). This is not a new result: for example, van Hunen and Allen (16) write that, prior to late Neoproterozoic, "continental crust would not reach the depth required to form blueschists and UHP [metamorphic rocks]." The new result here is in showing that the initiation of upper continental crust subduction to mantle depths began when the continents were located in the southern hemisphere—during Gondwana-Pangea assembly—consistent with the southern hemisphere distribution of EM hotspots. Similarly, the *absence* of continental UHP metamorphic terranes in the rock record prior to 650 Ma (14) supports the hypothesis that less subduction of upper continental crust to great depths occurred during the vast Precambrian interval when the continents were located at latitudes that included the northern hemisphere (Fig. 5, panel d), consistent with the absence of EM hotspots in the northern hemisphere (Figs. 1 and 2). The Neoproterozoic transition from shallow to deep slab-breakoff, discussed below, permitted continental protoliths to achieve UHP metamorphic depths for the first time—when the continents and subduction zones were located in the southern hemisphere—which set the stage for formation of the geographically-restricted Dupal domain.

Deep slab-breakoff and the secular cooling of the Earth's interior. At rifted-passive margins, the dense mafic slab is attached to continental crust. Prior to the late Neoproterozoic, rheological weakening of the subducting slab in the higher geothermal gradient of the Precambrian Earth favored shallow slab-breakoff of the denser oceanic lithosphere (15). During this time interval, the dense slab simply detached from down-going continental crust at shallow depths before continental crust could reach UHP conditions (15), and the continental crust did not reach the point of no return (Figs. 3 and 6). Following detachment, the up-dip felsic subduction complex had higher effective buoyancy (Fig. 3), which permitted felsic continental crust to migrate back up the subduction channel (55) before reaching before reaching UHP conditions. This model is consistent with the absence of continental UHP metamorphism (i.e., absence of continental protoliths with pressures >2.7 GPa; Fig. 6) prior to 650 Ma (15,16).

The appearance of widespread continental UHP metamorphism in the late Neoproterozoic is proposed to result from evolution of the style of subduction in response to secular cooling of the Earth's interior: down-going slabs began to break off from the continental crust at greater depths due to a rheological strengthening of the lithosphere as the mantle cooled (Fig. 3) (14,15,56). Because felsic continental crust is attached to the denser down-going slab to greater depths, the up-dip felsic subduction complex could be transported to greater depths (55), permitting generation of continental UHP rocks for the first time (Fig. 6, panel b). While continental crust observed at UHP metamorphic terranes was exhumed, continental crust subducted past the point of no return was delivered into the mantle (15,27,56). From ~650 Ma (i.e., the age of the oldest known UHP metamorphic rock with a continental protolith (14)) to present, zones of continent collision were nurseries for continental UHP metamorphic terranes that enhanced continental crust delivery to mantle depths (but, as discussed below, continental crust subducted from 300 Ma to present has not had sufficient time to cycle back into the sources of hotspots).

While fluxes of continental materials into the mantle are poorly constrained in the present day, the widespread appearance of continental UHP metamorphic terranes by 650 Ma provides evidence that the evolving thermal evolution of the Earth became more conducive to delivery of continental material to great depths (27,56). This rheological transition within the slab—which enabled deeper continental subduction—may not have been abrupt, but could have occurred on a longer timescale (i.e., following Rodinia) and became evident, and widespread, only during abundant continent collisions that occurred in the late Neoproterozoic (14). We propose that deep subduction of ancient rifted-passive margins associated with continent collisions during the southern hemisphere assembly of Gondwana and Pangea was critical for enhancing delivery of continental crust into the austral mantle. Because extensive subduction of ancient rifted-passive margins during collisions from 650-300 Ma (Fig. 5) occurred after the appearance of widespread continental UHP metamorphism, this 350-million-year interval would have had a marked, long-term impact on the geochemistry of the austral mantle because continents and collision zones were dominantly positioned in the southern hemisphere.

Additional evidence for post-650 Ma formation of EM domains. A key implication of our hypothesis is that EM domains were formed by relatively recent (post-650 Ma) subduction of Archean to Proterozoic upper continental crust. If correct, older apparent ages of some EM domains (57) can be explained by recent (post-650 Ma) subduction of ancient rifted Precambrian rifted-passive margins at late Neoproterozoic to Paleozoic continental collision zones. The 2.1 billion-year kimberlite record provides evidence that supports the hypothesis for a late (post-650 Ma) introduction of continentally-derived EM signatures to the mantle. Unlike OIB, which record the geochemistry of the mantle for <200 Ma (the age of the oldest oceanic crust), kimberlites provide a much longer history of the composition of the mantle. For the first 1.9 billion years of the 2.1-billion-year kimberlite record, kimberlites consistently sample a primitive (58) to depleted (59) mantle signal, with no evidence for contribution from a low $^{143}Nd/^{144}Nd$ EM domain.

However, the most recent ~200 Ma of the kimberlite record witnessed the first appearance of EM material (58,59), supporting enhanced late Neoproterozoic to Phanerozoic delivery of continental material to the deep mantle source of kimberlites. This time-resolved geochemical record from kimberlites suggests that transport of continental crust to the mantle prior to the late Neoproterozoic was not efficient compared to the mechanism—deep slab-breakoff and consequent continental subduction—that operated more recently, supporting the hypothesis that EM domains are young and formed during and after the late Proterozoic. Incidentally, the appearance of EM domains in the kimberlite mantle domain at ~200 Ma is consistent with a several-hundred-million-year delay between the late Proterozoic onset of continental crust subduction at collision zones and the appearance of continental crust signatures in modern hotspots fed by upwelling plumes, as we discuss below.

Why continental crust subducted in the northern hemisphere from 300 Ma to present is not sampled by northern hemisphere hotspots. Continental UHP terranes were positioned in the northern hemisphere from 300 Ma to present (Fig. 5, panel c). Similarly, the subduction of ancient rifted-passive margins in the *northern* hemisphere, while relatively insignificant during the late Neoproterozoic and Early Paleozoic, increased from the Late Paleozoic to present as continents moved northward over the past 300 Ma (Fig. 5, panel b). Therefore, a key question is why continental crust subduction from 300 Ma to present did not generate a deep EM domain sampled by northern hemisphere hotspots.

We argue that subduction of continental crust into the northern hemisphere during the last 300 Ma was unlikely to generate extreme EM domains sampled by modern hotspots (12) largely because continental material subducted into the northern hemisphere over the past several hundred million years has not had sufficient time to return to the surface in northern hemisphere mantle plumes. Down-going slabs require ~200 Ma to reach the CMB (44,60), then they reside at the CMB for a period of time, and finally they need 10's to 100 Ma to be transported from the CMB to the near surface in upwelling plumes (46,61). Therefore, northern hemisphere oceanic hotspots do not exhibit geochemical signatures associated with northern hemisphere continental crust subduction that occurred from 300 Ma to present (12).

Continental crust in the austral regions of the Large Low Shear-wave Velocity Provinces gives rise to more radiogenic heating, thereby generating more austral plumes. The distribution of the 11 EM hotspots in the southern hemispheric mantle is not random: all are geographically restricted to the southern hemispheric regions of the two deep mantle Large Low Shear-wave Velocity Provinces (LLSVPs) (Fig. 1). The clear geographic correspondence between LLSVP structures at the bottom of the mantle and EM hotpots at the surface is strong evidence that the material hosting the EM signatures—deeply subducted upper continental crust—resides in the deep mantle LLSVP structures (8,12). If we are to accept that upper continental crust can be transported past the point of no return during low T/P metamorphism recorded at UHP terranes, a clear implication of the geographic link between the Dupal domain and the LLSVPs is that the subducting continental crust enters the deepest mantle after passing the point of no return. How deeply subducted continental crust preferentially enters the LLSVPs, which cover only ~30% of the core-mantle boundary (62), remains a key question.

The composition, temperature, density structure, and origin of the LLSVPs are the subject of intense debate: they may host dense oceanic crust or primordial material, or both, which is consistent with suggestions that the LLSVPs have higher density and distinct chemical makeup (e.g., (62,63,64)). The clear geographic correspondence between EM hotspots and the LLSVPs leads us to argue that the LLSVPs are also host to most of the subducted upper continental crust in the deep mantle. Below we argue that this is a consequence of convection patterns in the mantle.

The global geographic anticorrelation between subduction zone locations and LLSVPs, where no slabs intersect with the LLSVPs (44), suggests that the mantle is dominated by a broad convection pattern with subduction zone downwelling around the LLSVPs and upwelling above the LLSVPs: a consequence of this convection pattern (20,65,66) is that down-going slabs will tend to push deep compositional layers—including subducted continental crust (12)—into the LLSVPs, thereby providing a possible explanation for the link between the Dupal domain and the LLSVPs. Therefore, the geochemical enrichment in the Dupal hotspots—all 11 of which overlie the LLSVPs—is consistent with a model where continental crust subducted into the southern hemisphere mantle was drawn into the nearby (i.e., southern hemispheric) portions of the LLSVPs and then entrained by deep mantle plumes sourcing southern hemisphere hotspots.

Consequently, the southern portions of the LLSVPs may be enriched in heat-producing elements, due to high concentrations of radioactive heat-producing elements (U, Th, K) in continental crust (32). This may give rise to a geodynamic feedback: enhanced continental crust delivery to the southern portions of LLSVPs results in excess austral hemisphere heat production that enhances plume generation in the southern hemisphere, including all of the plumes that source hotspots with the strongest recycled continental crust signatures. Such a model may help to explain the observation that there are twice as many hotspots (both continental and oceanic hotspots) in the southern hemisphere compared to the northern hemisphere (Fig. 4). Consistent with the hypothesis of excess heat flow carried by southern hemisphere plumes, most (64%) of the total global hotspot buoyancy flux (including both oceanic and continental hotspots) is accounted for in hotspots sourced by southern hemisphere conduits, while the summed hotspot buoyancy fluxes in the northern hemisphere is significantly less (36%) (12); if Hawaii is considered as a southern hemisphere plume—consistent with two of the four conduit advection models in Jackson et al. (12)—then an even larger fraction (73%) of the global hotspot buoyancy flux is concentrated in the southern hemisphere.

We note that the quantity of subducted continental crust incorporated into the LLSVPs is not known, owing to great uncertainty associated with fluxes of continental crust to the mantle. Additionally, the observation of proportionately more austral hotspots could relate to the fact that the center of mass of the LLSVPs—which appear to source most hotspots (Figs. 1 and 4)—are shifted into the southern hemisphere (12). Nonetheless, we calculate that the heat flow carried by plumes (which is at least 2.0±0.3 TW (67)) can be matched by a deep continental reservoir that with a mass of continental crust that is ~28% of the modern continents, well within the range of prior estimates for total subducted upper continental crust materials over geologic time (68). Therefore, if located primarily in the southern hemisphere portions of the LLSVPs, a relatively modest contribution from a deeply subducted upper continental crust reservoir in the southern hemisphere could provide additional heat to explain both the greater number of hotspots and the higher summed hotspot buoyancy flux in the southern hemisphere.

Methods

Geochemical database of oceanic hotspot lavas. The hotspot geochemistry database includes the lowest $^{143}Nd/^{144}Nd$ (12) lava—here called the most EM sample—analyzed at each of the geochemically characterized oceanic hotspots, and is shown in Fig. 2. The geochemical database was published previously (12), where an extensive description of data curation is also provided. Nonetheless, a description of data curation in the geochemical database is provided in the SI Appendix. Additionally, a list of the 58 known hotspots (47 oceanic and 11 continental hotspots), which we examine here, is provided in Table S1 (we note that one oceanic hotspot, Vema, has not been geochemically characterized, thus only 46 oceanic hotspots are geochemically characterized and shown in Fig. 2). The geochemical data in the database is compiled in Jackson et al. (12), together with sources of the data, and the database is not republished here.

Plume locations beneath hotspots. In order to identify the deep mantle location of the enriched mantle domains sampled by each hotspot, we do not use the surface location of the hotspots and project vertically downward. Instead, we embrace the fact that plume conduits tilt as they rise through the mantle (20,21,61). Therefore, when examining the geographic distribution of geochemical domains in the mantle, we use the latitude of the calculated conduit bases at 2850 km depth beneath each hotspot, near the core-mantle boundary (CMB) (12). Methods for plume advection use here are published elsewhere (12), but are nonetheless are provided in the SI Appendix. An average of plume conduit locations for each hotspot at the base of the mantle, and hotspot locations at the Earth's surface, are calculated from individual conduit locations from Jackson et al. (12) and are provided in Table S1, as described in the SI Appendix.

Ancient rifted-passive margins over the past billion years. A previous compilation of passive margin formation, tenure, and death through Earth History (69) accounted for the number of rifted-passive margins and their terminations through time, but not the geographic length, latitude, or the timeframe between the start and end of collisional metamorphism. In order to calculate the lengths, locations (latitudes), and duration of subducted rifted-passive margins over the past 1000 Ma, individual margins were modified from previous compilations (69,70) and traced from georeferenced geological maps in QGIS (as shown in Fig. S3). The margins were captured at a similar spatial resolution (i.e., node spacing). These rifted-passive margin lines were assigned a start of rifting age, a passive margin start-date at the rift-drift transition, a passive margin end-date (i.e., at the beginning of collision, or "death" in Bradley (69)), and an end-collision age (Dataset S3). Margin length and craton area calculations utilized the QGIS function library, and the rifted-passive margin shapefiles are available in the Dataset S4. This allows us to present the paleolatitude and paleolength (Fig. 5 panels b and c; see Datasets S3 and S5) of ancient rifted-passive margin subduction over time (i.e., from the beginning to end of collision).

The description of each of the rifted-passive margins in our database is provided in the SI Appendix. As we are primarily concerned with the terminations of these margins, we lump composite rifts associated with failed rifts or rifting of a ribbon continent together as one margin. These processes can be discerned in younger examples, but are more difficult to define in older margins, which may contribute to the apparent secular decrease in rifted-passive margin lifespan (69). Most rifted-passive margins will end with an arc-continent collision. As such, sutures are assigned to each margin and the rifted-passive margin end-date corresponds with the start of exhumation date (70).

A collision begins when an ancient rifted-passive margin, with crust of thickness and composition that is transitional between oceanic and continental crust, enters the trench. Eventually this transitional and continental crust will jam the subduction zone, resulting in a collisional orogeny, and the subducting slab including some transitional and continental crust will break-off into the mantle (71). We define a collision end date to encompass the duration of subduction of transitional and continental crust to the mantle. We define the end of collision where constraints are known from reorganization of the plate geometry, geophysical imaging, or metamorphic ages. However, in most orogens that encompass an arc-continent collision followed by a continent-continent collision, like the India-Asia example, crustal thickening can persist for tens of millions of years after the initial collision (72). On the Himalayan margin, arc-continent collision began by 52 Ma along the Indus-Tsangpo and Shyok sutures (73), marked by the appearance of young volcanic material on the Indian margin (74). However, after the initial arc-continent collision, the subduction zone stepped north and consumed the Kshiroda plate (75,76) until collision between India and Eurasia starting at ~40 Ma (73). Thus, following the Himalayan example, where direct geological constraints are lacking, we use 40 Myr as a maximum duration of transitional and continental crust subduction to the mantle in a continent-continent collision. For an arc-continent collision, we use the modern example of New Guinea as a type location, where initial collision occurred at 16 Ma, and slab-breakoff occurred at 4 Ma (71), yielding a maximum duration of 12 Ma. The combined timescale of transitional and continental crust subduction to the mantle of 52 Myr (i.e., 12 Myr + 40 Myr) during a compound "soft" arc-continent collision and "hard" continent-continent collision encompasses the Himalayan orogeny and is used as a constraint on the upper limit for duration of collision for compound collisions where other constraints are lacking. For continent-continent collisions, we do not count the length of both margins, but instead count only the lower plate in the collision. Many collisional margins lack evidence for deep continental subduction, such as the Thor suture between Baltica and Avalonia; however, to minimize subjective filters, issues of preservation bias, and to keep the compilation independent from the UHP database (14), we preserve these margins in the database.

Some rifted-passive margins, such as the Pyreneean-Biscay margin, transformed into an active arc and retro-arc foreland without evidence for a collisional phase (69). These margins were relatively young and may have initiated subduction along transcurrent margins, and as such there is no evidence for subduction of the margin. Consequently, we have eliminated these types of margins from our compilation. We also do not include proposed rifted-passive margins (69) in the Farewell Terrane, the Hoggar, or the Idermeg terrane of Mongolia, because geological constraints on these terranes are lacking. Therefore, our estimates of subduction of Neoproterozoic rifted-passive margins is a conservative minimum. Additionally, although several Gondwanan sutures are present in Antarctica, too little is known to define Proterozoic rifted-passive margins and these are also excluded from our treatment.

The paleolatitude of rifted-passive margin subduction from the beginning to end of collision was determined by assigning a plate ID to each margin and restoring to its position at the time of collision onset in GPlates (43). For each margin, the latitude was extracted from the latitudinal midpoint at 5° resolution (using data from a paleomagnetic reference and spin-axis frame (43) with modification from recent literature (77)). The databases for rifted-passive margin tenures, paleolatitudes and summed subducted rifted-passive margin length are provided in Datasets S3 and S5.

Area normalized paleolatitude over the past 1 billion years. In order to construct Fig. 5 (panel c), which shows the paleolatitude of subducted passive margins over time, area normalized average paleolatitude was extracted from paleogeographic models at 20 Myr intervals for the Neoproterozoic (43) and at 10 Myr intervals for the Phanerozoic (46). Here we have merged the two data sets, which produced average latitudes that agree for overlapping intervals from 540-520 Ma. For the Neoproterozoic, continental areas were calculated in QGIS, including each of the major cratonic blocks larger than Nigeria-Benin, which has an area of 552,510 km^2. Continental fragments smaller than this were not included because of uncertainties in their size and paleolatitude. For each cratonic block, the latitude was extracted from the latitudinal midpoint at 5º resolution (using data from Merdith et al. (43) with modification from recent literature (77)). The area normalized continental paleolatitudes are compiled in Dataset S2.

Paleolatitude of UHP metamorphic terranes over time. In order to construct Fig. 5 (panel d), which shows the paleolatitude of low T/P metamorphic terranes (including UHP terranes) over the past 1000 Ma, occurrences of low temperature/high pressure and UHP metamorphism compiled by Brown & Johnson (14) were assigned plate IDs and restored to the paleolatitude at the time of formation using GPlates. Paleolatitudes were extracted at 5° resolution of the plate using rotation files from Merdith et al. (43), with modifications of Paleozoic terranes in Asia from Domeier (45) and Mesoproterozoic of Laurentia from Swanson-Hysell et al. (78). The low temperature/high pressure and UHP metamorphic occurrences and their reconstructed paleolatitudes are shown in Dataset S6.

Acknowledgements. M.G.J. acknowledges support from NSF EAR-1900652, OCE-1928970, and OCE-1912931. F.A.M. acknowledges support from NSF EAR-1926001 and EAR-1916698. Discussion with Roberta Rudnick and Brad Hacker benefitted concept development, and we thank Roberta for sharing her database of continental rocks. We thank Andrea Giuliani, Jasper

Konter, Esteban Gazel, Eemu Ranta, and Sunna Harðardóttir for comments. Thorsten Becker and Bernhard Steinberger provided insights into challenges associated with Dupal formation via subduction. Sunna Harðardóttir, Olivia Anderson, and Eliel Anttila are thanked for assistance with Figs. 2 and S1, Fig. 4, and the Movie S1, respectively.

References Cited

1. S. Mukhopadhyay, R. Parai, Noble Gases: A record of Earth's evolution and mantle dynamics. *Annual Rev. Earth Planet. Sci.* **47**, 389-419 (2019).
2. W.M White, A.W. Hofmann, Sr and Nd isotope heterogeneity of oceanic basalts and mantle evolution. *Nature* **296**, 821-825 (1982).
3. A.W. Hofmann, W.M. White, Mantle plumes from ancient oceanic crust. *Earth Planet. Sci. Lett.* **57**, 421-436 (1982).
4. A.W. Hofmann, Mantle geochemistry: The message from oceanic volcanism. *Nature* **385**, 219–229 (1997).
5. W.M. White, Isotopes, DUPAL, LLSVPs, and Anekantavada. *Chem. Geol*. **419**, 10–28 (2015).
6. S.R. Hart, A large-scale isotope anomaly in the Southern Hemisphere mantle. *Nature* **309**, 753-757 (1984).
7. B. Dupré, C.J. Allègre, Pb–Sr isotope variation in Indian Ocean basalts and mixing phenomena. *Nature* **303**, 142–146 (1983).
8. P. Castillo, The Dupal anomaly as a trace of the upwelling lower mantle. *Nature* **336**, 667–670 (1988).
9. C.J. Hawkesworth, M.S.M. Mantovani, P.N. Taylor, Z. Palacz, Evidence from the Parana of south Brazil for a continental contribution to Dupal basalts. *Nature* **322**, 356–359 (1986).
10. N.T. Arndt, S.L. Goldstein, An open boundary between lower continental crust and mantle: its role in crust formation and crustal recycling. *Tectonophysics* **161**, 201–212 (1989).
11. D. Weis, Y. Bassias, I. Gautier, J.P. Mennessier, Dupal anomaly in existence 115 Ma ago: evidence from isotopic study of the Kerguelen Plateau (South Indian Ocean). *Geochim. Cosmochim. Acta* **53**, 2125-2131 (1989).
12. M.G. Jackson, T.W. Becker, B. Steinberger, Spatial characteristics of recycled and primordial reservoirs in the deep mantle. *Geochem. Geophys. Geosyst*. **22** (2021). https://doi.org/10.1029/2020GC009525

13. D.A. Evans, True polar wander and supercontinents: Tectonophysics, v. 362, no. 1-4, p. 303-320 (2003).

14. M. Brown, T. Johnson, Time's arrow, time's cycle: Granulite metamorphism and geodynamics. *Mineralogical Magazine* **83**, 323-338 (2019a).

15. E. Sizova, T. Gerya, M. Brown, Contrasting styles of Phanerozoic and Precambrian continental collision. *Gondwana Research* **25**, 522-545 (2014).

16. J. van Hunen, M.B. Allen, Continental collision and slab break-off: A comparison of 3-D numerical models with observations. *Earth Planet. Sci. Lett*. **302**, 27-37 (2011).

17. B.R. Hacker, P.B. Kelemen, M.D. Behn, Differentiation of the continental crust by relamination. *Earth Planet. Sci. Lett*. **307**, 501-516 (2011).

18. B.R. Hacker, P.B. Kelemen, M.D. Behn, Continental lower crust. *Annu. Rev. Earth Planet. Sci.* **43**, 167–205 (2015).

19. L.S. Doucet, Z.-X. Li, H.G. El Dien, A. Pourteau, J.B. Murphy, W.J. Collins, N. Mattielli, H.K.H. Olierook, C.J. Spencer, R.N. Mitchell, Distinct formation history for deep mantle domains reflected in geochemical differences. *Nat. Geosci.* **13**, 511-515 (2020).

20. L. Boschi, T.W. Becker, B. Steinberger, On the statistical significance of correlations between synthetic mantle plumes and tomographic models. *Physics Earth Planet. Int*. **167**, 230–238 (2008).

21. S.W. French, B. Romanowicz, Broad plumes rooted at the base of the Earth's mantle beneath major hotspots *Nature* **525**, 95–99 (2015).

22. P.L. Nelson, S.P. Grand, Lower-mantle plume beneath the Yellowstone hotspot revealed by core waves. *Nature Geoscience* **11**, 280–284 (2018).

23. C. Chauvel, A.W. Hofmann, P. Vidal, HIMU-EM: The French Polynesian connection. *Earth Planet. Sci. Lett.* **110**, 99–119 (1992).

24. J. Eisele, M. Sharma, S.J.G. Galer, J. Blichert-Toft, C.W. Devey, A.W. Hofmann, The role of sediment recycling in EM-1 inferred from Os, Pb, Hf, Nd, Sr isotope and trace element systematics of the Pitcairn hotspot. *Earth Planet. Sci. Lett.* **196**, 197–212 (2002).

25. M.G. Jackson, S.R. Hart, A.A.P. Koppers, H. Staudigel, J. Konter, J. Blusztajn, M.D. Kurz, J.A. Russell, The return of subducted continental crust in Samoan lavas. *Nature* **448**, 684-687 (2007).

26. M. Willbold, A. Stracke, Formation of enriched mantle components by recycling of upper and lower continental crust. *Chem. Geol*. **276**, 188–197 (2010).

27. R.J. Stern, D.W. Scholl, Yin and yang of continental crust creation and destruction by plate tectonic processes. *Int. Geol. Rev.* **52**, 1-31 (2010). DOI: 10.1080/00206810903332322

28. P.D. Clift, P. Vannucchi, J.P. Morgan, Crustal redistribution, crust–mantle recycling and Phanerozoic evolution of the continental crust. *Earth-Science Reviews* **97**, 80-104 (2009).

29. D.W. Scholl, R. von Huene. Crustal recycling at modern subduction zones applied to the past—issues of growth and preservation of continental basement, mantle geochemistry, and supercontinent reconstruction. *Geol. Soc. Am. Mem*. **200**, 9–32 (2007)

30. B.J. Peters, R.W. Carlson, J.M.D. Day, M.F. Horan, Hadean silicate differentiation preserved by anomalous ^{142}Nd/^{144}Nd ratios in the Réunion hotspot source. *Nature* **555**, 89-93 (2018).

31. A. Mundl, M. Touboul, M.G. Jackson, J.M.D. Day, M.D. Kurz, V. Lekic, R.T. Helz, R.J. Walker, Tungsten-182 heterogeneity in modern ocean island basalts. *Science*. **356***,* 66-69 (2017).

32. R.L. Rudnick, S. Gao, in The Crust (ed. Rudnick, R. L.) 1–64, Vol. 3 of Treatise in Geochemistry (Elsevier, Amsterdam, 2003).

33. T. Plank, Constraints from thorium/lanthanum on sediment recycling at subduction zones and the evolution of the continents. *J. Pet.* **46**, 921-944 (2005).

34. M. Tang, R.L. Rudnick, W.F. McDonough, R.M. Gaschnig, Y. Huang, Europium anomalies constrain the mass of recycled lower continental crust. *Geology* **43**, 703–706 (2015).

35. P. Chowdhury, T. Gerya, S. Chakraborty, Emergence of silicic continents as the lower crust peels off on a hot plate-tectonic Earth. *Nat. Geosci*. **10**, 698-703 (2017).

36. A.E. Saal, M.D. Kurz, S.R. Hart, J.S. Blusztajn, J. Blichert-Toft, Y. Liang, D.J. Geist, The role of lithospheric gabbros on the composition of Galapagos lavas. *Earth Planet. Sci. Lett*. **257**, 391–406 (2007).

37. M. Tang, W.F. McDonough, R.D. Ash, Europium and strontium anomalies in the MORB source mantle. *Geochem. Cosmochim. Acta* **197**, 132-141 (2017).

38. T. Plank, The Chemical Composition of Subducting Sediments. In: Treatise on Geochemistry, ed. R.F. Keeling. Elsevier, Amsterdam, pp. 607-629. 2. ed. (2014). doi: 10.1016/B978-0-08-095975-7.00319-3.

39. T. Plank, C.H. Langmuir, The chemical composition of subducting sediment and its consequences for the crust and mantle. *Chem. Geol.* **145**, 325-394 (1998).

40. R.K. Workman, S.R. Hart, J.M. Eiler, M.G. Jackson, Oxygen isotopes in Samoan lavas: confirmation of continent recycling. *Geology* **36**, 551-554 (2008).

41. A. Reinhard, M.G. Jackson, J. Harvey, C. Brown, J.M. Koornneef, Extreme differences in $^{87}Sr/^{86}Sr$ between magmatic olivines and Samoan host lavas: Evidence for highly heterogeneous $^{87}Sr/^{86}Sr$ in the magmatic plumbing system sourcing a single lava. *Chem. Geol.* **439***, 120-131* (2016).

42. T.H. Torsvik, L.R.M. Cocks, *Earth history and palaeogeography* (Cambridge University Press, 2017).

43. A.S. Merdith, *et al*. Extending full-plate tectonic models into deep time: Linking the Neoproterozoic and the Phanerozoic. *Earth. Sci. Reviews* **214** (2020).

44. M. Domeier, P.V. Doubrovine, T.H. Gorsvik, W. Spakman, A. Bull, Global correlation of lower mantle structure and past subduction. *Geophys. Res. Lett.* **43**, 4945–4953 (2016).

45. M. Domeier, Early Paleozoic tectonics of Asia: Towards a full-plate model. *Geoscience Frontiers **9***, 789-862 (2018).

46. T.H. Torsvik, H.H. Svensen, B. Steinberger, D.L. Royer, D.A. Jerram, M.T. Jones, M. Domeier, Connecting the deep Earth and the atmosphere, in Mantle Convection and Surface Expressions, Geophys. Monogr. Ser., edited by Marquardt, H., Cottaar, S., Konter, J., & Ballmer, M. American Geophysical Union, Washington, D.C., *in press* (2021). Available on online at https://eartharxiv.org/repository/object/280/download/554/.

47. M.L. Rudolph, S. Zhong, Does quadrupole stability imply LLSVP fixity? *Nature* **503**, E3-E4 (2013).

48. R.K. Bono, J.A. Tarduno, A stable Ediacaran Earth recorded by single silicate crystals of the ca. 565 Ma Sept-Îles intrusion. *Geology* **43**, 131-13 (2015)

49. H.C. Halls, A. Lovette, M. Hamilton, U. Söderlund, A paleomagnetic and U–Pb geochronology study of the western end of the Grenville dyke swarm: Rapid changes in paleomagnetic field direction at ca. 585 Ma related to polarity reversals? *Precambrian Research* **257**, 137-166 (2015).

50. B. Robert, J. Besse, O. Blein, M. Greff-Lefftz, T. Baudin, F. Lopes, S. Meslouh, M. Belbadaoui, Constraints on the Ediacaran inertial interchange true polar wander hypothesis: A new paleomagnetic study in Morocco (West African Craton). *Precambrian Research* **295**, 90-116 (2017).

51. R.K. Bono, J.A. Tarduno, F. Nimmo, R.D. Cottrell, Young inner core inferred from Ediacaran ultra-low geomagnetic field intensity. *Nat. Geosci.* **12**, 143-147 (2019).

52. D. Thallner, A.J. Biggin, H.C. Halls, An extended period of extremely weak geomagnetic field suggested by palaeointensities from the Ediacaran Grenville dykes (SE Canada). *Earth Planet Sci. Lett.* **568**, *117025* (2021).

53. R.D. Nance, J.B. Murphy, Supercontinents and the case for Pannotia. In R.W. Wilson, G.A. Houseman, K.J.W. McCaffrey, A.G. Doré, S.J.H. Buiter (eds). Fifty Years of the Wilson Cycle Concept in Plate Tectonics. *Geological Society, London, Special Publications* **470**, (2018). https://doi.org/10.1144/SP470.5

54. B. Goscombe, D.A. Foster, D. Gray, B. Wade, Assembly of central Gondwana along the Zambezi Belt: Metamorphic response and basement reactivation during the Kuunga Orogeny. *Gondwana Res.* **80**, 410-465 (2020).

55. W.G. Ernst, Preservation/exhumation of ultrahigh-pressure subduction complexes. *Lithos* **92**, 321–335 (2006).

56. M. Brown, T. Johnson, MSA Presidential Address: Metamorphism and the evolution of subduction on Earth. *American Mineralogist* **104**, 1065–1082 (2019b).

57. Delavault, H., Chauvel, C., Thomassot, E., Devey, C.W., & Dazas, B.. Sulfur and lead isotopic evidence of relic Archean sediments in the Pitcairn mantle plume. *Proc. Nat. Acad. Sci*. **113**, 12952-12956 (2016).

58. J. Woodhead, J. Hergt, A. Giuliani, R. Maas, D. Phillips, D.G. Pearson, G. Nowell, Kimberlites reveal 2.5-billion-year evolution of a deep, isolated mantle reservoir. *Nature* **573**, 578-581 (2019).

59. A. Giuliani, M.G. Jackson, A. Fitzpyane, H. Dalton, Remnants of early Earth differentiation in the deepest mantle-derived lavas. *Proc. Nat. Acad. Sci.* **118** (2020).

60. D. Van der Meer, W. Spakman, D.J.J. van Hinsberger, M.L. Amaru, T.H. Torsvik, Towards absolute plate motions constrained by lower-mantle slab remnants. *Nat. Geosci*. **3**, 36-40 (2010).

61. B. Steinberger, P.L. Nelson, S.P. Grand, W. Wang, Yellowstone plume conduit tilt caused by large-scale mantle flow. *Geochem. Geophys. Geosyst*. **20** (2019). doi:10.1029/2019gc008490

62. E.J. Garnero, A.K. McNamara, S.-H. Shim, Continent-sized anomalous zones with low seismic velocity at the base of Earth's mantle. *Nature Geoscience* **9**, 481–489 (2016).

63. D. Weis, M.O. Garcia, J.M. Rhodes, M. Jellinek, J.S. Scoates, Role of the deep mantle in generating the compositional asymmetry of the Hawaiian mantle plume. *Nat. Geosci.* **4**, 831-838 (2011).

64. R. Hassan, N. Flament, M. Gurnis, D.J. Bower, D. Muller, Provenance of plumes in global convection models. *Geochem. Geophys. Geosyst*. **16** (2016). doi:10.1002/2015GC005751

65. A.K. McNamara, S. Zhong, Thermochemical structures beneath Africa and the Pacific Ocean. *Nature* **437**, 1136-1139 (2005).

66. D.J. Bower, M. Gurnis, M. Seton, Lower mantle structure from paleogeographically constrained dynamic Earth models. *Geochem. Geophys. Geosyst.* **14**, 44–63 (2013).

67. M.J. Hoggard, R. Parnell-Turner, N. White, Hotspots and mantle plumes revisited: Toward reconciling the mantle heat transfer discrepancy. *Earth Planet. Sci. Lett.* **542**, 116317 (2020).

68. A.W. Hofmann, The lost continents. *Nature* **448**, 655-656 (2007).

69. D.C. Bradley, Passive margins through earth history. *Earth-Science Reviews* **91**, 1-26 (2008).

70. F.A. Macdonald, N.L. Swanson-Hysell, Y. Park, L.E. Lissiecki, Arc-continent collisions in the tropics set the Earth's climate state. *Science* **364**, 181-184 (2019).

71. M. Cloos, *et al.* Collisional delamination in New Guinea: The geotectonics of subducting slab-breakoff. *Geological Society of America Special Papers* **400**, 1-51 (2005).

72. M. Ingalls, D.B. Rowley, B. Currie, A.S. Colman, Large-scale subduction of continental crust implied by India–Asia mass-balance calculation. *Nature Geoscience* **9**, 848-853 (2016).

73. P. Bouilhol, O. Jagoutz, J.M. Hanchar, F.O. Dudas, Dating the India–Eurasia collision through arc magmatic records. *Earth Planet. Sci. Lett.* **366**, 163-175 (2013).

74. L. Ding, *et al.* The India–Asia collision in north Pakistan: Insight from the U–Pb detrital zircon provenance of Cenozoic foreland basin. *Earth and Planetary Science Letters* **455**, 49-61 (2016).

75. C.R. Martin, *et al.* Paleocene latitude of the Kohistan–Ladakh arc indicates multistage India–Eurasia collision. *Proc. Nat. Acad. Sci.* **117**, 29487-29494 (2020).

76. O. Jagoutz, L. Royden, A.F. Holt, T.W. Becker, Anomalously fast convergence of India and Eurasia caused by double subduction. *Nature Geoscience* **8**, 475 (2015).

77. A. Eyster, B.P. Weiss, K. Karlstrom, F.A. Macdonald, Paleomagnetism of the Chuar Group and evaluation of the late Tonian Laurentian apparent polar wander path with implications for the makeup and breakup of Rodinia. *GSA Bulletin* **132**, 710-738 (2020).

78. N.L. Swanson-Hysell, J. Ramezani, L.M. Fairchild, I.R. Rose, Failed rifting and fast drifting: Midcontinent rift development, Laurentia's rapid motion and the driver of Grenvillian orogenesis. *Bulletin* **131**, 913-940 (2019).

79. M. Brown, C.L. Kirkland, T.E. Johnson, Evolution of geodynamics since the Archean: Significant change at the dawn of the Phanerozoic. *Geology* **48**, 488-492 (2020).

Figure legends

Figure 1. Positions of the continents at present and at 500 Ma. Panel A) Pre-Mesozoic continental plates are shown in dark grey with present continental outlines in light grey for reference. The location of plume conduits at 2850 km depth for the 11 oceanic EM hotspots are shown as large red circles, and the continental and non-EM oceanic hotspot conduits are shown as smaller blue squares (Dataset S1). LLSVPs are shaded pink and defined by the 0.75 RMS velocity contour at 2850 km in the S40RTS model after Jackson et al. (12). Panel B) Reconstruction of continents at 500 Ma (43), showing the distribution of the continents primarily in the southern hemisphere during formation of Gondwana. Right-hand columns show polar projections, emphasizing the change in area normalized average continental latitude from ~34ºS at 500 Ma (panel B) to ~12ºN in the present (panel A), as shown in Fig. 5 (panel B). The 500 Ma reconstruction is a snapshot from the Movie S1, which provides a video showing a plate reconstruction (43) from 1 Ga to present, and shows rifted passive margins listed in Dataset S3 (and uses rifted passive margin shapefiles available in the Dataset S4). Both panels show the same longitude reference frame and are centered at 110º. The 500 Ma reconstruction uses a

paleomagnetic reference frame that is not fixed to the mantle (43). For a modeled mantle reference frame reconstruction at 500 Ma, see Fig. S2, which predicts similar latitudes and geometries between the continents, but different longitudes.

Figure 2. **Defining the austral hemisphere EM domain in radiogenic isotope space (left panel) and its geographic extent in the southern hemisphere (right panel).** The most geochemically extreme lava with the lowest $^{143}Nd/^{144}Nd$ from every known geochemically-characterized oceanic hotspot is shown using the database from Jackson et al. (12). Eleven oceanic EM hotspots linked to the southern hemisphere mantle via plume conduits have lower $^{143}Nd/^{144}Nd$ than any hotspots linked to the northern hemisphere, and the geographic distribution of these 11 hotspots defines the Dupal domain. Latitudes are for the bases of advected plume conduits at 2850 km, and the latitude shown for each hotspot is an average (with 2SD error bars) of results for plume advection in four different global seismic models (Dataset S1). Forty-seven oceanic hotspots are known, but only 46 are shown in the right panel because Vema hotspot has not been geochemically characterized. Another hotspot—Lord Howe—does not have published $^{87}Sr/^{86}Sr$ so cannot be included in the left panel. Continental hotspots are excluded from the figure due to the potential for crustal contamination. Diamond symbols are hotspots associated with the Pacific LLSVP, triangles are African LLSVP hotspots, and circles represent hotspots located far from LLSVP boundaries (>500 km outside of the LLSVPs, defined in Dataset S1). The 11 hotspots with the lowest $^{143}Nd/^{144}Nd$ are: Tristan/Gough hotspot (TR), Discovery (DI), Samoa (SA), Pitcairn (PI), Meteor/Shona (MS), Tasmantid (TA), Heard/Kerguelen (HK), Hawaii (HW), San Felix (SF), Societies (SO), and Amsterdam/St. Paul (AM). Symbols are shaded (red-blue scale) for the latitude of the calculated conduit base at 2850 km. All data shown in the figure are compiled in Jackson et al. (12).

Figure 3. Schematic depiction of tectonic environments through time illustrating lack of silicic continental crust subduction during shallow slab-breakoff prior to 650 Ma and onset of silicic continental crust subduction during deep slab-breakoff after 650 Ma. A) During supercontinent breakup, such as the breakup of Rodinia from ~780-650 Ma, ancient continental crust is rifted, which results in margins composed of Archean and Proterozoic crust that could later be subducted. B) During continent-continent collision in the Archean to Proterozoic, prior

to the first appearance of continental UHP at ~650 Ma (Figs. 5 and 6), shallow slab-breakoff occurs within the down-going oceanic crust before the continental crust is pulled to mantle depths. C) Continent-continent collision from the Neoproterozoic to present, after the first appearance of UHP metamorphism in continental terranes at ~ 650 Ma (Figs. 5 and 6). Secular cooling resulted in increased strength of (and coupling between) continental and the down-going oceanic crust. As a result, continental crust attached to the down-going slab is pulled to mantle depths appropriate for UHP metamorphism before slab-breakoff can occur, and a portion of the continental crust (attached to the down-going slab) can detach from the continents and subduct into the mantle. Note that sediment and continental material from subduction erosion (yellow shaded in all panels) is not attached to the down-going slab and may be buoyant and relaminate onto the lower continental crust instead of subducting into the mantle (17,18).

Figure 4. Distribution of 58 known global hotspots (oceanic and continental) as a function of latitude. There are more than twice as many southern hemisphere hotspots (N=39) as northern hemisphere hotspots (N=19). Latitudes are for the bases of advected ("tilted") plume conduits at 2850 km depth, and represent an average for results from four global seismic models (Dataset S1). All 47 known oceanic hotspots and 11 continental hotspots are shown in the figure, which contrasts with Figs. 1 and 2, where continental hotspots are excluded due to concerns of crustal contamination overprinting mantle Sr and Nd isotope signatures (Methods). (Additionally, the two oceanic hotspots that are not, or not completely, geochemically characterized—Vema and Lord Howe—are shown here). Plume conduits for >80% (of all hotspots globally trace back to the LLSVPs (12), even though LLSVPs cover only ~30% of the CMB (62), suggesting a strong link between LLSVPs and hotspot generation via plume formation. However, 11 of the 58 hotspots in the hotspot catalogue are not associated with LLSVPS. When only LLSVP-related hotspots (i.e., hotspots linked by advected plume conduits to the LLSVPs) are considered, there are more than three times as many southern hemisphere hotspots (N=36) as northern hemisphere hotspots (N=11). The database of 58 hotspots, their classification as LLSVP-related and non-LLSVP hotspots (and description of this classification scheme), and the average latitudes of advected plume conduits at 2850 km calculated in four different global seismic models (and a description of the plume advection models and the seismic models used) are provided in Jackson et al. (12) and summarized in Dataset S1.

Figure 5. A billion-year record of continental paleolatitudes, rifted passive margin subduction paleolatitude and intensity, and paleolatitude of continental low T/P (including UHP) metamorphism occurrences. Panel A) Area-normalized average continental paleolatitude calculated back to 1 Ga shows the continents deep in the southern hemisphere during assembly of Gondwana and Pangea; continental paleolatitude calculations are provided in Dataset S2. Panel B) Ancient rifted passive margin subduction lengths in the southern (red lines) and northern (blue lines) hemispheres are shown back to 1 Ga, with a pulse of southern hemisphere margin subduction that follows the 650 Ma (age published elsewhere (14)) first occurrence of a continental UHP rock (i.e., ≥ 2.7 Gpa). The subducted ancient rifted-passive margin lengths are provided in Dataset S5. Panel C) In this panel, the data from panel B are instead expressed as a function of the paleolatitude of the midpoint of the margin at subduction start date, showing that the subduction of ancient rifted-passive margins occurred overwhelmingly in the southern hemisphere during Gondwana-Pangea assembly (Dataset S3). Panel D) Paleolatitude of low T/P continental metamorphic terranes, including UHP metamorphic terranes, are positioned in the southern hemisphere during assembly of Gondwana and Pangea; unlike continental terranes, oceanic low T/P and UHP terranes are found at all latitudes. The data shown are published elsewhere (14), and the paleolatitudes are provided in Dataset S6. The first appearance of continental UHP rocks at 650 Ma (14) defines initiation of the austral hemisphere EM domain formation interval (vertical grey bar); continental material subducted after 300 Ma has had insufficient time to be recycled back to the surface in hotspots, and defines the end of the austral hemisphere EM domain formation interval. Supercontinent tenures are modified from elsewhere (13).

Figure 6. A three-billion-year record of metamorphism. Panel A) The distribution of high temperature/pressure (high T/P in figure), intermediate temperature/pressure (intermediate T/P), and low temperature/pressure (low T/P) metamorphism is shown over time over time, and demonstrates that low T/P metamorphism is common and widespread only since the late-Neoproterozoic. Panel B) The pressures of only low T/P metamorphic rocks (not include intermediate and high T/P rocks) are shown over time. Data are separated by oceanic (yellow) and continental (blue) protoliths. The first appearance of *continental* UHP metamorphism (i.e., ≥

2.7 Gpa) is at ~650 Ma; low T/P continental rocks appear before 650 Ma, but none achieve UHP pressures. UHP rocks do appear before 650 Ma but all are oceanic protoliths, not continental. Data, including the oldest (650 Ma) continental UHP rock, are from a compilation published elsewhere (14). The thermobarometric ratio curve is from elsewhere (79).

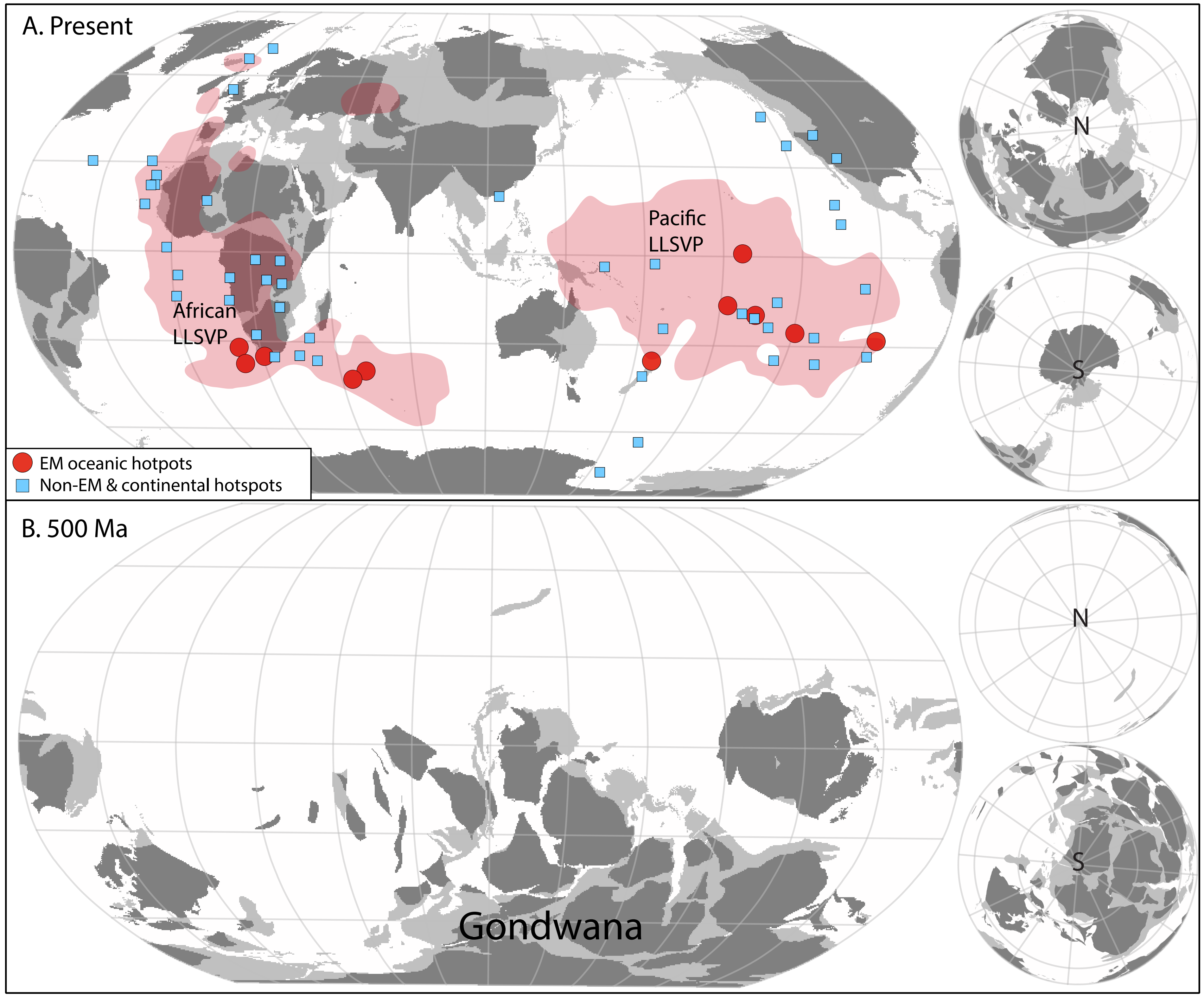

Figure 1. Positions of the continents at present and at 500 Ma. Panel A) Pre-Mesozoic continental plates are shown in dark grey with present continental outlines in light grey for reference. The location of plume conduits at 2850 km depth for the 11 oceanic EM hotspots are shown as large red circles, and the continental and non-EM oceanic hotspot conduits are shown as smaller blue squares (Dataset S1). LLSVPs are shaded pink and defined by the 0.75 RMS velocity contour at 2850 km in the S40RTS model after Jackson et al. (12). Panel B) Reconstruction of continents at 500 Ma (43), showing the distribution of the continents primarily in the southern hemisphere during formation of Gondwana. Right-hand columns show polar projections, emphasizing the change in area normalized average continental latitude from ~34ºS at 500 Ma (panel B) to ~12ºN in the present (panel A), as shown in Fig. 5A. The 500 Ma reconstruction is a snapshot from the Movie S1, which provides a video showing a plate reconstruction (43) from 1 Ga to present, and shows rifted passive margins listed in Dataset S3 (and uses rifted passive margin shapefiles available in the Dataset S4). Both panels show the same longitude reference frame and are centered at 110º. The 500 Ma reconstruction uses a paleomagnetic reference frame that is not fixed to the mantle (43). For a modeled mantle reference frame reconstruction at 500 Ma, see Fig. S2, which predicts similar latitudes and geometries between the continents, but different longitudes.

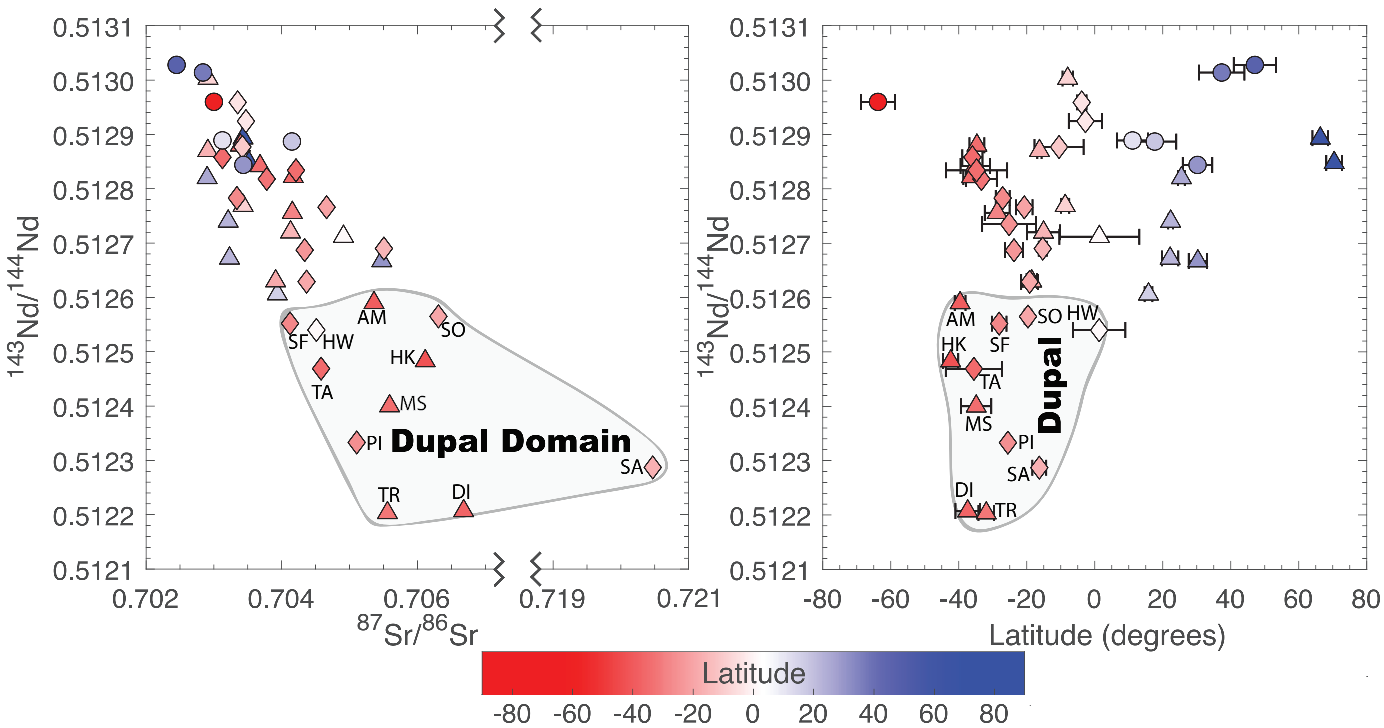

Figure 2. Defining the austral hemisphere EM domain in radiogenic isotope space (left panel) and its geographic extent in the southern hemisphere (right panel). The most geochemically extreme lava with the lowest $^{143}Nd/^{144}Nd$ from every known geochemically-characterized oceanic hotspot is shown using the database from Jackson et al. (12). Eleven oceanic EM hotspots linked to the southern hemisphere mantle via plume conduits have lower $^{143}Nd/^{144}Nd$ than any hotspots linked to the northern hemisphere, and the geographic distribution of these 11 hotspots defines the Dupal domain. Latitudes are for the bases of advected plume conduits at 2850 km, and the latitude shown for each hotspot is an average (with 2SD error bars) of results for plume advection in four different global seismic models (Dataset S1). Forty-seven oceanic hotspots are known, but only 46 are shown in the right panel because Vema hotspot has not been geochemically characterized. Another hotspot—Lord Howe—does not have published $^{87}Sr/^{86}Sr$ so cannot be included in the left panel. Continental hotspots are excluded from the figure due to the potential for crustal contamination. Diamond symbols are hotspots associated with the Pacific LLSVP, triangles are African LLSVP hotspots, and circles represent hotspots located far from LLSVP boundaries (>500 km outside of the LLSVPs, defined in Dataset S1). The 11 hotspots with the lowest $^{143}Nd/^{144}Nd$ are: Tristan/Gough hotspot (TR), Discovery (DI), Samoa (SA), Pitcairn (PI), Meteor/Shona (MS), Tasmantid (TA), Heard/Kerguelen (HK), Hawaii (HW), San Felix (SF), Societies (SO), and Amsterdam/St. Paul (AM). Symbols are shaded (red-blue scale) for the latitude of the calculated conduit base at 2850 km. All data shown in the figure are compiled in Jackson et al. (12).

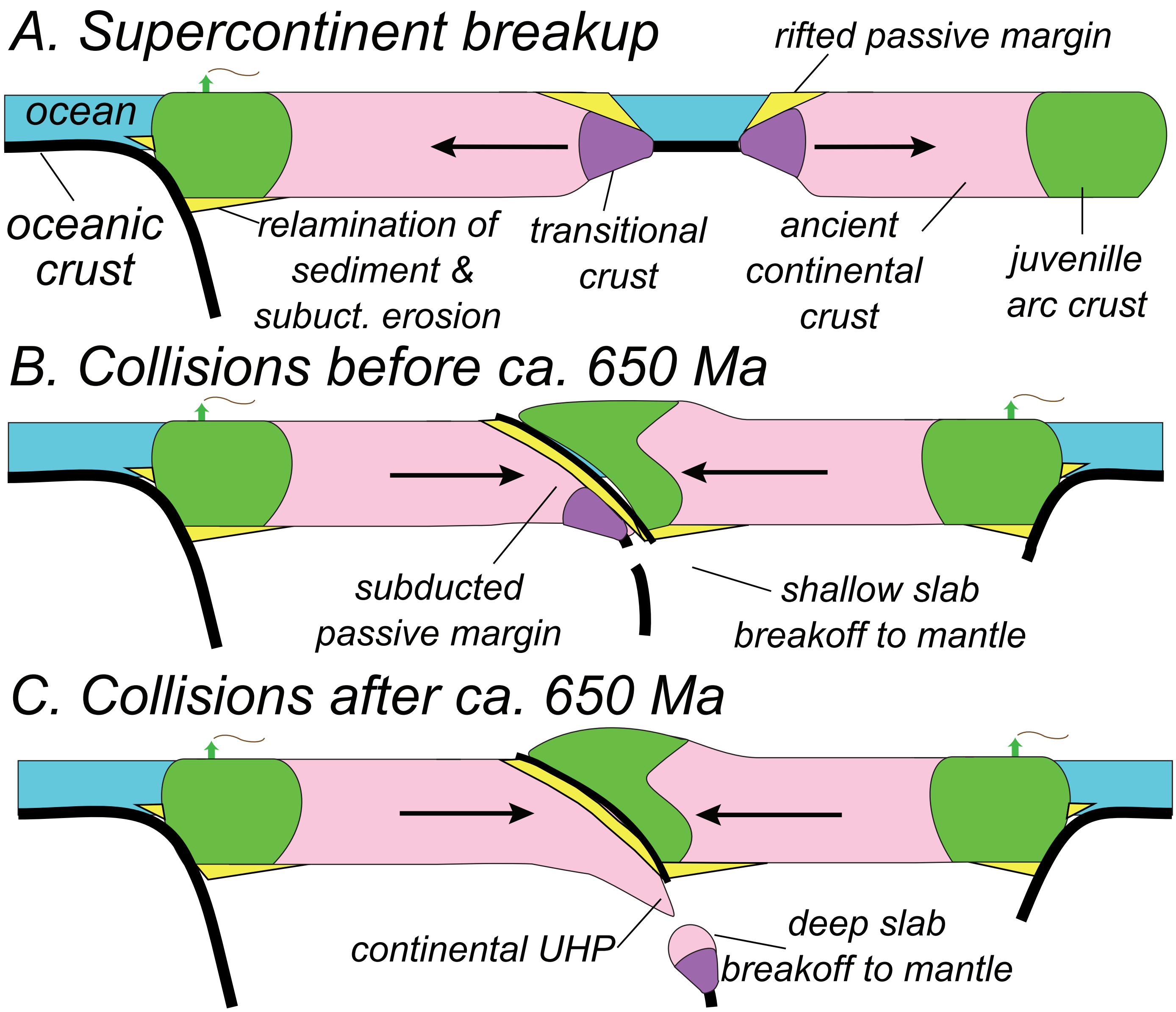

Figure 3. Schematic depiction of tectonic environments through time illustrating lack of silicic continental crust subduction during shallow slab-breakoff prior to 650 Ma and onset of silicic continental crust subduction during deep slab-breakoff after 650 Ma. A) During supercontinent breakup, such as the breakup of Rodinia from ~780-650 Ma, ancient continental crust is rifted, which results in margins composed of Archean and Proterozoic crust that could later be subducted. B) During continent-continent collision in the Archean to Proterozoic, prior to the first appearance of continental UHP at ~650 Ma (Figs. 5 and 6), shallow slab-breakoff occurs within the down-going oceanic crust before the continental crust is pulled to mantle depths. C) Continent-continent collision from the Neoproterozoic to present, after the first appearance of UHP metamorphism in continental terranes at ~ 650 Ma (Figs. 5 and 6). Secular cooling resulted in increased strength of (and coupling between) continental and the down-going oceanic crust. As a result, continental crust attached to the down-going slab is pulled to mantle depths appropriate for UHP metamorphism before slab-breakoff can occur, and a portion of the continental crust (attached to the down-going slab) can detach from the continents and subduct into the mantle. Note that sediment and continental material from subduction erosion (yellow shaded in all panels) is not attached to the down-going slab and may be buoyant and relaminate onto the lower continental crust instead of subducting into the mantle (17,18).

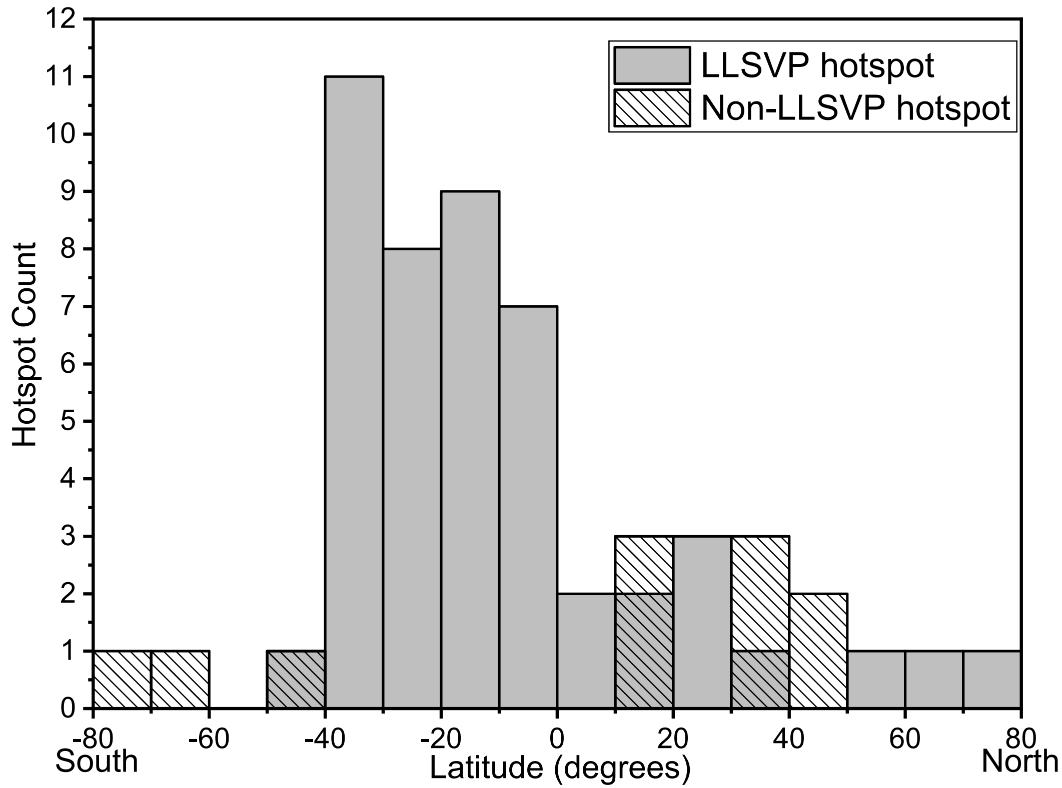

Figure 4. Distribution of 58 known global hotspots (oceanic and continental) as a function of latitude. There are more than twice as many southern hemisphere hotspots (N=39) as northern hemisphere hotspots (N=19). Latitudes are for the bases of advected ("tilted") plume conduits at 2850 km depth, and represent an average for results from four global seismic models (Dataset S1). All 47 known oceanic hotspots and 11 continental hotspots are shown in the figure, which contrasts with Figs. 1 and 2, where continental hotspots are excluded due to concerns of crustal contamination overprinting mantle Sr and Nd isotope signatures (Methods). (Additionally, the two oceanic hotspots that are not, or not completely, geochemically characterized—Vema and Lord Howe—are shown here). Plume conduits for >80% (of all hotspots globally trace back to the LLSVPs (12), even though LLSVPs cover only ~30% of the CMB (62), suggesting a strong link between LLSVPs and hotspot generation via plume formation. However, 11 of the 58 hotspots in the hotspot catalogue are not associated with LLSVPS. When only LLSVP-related hotspots (i.e., hotspots linked by advected plume conduits to the LLSVPs) are considered, there are more than three times as many southern hemisphere hotspots (*N*=36) as northern hemisphere hotspots (*N*=11). The database of 58 hotspots, their classification as LLSVP-related and non-LLSVP hotspots (and description of this classification scheme), and the average latitudes of advected plume conduits at 2850 km calculated in four different global seismic models (and a description of the plume advection models and the seismic models used) are provided in Jackson et al. (12) and summarized in Dataset S1.

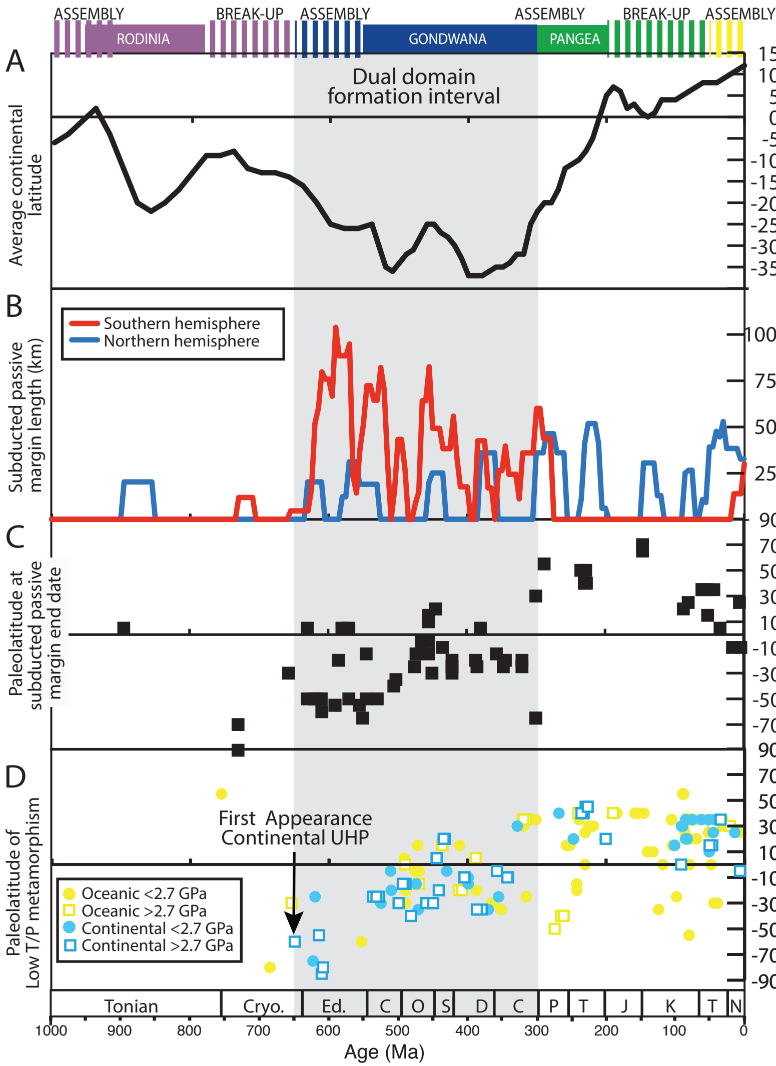

Figure 5. A billion-year record of continental paleolatitudes, rifted passive margin subduction paleolatitude and intensity, and paleolatitude of continental low T/P (including UHP) metamorphism occurrences. Panel A) Area-normalized average continental paleolatitude calculated back to 1 Ga shows the continents deep in the southern hemisphere during assembly of Gondwana and Pangea; continental paleolatitude calculations are provided in Dataset S2. Panel B) Ancient rifted passive margin subduction lengths in the southern (red lines) and northern (blue lines) hemispheres are shown back to 1 Ga, with a pulse of southern hemisphere margin subduction that follows the 650 Ma (age published elsewhere (14)) first occurrence of a continental UHP rock (i.e., ≥ 2.7 Gpa). The subducted ancient rifted-passive margin lengths are provided in Dataset S5. Panel C) In this panel, the data from panel B are instead expressed as a function of the paleolatitude of the midpoint of the margin at subduction start date, showing that the subduction of ancient rifted-passive margins occurred overwhelmingly in the southern hemisphere during Gondwana-Pangea assembly (Dataset S3). Panel D) Paleolatitude of low T/P continental metamorphic terranes, including UHP metamorphic terranes, are positioned in the southern hemisphere during assembly of Gondwana and Pangea; unlike continental terranes, oceanic low T/P and UHP terranes are found at all latitudes. The data shown are published elsewhere (14), and the paleolatitudes are provided in Dataset S6. The first appearance of continental UHP rocks at 650 Ma (14) defines initiation of the austral hemisphere EM domain formation interval (vertical grey bar); continental material subducted after 300 Ma has had insufficient time to be recycled back to the surface in hotspots, and defines the end of the austral hemisphere EM domain formation interval. Supercontinent tenures are modified from elsewhere (13).

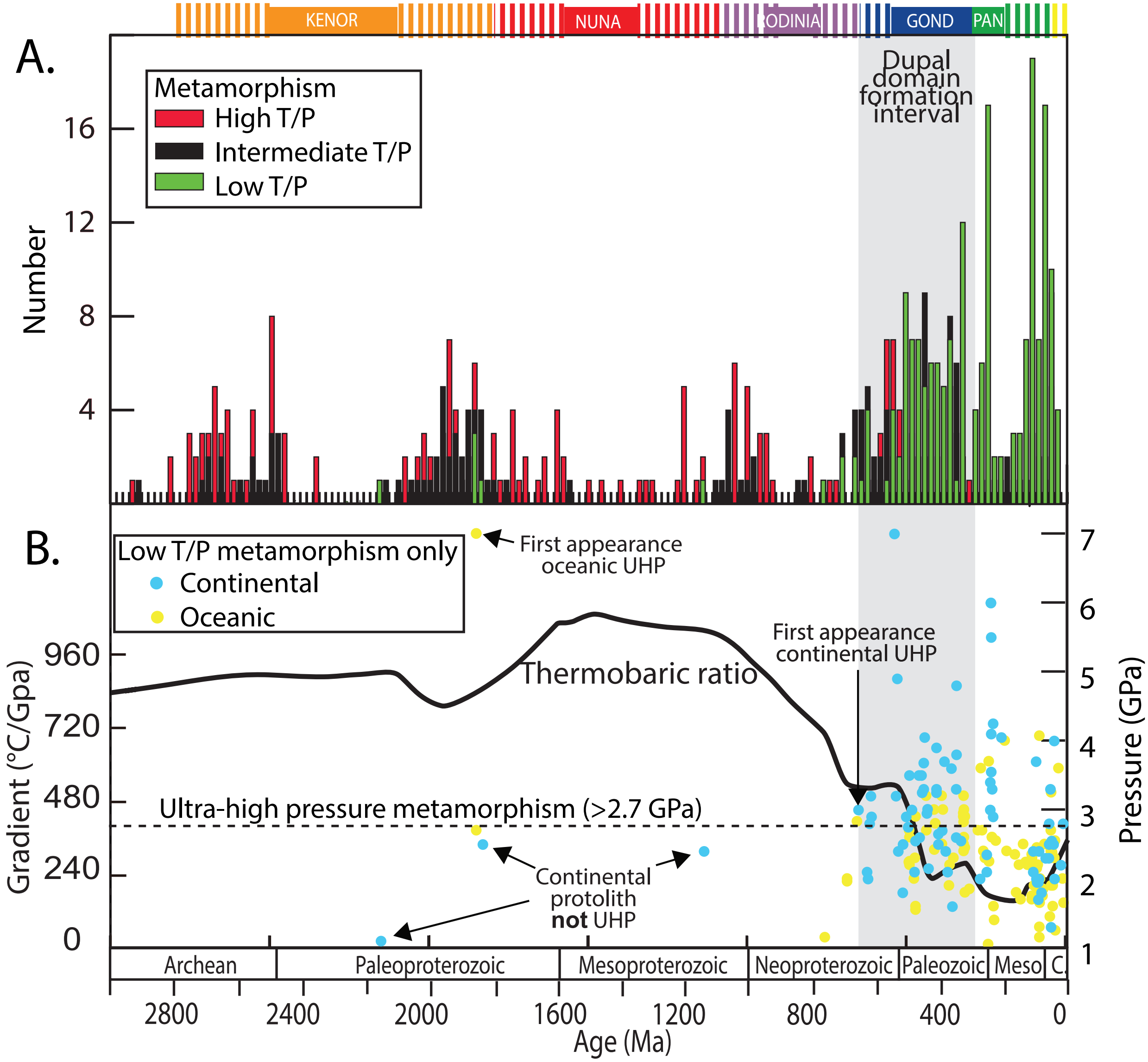

Figure 6. A three-billion-year record of metamorphism. Panel A) The distribution of high temperature/pressure (high T/P in figure), intermediate temperature/pressure (intermediate T/P), and low temperature/pressure (low T/P) metamorphism is shown over time over time, and demonstrates that low T/P metamorphism is common and widespread only since the late-Neoproterozoic. Panel B) The pressures of only low T/P metamorphic rocks (not include intermediate and high T/P rocks) are shown over time. Data are separated by oceanic (yellow) and continental (blue) protoliths. The first appearance of *continental* UHP metamorphism (i.e., ≥ 2.7 Gpa) is at ~650 Ma; low T/P continental rocks appear before 650 Ma, but none achieve UHP pressures. UHP rocks do appear before 650 Ma but all are oceanic protoliths, not continental. Data, including the oldest (650 Ma) continental UHP rock, are from a compilation published elsewhere (14). The thermobarometric ratio curve is from elsewhere (79).

Supplementary Information Text

Geochemical database of oceanic hotspot lavas.

The geochemical database providing the most extreme (lowest $^{143}Nd/^{144}Nd$) lava from all known geochemically-characterized oceanic hotspots is published elsewhere (1). To explore the distribution of EM domains, we examine only the lowest $^{143}Nd/^{144}Nd$ lava from each hotspot. Alternative approaches, such as identifying the mean or median $^{143}Nd/^{144}Nd$ of all lavas from each hotspot, do not identify the global distribution of the *most enriched* geochemical domain sampled by each hotspot.

As discussed elsewhere (2), the minimum hotspot $^{143}Nd/^{144}Nd$ is the preferred indicator of geochemical enrichment in oceanic lavas over $^{87}Sr/^{86}Sr$ and $^{176}Hf/^{177}Hf$ because 1) $^{143}Nd/^{144}Nd$ is less susceptible to seawater contamination than $^{87}Sr/^{86}Sr$, and 2) far more $^{143}Nd/^{144}Nd$ data are available in OIB than $^{176}Hf/^{177}Hf$ data. Derived Pb-isotope parameters (i.e., $^{208}Pb^*/^{206}Pb^*$, $\Delta^{207}Pb/^{204}Pb$, $\Delta^{208}Pb/^{204}Pb$) (3, 4) also correlate with geochemical enrichment, but Pb isotope databases for OIB suffer from lower precision datasets that were generated prior to the advent of modern techniques that monitor in-run Pb isotope fractionation (e.g., MC-ICP-MS analyses using Tl addition or double- and triple-spike Pb isotope analysis by TIMS). Available Pb isotopic data for much of the oceanic hotspot dataset was obtained using older TIMS methods that did not control in-run isotope fractionation, leaving many hotspots without available high-precision modern Pb isotope measurements. Therefore, we do not further explore Pb isotopic data here. We note that Hart (3) relied on only $^{87}Sr/^{86}Sr$ and Pb isotopes to define the geographic extent of the Dupal domain; compared to the $^{87}Sr/^{86}Sr$ and Pb-isotopic datasets, however, relatively little $^{143}Nd/^{144}Nd$ data existed at the time. While we define the Dupal domain differently (i.e., using $^{143}Nd/^{144}Nd$) than Hart (3), we note that Hart (3) used $^{87}Sr/^{86}Sr$ when defining the Dupal and $^{87}Sr/^{86}Sr$ shows a strong inverse relationship with $^{143}Nd/^{144}Nd$ (**Fig. 2**).

The geochemical database used here and description of methodology for database construction are provided in (1). Hotspot lavas erupted in continental settings are excluded from the analysis because continental crust assimilation—a mechanism that can impart low $^{143}Nd/^{144}Nd$ and high $^{87}Sr/^{86}Sr$ on upwelling mantle-derived melts—can mask mantle signals with shallow-derived continental fingerprints. Therefore, the geographic extent of the Dupal domain is defined using oceanic hotspots only, and the histogram in **Fig. 4** shows the global latitude distribution of all hotspots, oceanic and continental. In the published geochemical database used here, Sr and Nd isotopes were obtained on the same sample (i.e., the sample with the lowest $^{143}Nd/^{144}Nd$ from each hotspot). We do not apply an "age threshold" for the analysis: we assume that a volcano located along a particular hotspot track erupted over the hotspot, no matter the age of the volcano, and this approach allows us to assign the latitude and longitude of the hotspot to samples collected anywhere along a hotspot track.

Plume locations beneath hotspots.

Because it is difficult to resolve plume conduits under some hotspots due to the low resolution available in global seismic models, plume conduits calculated in plume advection models (5-7) allow us to explore how the different plumes tilt as they up-well, and infer the location of the plume conduit at the core-mantle boundary.

Methods for the calculation of advected conduit bases presented here are presented in (1), together with hotspot locations at the surface. In short, to define plume conduit locations beneath each hotspot, we use an average location of the calculated advected conduits bases calculated at 2850 km depth from four seismic models: SEMUCB-WM1 (8), S40RTS (9), SMEAN2 (10), and TX2016 (11). The average of the plume conduit locations at 2850 km from the four models is shown in **Dataset S1**. The variability in the latitude of the conduit base location across the four seismic models is reflected in the 2 SD error bars on latitude in **Fig. 2** (see **Dataset S1**). Although using the latitude of the surface location of the hotspot would not significantly change the results of this study, our treatment is more accurate because plumes are advected laterally in the convecting mantle as they rise (6-8). Advected conduits show that the deep mantle plume source for two of the 47 oceanic hotspots—Hawaii and Caroline hotspots—are in a different hemisphere than the surface location of the hotspot in some seismic models. First, the surface location of the Hawaiian hotspots is located at 19° N at the Earth's surface, but the calculated plume conduit base is located in the southern hemisphere in plume advection models run in two global seismic models (SEMUCB-WM1 and TX2016) and in the northern hemisphere (but near the equator) in two other seismic models (SMEAN2 and S40RTS) (see plume conduit results in Jackson et al. (1)). Nonetheless, the latitude of the base of the plume conduit beneath Hawaii overlaps with the southern hemisphere within 2 SD uncertainty (see **Fig. 2** and **Dataset S1**). The surface location of the Caroline hotspot, at 5° N latitude, has a calculated conduit base that is located in the southern hemisphere in all plume advection models (1). All of the other hotspots explored in the study have plume bases that are calculated to reside in the same hemisphere as the modern surface expression of the hotspot.

Passive margins of the past billion years.

The following text provides a description for ancient rifted-passive margins used in our database. The ancient rifted-passive margins are labeled with a number (ID) that is used to identify the margin on the map (**Fig. S3**) and in **Dataset S3**.

Laurentia

1. Innuitian

Thick Late Mesoproterozoic to early Tonian platformal strata define the northern margin of Laurentia. Based on new dates and stratigraphy (12, 13), the Mesopoterozoic Borden-Bylot basins can now be linked to a series of intercontinental basins in northern Laurentia and Siberia, and have consequently been removed from the compilation.

The northern margin of Laurentia was intruded by the 719 Ma Franklin large igneous province (LIP) (14), which was associated with the separation of Siberia from Laurentia. However, the Innuitian margin does not preserve a Cryogenian to Ediacaran rifted passive margin. Late Ediacaran mixed carbonate and siliciclastic rocks of the Kennedy Channel Formation are present on Ellesmere Island(15), which may record reactivation of the margin. Broad deposition across the Arctic margin does not occur until after the early Cambrian (16), which we attribute to thermal subsidence, and place the rift-drift transition at 525 Ma (17).

The passive margin became a foreland basin with collision of the McClintock arc to the east (16). The earliest stratigraphic record of collision is a latest Ordovician to earliest Silurian (ca. 445 Ma) influx of orogen-derived turbidites in northernmost Greenland and Ellesmere Island (18). Foreland deposits persist through the Silurian. The suture occurred only in the NE segment and was translated modified by later sinistral motion along the margin. We extend the subduction of crustal material to the mantle for 12 Myr to 433 Ma along this arc-continent collision.

2. Victoria

In the Yukon, the Mackenzie Mountains, and Victoria Island, ~900 Ma rift-related clastics are overlain by ~820-780 Ma platformal carbonates. Extensional structures are present until about 815 Ma in the Yukon (19). For this segment, this may have been a successful rift from North China (20), and hence we take the rift-drift transition at 815 Ma, or North China may have been the conjugate to the western margin of Laurentia. The Victoria segment was intruded by the 719 Ma Franklin LIP (14) and then reactivated by latest Ediacaran to Cambrian rifting on both the northern and western margins. Because this collision was oblique and diachronous along the margin, we take the start date from the termination of collision on the Innuitian margin at 432 Ma to the end of the Silurian at 420 Ma. We separate this collision from the Ellesmerian orogeny, but acknowledge that these could be interpreted as a continuum with collision extending through the Devonian. As a strike-slip orogen, it is unclear if there was significant crustal material subducted to the mantle, and consequently we do not include this segment in calculations of subducted passive margin length.

3. North Slope

The North Slope terrane was displaced westward during the Paleozoic Innuitian and Ellesmerian orogenies (21), and is now in Arctic Alaska, where like the Victoria segment, 719 Ma plume-related magmatism was emplaced into a Tonian carbonate margin (22, 23). This is followed by Cryogenian to Paleozoic glacial and carbonate deposition, which records a series of failed or outboard rifts until a successful rift around the Ediacaran-Cambrian boundary (22, 24). In Arctic Alaska, passive margin termination is marked by a significant Upper Ordovician to Lower Devonian erosional unconformity, which we correlate with passive margin termination along the Innuitian margin (24).

4-5. Greenland & Svalbard

A vast thickness (12-15 km) of Tonian platformal strata define a rifted passive margin on the northeastern margin of Laurentia. In both northeast Svalbard and East Greenland, the Neoproterozoic successions begin with ca. 900 Ma rift-related clastic rocks, followed by Tonian platformal carbonates, ~1 km thick Cryogenian (717-635 Ma) successions, and thin early Ediacaran deposits (25, 26). The rift-drift transition was estimated at 815 Ma (25, 26). We define a diachronous onset of the Taconic-Caledonide orogenies between the Appalachians and the Arctic between 465 and 445 Ma, and take a 455 Ma onset age for the Greenland-Svalbard segment (27). We cut crustal contamination off at 443 Ma because Laurentia was the upper plate during the Caledonian orogeny with Baltica.

6-8. Appalachian

We divide the Appalachian margin into three segments that record the rifting of three separate cratons from Mesoproterozoic reconstructions of Rodina (28). The Scottish segment likely records the rifting of Baltica, the Northern Appalachian segment the rifting of Amazonia, and southern segment the rifting of Kalahari, and perhaps a later ribbon continent (29) such as Arequipa.

At least two pulses of plume-related intrusions of the Central Iapetan Magmatic Province (CIMP) were emplaced at ~615 and 590 Ma (30) between Laurentia, Baltica, and Amazonia. Rift-related volcanism occurred on the Appalachian margin of eastern North America between 562 and 550 Ma. The basal onlap on the distal cratonic margin are Middle Cambrian in age and we take a rift-drift age of 520 Ma for the Appalachian segment (31). Deposition in the Taconic forelands began by 465 Ma with arc-continent collision followed by slab breakoff and reversal (31), after which Laurentia was on the upper plate. We use these parameters for both the Scottish and northern Appalachian segments. For ease of visualization we place the Scottish segment on southern Greenland, but note that fragments are preserved in Scotland.

Tonian to Cryogenian rift-related magmatism dated at ~760-700 Ma is present on the southern Appalachian segment (32, 33), but is absent north of the New York promontory. A Cryogenian to Ediacaran passive margin sequence is absent suggesting this event was locally a failed rift or far-field. A feasible scenario is that Tonian-Cryogenian rift related magmatism records the rifting of Kalahari, which was separated from North America by another continental terranes, perhaps the Arequipa terrane, which rifted away along with Amazonia in the latest Ediacaran to Cambrian. Consequently, we take the onset of rifting at 760 Ma, but take constraints on the successful rift and terminal collision from the northern Appalachian segment.

During the Alleghenian orogeny with Gondwana starting at ~320 Ma, the composite Laurentian margin was on the lower plate. We attribute rapid exhumation at ~295 Ma (34) to be associated with slab-breakoff.

9. Ouachita

Rift-related magmatism in New Mexico and Texas spans from ~539 to 508 Ma (35, 36). The oldest platformal strata are latest Middle Cambrian, consistent with a rift-drift transition at ca. 500 Ma. Although the Ouachita-Alleghenian-Mauritanide belt does not preserve an ophiolite, vast sediment with volcanic debris was shed across North America and North Africa as well as tuffs found in these basins by ~320 Ma (37, 38), which we take as the termination date of the passive margin. Laurentia is interpreted to have been on the lower plate of a continent-continent collision with South America (39); we extend crustal contamination of the mantle for 40 Myrs to 280 Ma.

10-11. Cordillera
The Cordilleran margin of western Laurentia formed through two episodes of rifting, a Tonian-Cryogenian failed rift, and a successful Ediacaran-Cambrian rift (40-43). Extension, syn-sedimentary faulting, and rift-related volcanism began with the 777-719 Ma CHUMP (CHuar-Uinta Mountains-Pahrump) basins(44) and equivalents in Canada, which were deposited in narrow failed rifts (45). Rift-related volcanism persisted until 690 Ma (43, 46), and syn-sedimentary faulting and unconformities persisted throughout the Cryogenian (47, 48). There may have been a brief passive margin stage between 660 and 580 Ma recorded in the Mackenzie Mountain Supergroup(49), but the margin was reactivated at 570 Ma (50, 51). What appears as passive margin sedimentation in the aftermath of the Marinoan glaciation may be continued activity masked by the profound post-Snowball transgressions at ca. 660 and 635 Ma (51). The margin was reactivated during the late Ediciacaran, as marked by additional unconformities, basement derived grits, and basaltic volcanism (40, 52). The rift-drift transition was previously placed at the Precambrian-Cambrian boundary (41, 42), but recent geochronology on the craton suggest broad subsidence did not occur until ca. 508 Ma (53).

In the northern Canadian Rockies and adjacent Alaska, Devonian siliciclastic rocks of the Imperial, Tuttle, and Nation River Formations, and the Earn Group represent a foreland basin (54), starting by 387 Ma (55). Terrane suturing continued through the Late Paleozoic, but may have been offboard (56). The southern Cordillera collided with an arc terrane during the Devonian Antler orogeny. Convergence began offshore in latest Devonian and platform drowning is Early Mississippian (57), with the death of the passive margin placed at 357 Ma (55).

12. Brookian
The Brooks Range marks a Mesozoic arc-continent collision between the Anguyuchum arc and the passive margin of the Arctic Alaska microcontinent, which was rifted from the Middle Devonian (~390 Ma) to earliest Carboniferous (58). The rift-drift transition is marked by platform carbonates of the Lisburne Group, which are as old as ~350 Ma (55, 59). Arc-continent collision is marked by an influx of flysch from southerly sources, which began at 146 Ma (60). Exhumation ages from ca. 146-90 Ma are provided by deposition of foreland deposits on the North Slope that contain ophiolitic detritus (60). We extend crustal contamination in this oblique collision to 120 Ma to encompass shoaling in the foreland on the North Slope autochthon, which we associate with slab breakoff.

Baltica
13. Scandanavia
Plume and rift related intrusions of the Central Iapetan Magmatic Province (CIMP) were emplaced between 616 Ma (30) and rift-related dikes at 608 Ma (61). We place the rift-drift transition at 605 Ma and the end of the passive margin at 505 Ma with arc-continent collision in the Finnmarkian orogeny (55, 62). After arc-continent collision, the Baltican margin was subducted under composite Laurentia from ~435-415 Ma in the Caledonian orogeny (27). Thus, we mark crustal contamination from the subduction of Baltica between 505 and 415 Ma with a gap from 493-435 Ma.

14-15. Timanide
Mesoproterozoic to Tonian platformal carbonate and minor silciclastic rocks cover the East European Platform and are unconformably overlain by an Ediacaran siliciclastic sequence. The Mesoproterozoic and early Tonian units may represent an intercontinental basin or a rifted passive margin, but in either case it appears that the margin rifted again during the late Tonian, which was followed by late Tonian to Cryogenian passive margin deposition (63, 64). Narrow Late Tonian rift basins formed in Sweeden, which accommodated the Vasingso Group and contain microfossils that have been correlated with 780-730 Ma assemblages in western North America (65). We

interpret these interior basins as the manifestation of a successful rift and rift-drift transion at ~750 Ma.

A ~670 Ma ophiolite was obducted during the Timanide orogeny (66), which extended through the Ediacaran to ~530 Ma (67). We mark arc-continent collision by the appearance of 630-590 Ma detrital orthoclase in ca. 610-590 Ma strata that unconformably overlie Tonian units, and the presence of 609-571 Ma detrital phengite (67). Following slab-breakoff and reversal, the main phase of the Timanide orogeny occurred as an accretionary orogeny with Baltica in the upper plate. The Timanide orogeny and active margin continued through the Paleozoic (67).

16. Uralian 1&2
Upper Cambrian to Lower Ordovician rift facies date the onset of rifting of the Paleozoic Uralian margin to ~500 Ma (68), with a rift-drift transition at 477 Ma (55). The remnants of the Early Paleozoic subduction-accretion complexes occur in a belt between the East European and the West Siberian cratons (69). Magmatism and ophiolite generation in the Magnitogorsk arc and equivalents spans 488-392 Ma, with Baltica continental crust entering the subduction zone by 380 Ma and foreland deposition between 375-359 Ma during the early Uralian arc-continent collision (68). We extend arc-continental-terrane collision between Baltica, the Magnitogorsk arc, and Kazakhstania from 380-359 Ma. Additional subduction of the amalgamated Baltica and Kazakhstania likely occurred during the late Uralian orogeny with the final arrival of Siberia, with Siberia on the upper plate. Starting at ~300 Ma, Siberia collided with the eastern margin of the amalgamated arc terranes and Baltica forming the Permo-Carboniferous Uralian suture (70). We bracket continent-continent collision with deposition within the Uralian foreland basin from the Cisuralian to Capitanian (71) (300-260 Ma).

17. Tornquist
Half grabens imaged in Poland have been correlated to the basal Ediacaran stratigraphy in drill core (72). We take a rift age of 616-550 Ma after CIMP magmatism and the 551 Ma tuff at the top of the rift sequence to mark the rift-drift transition (72). An unconformity between the Middle Cambrian and the Ordovician is likely related to the Finnmarkian orogeny of the Scandanavian margin. Sedimentation continued through the Ordovician, with the Late Ordovician closure of the Tornquist Sea and collision of Avalonia along the Thor suture (73). Seismic data and the absence of any subduction related magmatism on the Baltica margin other than air-fall ash deposits suggests subduction towards the southwest (74). We place the end of the passive margin 450 Ma with Ordovician units succeeded by a Silurian foreland basin to 422 Ma, that was further metamorphosed by Scandian-Acadian deformation and later strike-slip motion (74).

18-20. Avalonia
Rifting of Avalonia began as a backarc rift during the Ediacaran at 595 Ma (75) and culminated with an early Cambrian cover sequence (76). The arrival of Avalonia to the Appalachian margin created the 421-400 Ma Acadian orogeny in North America and Europe, in which Avalonia was subducted under North America (77).

Alpine-Himalaya
21. Variscan
Rifting of the Amorica spanned 419-407 Ma in the Rheno-Hercynian Zone with a passive margin end date at 347 Ma (55). This was followed by the collision of Gondwana, which created Hercynian-Variscan foreland basins beginning at 340 Ma in the Czech Republic (78) that remained active into the Westphalian (304 Ma) in South Wales (79) through the Stephanian (299 Ma) in Germany (80) and from the Middle Variscan through the Sephanian (~335-300 Ma) in Poland (81). Final collision and exhumation is marked by the emplacement of 330-300 Ma post-kinematic granites (82). We cut off the collision between Avalonia and Amorica at 330 Ma, and assign the later forelands and deformation to the collision with Gondwana.

22. Saxo-Thuringia

The Saxo-Thuringian margin of Armorica was part of Gondwana during the early Paleozoic and includes Cambrian conglomerates and Lower Ordovician mafic volcanic rocks (82, 83). We pick an onset of rifting at 500 Ma with a passive margin defined from 444 Ma to 330 Ma. Collision in the Variscan orogen continued until ca. 300 Ma (82).

23. Alpine
Permian to Triassic rifting in western Europe was followed by a rift-drift transition at ~170 Ma with a passive margin duration from 170-43 Ma (55, 84). Ophiolite generation in the Mesozoic to Cenozoic Alpine-Pontide belt occurred predominantly from 170-140 Ma (e.g. Betic, Chenaillet, Zermatt-Saas, External and Internal Ligurides, Calabrian, Corsica, Mirdita, and Pindos), during opening of the Alpine-Tethys Ocean (85). Subduction related metamorphism began in the Alpine Tethys by the Valangian (140-133 Ma) with uplift and erosion of the ophiolites above the Iberian plate and Eurasia primarily from 50-30 Ma (86), and we cut off passive margin subduction at the end of this interval.

24. NW Iberia
NW Iberia preserves a passive margin duration from 475-385 Ma (87), with the demise of the passive margin in the early stage of the Hercynian orogen. This margin may have been much more extensive but is largely overprinted by Alpine metamorphism. Exhumation extends to 365 Ma (87), which we attribute to slab-breakoff.

25. Greece Pindos
A passive margin formed on the Apulian microcontinent from 230-60 Ma (55), and we extend the onset of rifting to 250 Ma and collision from 60 to 40 Ma (88), as an early Alpine suture.

26-27. Isparta
A passive margin developed on the East Isparta margin from 227-53 Ma, and on the West Isparta segment from 227-60 Ma (55). We extend the onset of rifting to the Permian-Triassic boundary and end the collision at 35 and 40 Ma, respectively, with closure of the northern Sakarya zone, which formed a north-dipping Triassic subduction-accretion zone on the northern margin of the Paleo-Tethys (89), which was incorporated into the Pontides suture and uplifted from the Maastrichian through the Eocene (90). Since the Miocene, this suture zone was reactivated as part of the Inner Taurus and Zagros belts, and we continue passive margin subduction to the present.

28. Oman-Zagros
A passive margin formed on the northeastern margin of Arabia from 272-87 Ma (55). Mesozoic Pan-Arabian ophiolites formed in a supra-subduction zone setting (e.g. Troodos, Kizildag, Semail, Neyriz, Nehbandan, Muslim Bagh, and Waziristan) from 125-90 Ma (91) and were thrust onto Africa and Arabia during the mid-Turonian to latest Campanian (87-72 Ma) Ayyubid orogeny (92-94). As an arc-continent collision, we extend the passive margin death 12 Myrs from 87 to 75 Ma.

29. N. Iran
The Paleo-Tethys opened during the Ordovician, subduction was initiated by the Devonian, and it closed from the Permian to Triassic with the diachronous collision of the Cimmerian ribbon continent in the Eo-Cimmerian orogeny. Middle Ordovician to Middle Devonian volcanic rocks have been attributed to rifting, with a 390 Ma rift-drift transition (55). An active margin developed on the southern Turan margin through the Permian with collisional arc deposits appearing on Iranian passive margin in the Triassic (95). Initial Eo-Cimmerian collision started at ~227 Ma, with slab-breakoff at ~200 Ma, and backarc rifting at ~180 Ma (95).

30. Himalayan I
The Lesser Himalaya preserves a Cryogenian rift followed by an Ediacaran to Cambrian passive margin sequence. We define a rift starting at 650 Ma and a passive margin from 635-502 Ma (55). Arc-continent collision terminated at 490 Ma prior to the development of an Ordovician active margin (96)

31. Himalayan II

For the younger Himalayan margin, rifting occurred between 330 and 271 Ma, and arc-continent collision began by 52 Ma along the Indus-Tsangpo and Shyok sutures (97), marked by the appearance of young volcanic material on the Indian margin (98). However, after the initial arc-continent collision, the subduction zone stepped north and consumed the Kshiroda plate (99, 100) until collision between India and Eurasia starting at 40 Ma (97). We continue passive margin subduction through the continent-continent collision, which started at ~41 Ma (97) and continues to the present. Thus, we combine the subduction of Indian crust in two events starting with the arc-continent collision from 52-41 Ma and the continent-continent collision from 41 Ma to present.

32-33. Karakorum-Qiantang

The Karkorum block is the western extension of the Qiangtang terrane west of the Altyn-Tagh Fault. The West Jinsha suture is defined by the Triassic Yushu mélange between the Qiangtang terrane and the Songpan-Garze belt (101). A passive margin existed on the northern margin of the Qiangtang terrane from the Cambrian through the Permian, and was reactivated during the Permian with the rifting of a ribbon continent on the southern margin by the Early Permian (ca. 299 Ma). Magmatism within the oceanic tract is largely Permian in age (101). Subduction of the northern margin began by 230 Ma (101, 102), after which an active continental margin was established by 210 Ma.

Siberia

34. Taimyr

It was previously proposed that a Tonian ophiolite and arc collided with the Mesoproterozoic Taimyr margin at ~650 Ma (66, 103). However, recent geochronology suggests that the Siberian margin was active after ca. 900 Ma and that ca. 730 Ma ophiolites formed in a back-arc and were accreted and exhumed during the Ediacaran (104); consequently we do not include the early Taimyr passive margin (55). After Ediacaran accretionary orogenesis the Taimyr margin was re-rifted in the late Ediacaran to early Cambrian with a rift-drift transition at ~525 Ma (105). A late Paleozoic orogeny was dated by Late Pennsylvanian to Early Permian thrusts and Permian granitic plutonism and metamorphism in the central Taimyr zone (106, 107). This orogeny is considered a continuation of the Uralian suture. We date the onset of collision at 288 Ma with the age of the youngest supra-subduction granites (107). Ar-Ar ages of ~272 Ma represent termination of Late Paleozoic collisional tectonic activity within Northern Taimyr (107).

35-36. Yenisei

The Yenesei margin of Siberia rifted sometime after 1100 Ma to accommodate the Stenian to early Tonian Tungusik Group (108). Peak metamorphism of the margin occurred between 895-855 Ma (109). We define the passive margin from 1050-895 Ma. The margin then re-rifted between 800-790 Ma (110) with passive margin development by 715 Ma (109) to accommodate Cryogenian glacial deposits in the Chivda Formation (111). The margin then became active again with 630-610 Ma arc-continent collision with the Isakovaka arc (109, 112).

37. Cis-Patom-Baikal

Cyrogenian magmatism associated with the Olokit rift occurred between 730-650 Ma (113), likely associated with separation from the northern margin of Laurentia. Passive margin deposits include Marinoan age ~645-635 Ma glacial deposits (114). The Neoproterozoic Baikal-Muya belt collided with the southern margin during the Edaicaran with foreland deposits that include the ca. 570 Ma Shuram excursion (114). We use the foreland to define passive margin subduction of the southern margin of the Siberian craton from 580-560 Ma. Cambrian to Ordovician oblique collisions along the southern margin of Siberia mark the subsequent accretion.

38. Verkhoyansk

Previous compilations defined three separate rifted passive margins on the eastern margin of Siberia (55). The first margin started at ca. 1600 Ma and ended at ca. 1010 Ma. This appears to be way too long-lived for a single passive margin and there is no record of a collision outside of what is interpreted as a foreland. The older succession could instead be part of the broad

Mesoproterozoic intercratonic basins that formed on Siberia and Laurentia. If there is a Mesoproterozoic rifted passive margin, it is in the ca. 1100 Kerpyl Group, which lies unconformably over Lower Mesoproterozoic strata. Depending on the reconstruction, the eastern margin may have faced the Grenville orogen and all of the Late Mesoproterozoic units could be related to foreland deposition. Instead we interpret these successions to represent an intercontinental basin succeeded by distal foreland deposits of the Grenville.

Rifting of the eastern margin started at 543 Ma with a rift-drift transition at 523 Ma (115). This margin was reactivated with the emplacement of the Yakutsk LIP and separation of a ribbon continent at ~380 Ma and ended at 146-126 Ma (116); because this margin was reactivated instead of terminated, we do not demarcate a separate passive margin death. We continue the Anguychum suture through to Chukotka, the South Anyui suture, and the Verkhoyansk of Russia, but because constraints are lacking in these belts, we largely use the parameters from the closure of the Anguychum Ocean. In the Verhoyansk, a Jurassic collision between the Mesozoic Alazeya arc and the Omelevka microcontinent is lined with ophiolites and created the Kolyma-Omion microncontinent, which was subsequently thrust over the Siberian margin (116).

Asia

39. Khubsugul-Zavkhan

We combine the Gargan margin with the Khubsugul and Zavkhan margins of Mongolia, which we interpret to have formed on the Tuva-Mongolia microcontinent that was exotic to Siberia until the Paleozoic (117). The passive margin formed during latest Tonian to Cryogenian rifting and ended with the collision of the Khantaishir-Agardhag arc between 545 and 525 Ma (117, 118). Previous compilations also included the Idermeg terrane (119), but we find this margin too poorly constrained. Additionally, we interpret the Bayankhongor ophiolite as an oceanic plateau along an accretionary margin and do not use it as a constraint on a passive margin termination.

40. Tianshan-North Tarim

Volcanic rocks in the Quruqtagh Group on the northern margin of the Tarim craton have been dated between ~740 and 615 Ma and interpreted as a rifted passive margin (120), although others have interpreted the margin as a back-arc rift and long-lifted accretionary margin (121). Nonetheless, we place the rift-drift transition at 615 Ma and the initial collision at 455 Ma marked by an unconformity and influx of siliciclastic detritus (122). A 440-390 Ma belt of arc magmatism in the Tianshan and northern Tarim records the establishment of a south-dipping subduction zone under the Tarim by the Silurian, which was followed by Silurian-Devonian back-arc extension and accretion of the Yili block (123).

41. Kunlun

The Neoproterozoic stratigraphy on the southern margin of the Tarim block appears to mirror that on the northern margin, and consequently we follow constraints from the Quruqtagh for the rift and drift. Previous compilations defined the end of the passive margin at 430 Ma (55), but we instead suggest that this is a successor foreland basin associated with the collision of the and that the peripheral foreland associated with collision of the South West Kunlun arc terrane formed along the Kudi-Altyn suture from 475-455 Ma (124). We assign the later collision to the subduction of composite Qilian-Qaidam-North Qinling and North China block below the Tarim block (125).

42. North China

Tonian basins were deposited across North China (126) above the ~970-890 Ma Xuhuai rift system. These basins were re-activated during the Cambrian and succeeded by Late Ordovician foreland deposits (127). We define the passive margin from 890-455 Ma, and termination with the collision of the Erlangping ophiolite. The Erlangping suture between an Early Ordovician oceanic arc and the North China craton, slightly proceeds the Qilian suture, with collision over by 435 Ma (128). We place the subduction of North China below these terranes from 455-435 Ma.

43-44. Longmen Shan and Qinling-Dabie

After collision and accretion of the Yangtze and Cathaysia blocks by 810 Ma, the northwestern margin of the South China craton became an active margin through much of the Cryogenian. By the latest Cryogenian, the southern margin of the Yangtze block had developed into a rifted passive margin, perhaps through back arc rifting, however, we find the Ediacaran northern margin of South China too poorly constrained to define as a passive margin (55). Active Tonian to Cryogenian arc magmatism on the northwest margin suggests the margin may instead have been formed by back-arc extension. We attribute Cambrian-Ordovician strata to the southern margin, and define Silurian rifting for the northern margin (129), and a passive margin by 400 Ma. The margin was reactivated at 300 Ma (55), and the passive margin ended with the Dabie-Sulu orogen starting at 228-210 Ma. The Dabie-Sulu suture was exhumed in the late Triassic to Jurassic (228-210 Ma) during the final collision between North China and South China (130), and extends east to Korea (131).

45. Nanling

Rifting on the southern margin of the Yangtze block occurred during the Sturtian glaciation culminating with horst and graben structure capped by the post-Sturtian transgression. Thus, we define rifting from 720-660 Ma. Termination of the passive margin occurred by 450 Ma with putative distal retro-arc foreland basin deposition associated with the Kwangsian orogeny (132, 133). However, it appears this margin was never subducted but instead reactivated in a back arc to accretionary setting after establishment of east dipping subduction outboard, and consequently, we do not include the Nanling segment in the calculation of subducted passive margin length.

46. Taiwan

A passive margin developed on Taiwan from 28-6 Ma (55). Taiwan is one of the best-constrained examples of active arc-continent collision and subduction polarity reversal. Collision began at 6 Ma and exhumation has accelerated over the past million years (134).

Australia

47. Timor

Rifting had started on the northwest margin of Australia by the latest Triassic with a rift-drift transition at 151 Ma (55). The passive margin end date is about 4 Ma and the collision of the Banda arc continues today (135).

48. New Guinea

Arc-continent collision began in New Guinea during the Late Oligocene to Early Miocene above a north-dipping slab (136-138). Two major ophiolite belts—the Irian-Marum ophiolite belts (including the April ultramafics), and the Papuan Ultramafic Belt (PUB)—are preserved along the Central and Peninsular Range. Exhumation of the Irian ophiolite began in the middle Miocene (16-14 Ma), and uplift in the Central Range accelerated from the Late Miocene to Pliocene (139). Although the PUB was generated and obducted earlier than the ophiolites in the Central Range (140, 141), it was also exhumed very rapidly over the past 10 Ma (137).

49-50. Centralian & Adelaide

When Australia rifted from Laurentia during the Tonian, basins formed throughout Australia, and a rifted passive margin developed on the eastern margin (142). We include the Kimberley with basins of Central Australia. Rift-related magmatism has been dated between 825-750 Ma, and we pick the rift-drift transition at 750 Ma (143). Collision between North and South Australia in the Paterson-Peterman orogeny created large-scale metamorphism and foreland deposition between ~570-530 Ma (144), which was manifested in the influx of siliciclastic material in the Georgina Basin (142). Peak metamorphism occurred between 550-530 Ma above a south-dipping slab (145). On the Adelaide margin, we associate canyon cutting in the ~570 Ma Wonoka Formation to be associated with disruption of the passive margin, followed by an influx of clastic material in the Pound Group from developing highlands to the northwest (146). However, it appears this margin was never subducted but instead reactivated in a back arc to accretionary setting after establishment of east dipping subduction outboard in the Ross-Delamerian orogeny (147). Consequently, we do not include the Adelaide segment in the calculation of subducted passive margin length.

51. Tasman
The western rifted margin of Australia continues to Tasmania and hosts Tonian to Cryogenian deposits of the Black River Group (148). Volcanic rocks of the Rocky Cape Group and equivalents formed between ~582-575 Ma (149), which we associate with back-arc rifting and consequently we cut passive margin sedimentation off earlier in this segment at 600 Ma. In the Ross Orogen of Antarctica, an active arc was established by 565 Ma (150). In Australia, the Delamerian orogeny formed from 520-490 Ma due to accretion of an outboard arc (147), with peak metamorphism in Tasmania between 520 and 508 Ma (151). Like the Adelaide segment, there is no evidence for subduction of the passive margin, so we do not include this in the calculation.

Central and South America
52. Cuba
Cuba hosts a carbonate-dominated Mesozoic sequence that formed during the break-up of Pangea with a rift-drift transition at ca. 159 Ma (55). Volcaniclastics from the Greater Antilles arc appeared on the margin at ca. 80 Ma. We extend the rift to 200 Ma to encompass Jurassic volcanism and subduction of the margin until 60 Ma (152).

53. Venezuela
Rifting of Pangea began with the ca. 200 Ma Central Atlantic Magmatic Province, and we follow Cuba for the rift-drift transition at ca. 159 Ma (55). The transition from passive margin to a foredeep is defined by an increase in subsidence at ~34 Ma (153), and passive margin subduction until 8 Ma.

54. Araras, Paraguay
Rifting occurred during the Marinoan glaciation, forming grabens filled with glacial deposits and iron formation. We define rifting from 645-635 Ma. The SE margin of the Amazon craton is marked by the 540-500 Ma Paraguay and Araguaia belts (154), which are separated from the Goias magmatic arc by the Transbrasiliano Lineament. This marks the continent-continent collision between the Amazon, West Africa, and Sao Francisco cratons. The SE margin of Amazonia has alternatively been interpreted as an active continental arc throughout most of the Neoproterozoic (155), however, the Goais arc formed as an inter-oceanic arc that collided with the Sao Francisco craton and there is no evidence for subduction under Amazonia at this time (156). The continental arc likely formed on the Sao Francisco craton from ~630-560 Ma, after ~650-630 Ma collision with the Goias arc.

A Cryogenian rifted passive margin deposit with a Marinoan cap carbonate is present in the Paraguyay Belt (157). This early Ediacaran succession is unconformably overlain with 550-540 Ma foredeep deposits of the Tamengo and Buaicurus formations(158) and early Cambrian foreland deposits of the Diamantino Formation (159). Deformation and metamorphism is bracketed by 518 Ma undeformed granite (159).

55. Iapetan margin of Amazonia
The Iapetan margin of Amazonia is poorly represented in heavily deformed para-autchthonous belts of the Maranon complex, but is preserved in part in Late Ediacaran to Cambrian sequences that unconformably overlie basement and Cryogenian strata near the Bolivia-Brazil border. We pick CIMP rifting from 616 to 570 Ma (30). The margin ended with the Ediacaran-Late Cambrian oblique collision of the Pampean terranes and Arequipa from 545-520 Ma (160).

56. Arequipa
Arequipa formed as a ribbon continent between Laurentia, Amazonia, and the Kalahari craton during the Cryogenian (161). Unconformities developed until an Ediacaran carbonate platform blanketed the outcrop belt. We place the rift-drift transition at ~630 Ma. The margin was drowned by siliciclastic sedimentation between 545 and 520 Ma (160).

57. Precordillera

Rifting between the Precordillera and the southern margin of North America occurred between ~539-508 Ma (35, 36). The oldest platformal strata are latest Middle Cambrian, consistent with a rift-drift transition at ca. 500 Ma. Foreland deposition began in the Early Ordovician and continued through the Ordovician (162).

58. West Sao Francisco
The Brasiliano orogeny involved a collision between the Bambui platform on the west side of the Sao Francisco craton, and terranes to the west. Extension-related magmatism in the Sao Francisco craton has been dated at 906 Ma and between 800-760 Ma, and interpreted as a back-arc rift of the Goais block from Sao Francisco (163). These are overlain with a passive margin sequence that includes Sturtian age glacial deposits (164). The Brasiliano orogeny involved a collision between the Bambui platform on the west side of the Sao Francisco craton, and terranes to the south and west including the Goais arc and the Paranapanema block. Magmatic ages in the Goias arc come in two major pulses, one from ~890-860 Ma and a second between ~670-600 Ma (165). U-Pb zircon dates on metamorphic overgrowths constrain high-grade metamorphism along the eastern boundary of the Goais massif at 760–740 Ma (166). Peak metamorphism in the Brasiliano belt was between 650-610 Ma (167). We interpret 760-740 Ma metamorphism to record arc-terrane collision off-board, which was followed by 630-610 Ma continent-continent collision with the Paranapanema block and termination of the passive margin.

59. East Sao Francisco
For rifting, we follow constrains from West Sao Francisco. The Socorro and Serra da Bolívia magmatic arcs collided with the already amalgamated Paranapanema-São Francisco plates between 620 and 605 Ma (168). This was followed by accretion of the Rio Negro magmatic arc of the Oriental terrane between 605 and 595 Ma. Widespread generation of crustal melts associated with collision is represented by foliated granitic plutons, dated between 610–565 Ma (168). Although collision of the Riberia and Dom Feliciano belts certainly overlapped, we associate collision of the Socorro and Serra da Bolívia magmatic arcs with the Dom Feliciano suture, and take the Ribiera suture from 610-590 Ma. This was followed by oblique continent-continent collision with Congo through the early Cambrian in which Sao Francisco and Rio de la Plata were on the lower plate (169), and consequently we extend subduction of the margin until 540 Ma.

Africa
60-62. Sierra de la Ventana, Cape Fold Belt, Ellsworth Mountains
In the Cape belt, Middle Cambrian rift deposits are overlain by an Early Ordovician to Carboniferous passive margin sequence (170). Foreland basin deposits of the Karoo Group formed between 300-280 Ma (171). This margin has been correlated with equivalent units in the Sierra de la Ventana belt in Argentina and the Ellsworth Mountains of Argentina (55).

63. East margin of West African craton
A Neoproterozoic rifted passive margin developed on the eastern margin of the West African craton between 1000-635 Ma, which preserves a ca. 635 Ma basal Ediacaran cap carbonate in the Volta Basin (172). Neoproterozoic ophiolites of the Buem belt were exhumed after ~710 Ma in an arc-continent collision (173, 174) associated with 620-602 Ma UHP metamorphism (175). We take these ages as the best constraint on exhumation during arc-continent collision in the Dahomeyide belt. These are overprint by ~601-570 Ma metamorphism related to transpressional contintent-continent collision with the Nigerian Shield(175).

The Trans-Saharan continent-continent collision between the West African craton and the Tuareg-Nigerian shield occurred between 601-567 Ma, as marked by migmitization and foreland basin development (175). A maximum age on foreland deposition comes from a 601 Ma tuff directly below the main foreland basin succession in the Oti-Pendjari Group of the Volta Basin(176). A 601-567 Ma collision is further consistent with 586-567 Ma Ar-Ar and titanite ages from within the Dahomeyide thrust stack (177).

64. North margin of West African craton

In the Anti-Atlas belt, on the West African Craton, south of the Anti-Atlas Major Fault, 2200-2030 Ma basement is overlain by volcaniclastic rocks of the Taghdout Group and Tachdamt Formation, which form the lower portion of the Anti-Atlas Supergroup and have been dated at ~883 Ma (178, 179). Volcanic units have sub-alkaline to tholeiitic geochemical signatures, which have been interpreted to record the development of a volcanic rifted passive margin (180). North of the Anti-Atlas Major Fault, the Sirwa and Bou Azzer ophiolites have been dated between 762-759 Ma (181, 182). Crustal thickening and a magmatic lull from 730-710 Ma has been related to arc-continent collision between the Sirwa and Bou Azzer ophiolites and the West African craton above a north-dipping subduction zone (183). After collision, an active continental arc was established in Morocco by 710 Ma (183) and on crustal fragments of Cadomia and West Avalonia through the Early Ediacaran, followed by Late Ediacaran backarc rifting of the Cadomian arc (184).

65. West margin of West African craton

A late Mesoproterozoic rift accommodated the ~1100 Ma Atar Group in Mauritania (185). The margin was reactivated with a thick Tonian siliciclastic sequence in the Assabet Group, which coincided with rifting of the northern margin and potentially collision on the southwestern margin (186). We follow constraints from the northwest margin of West Africa and propose that the margin terminated with an arc-continent collision between 730-710 Ma. In allochthonous units, initiation of subduction is defined by the ~710 Ma Gorgol Noir ophiolite (187), which we associate with the transformation of the margin to an active arc. The Bassaride-Rokelide belt of Guinea, Sengal, and Sierra Leon, extends into the Souttouf belt of Western Sahara where there is extensive 660-650 Ma metamorphism (188, 189). In Mauritania, an unconformity at this level is overlain by 640-635 Ma Marinoan glacial deposits (190). In the Souttouf belt, metamorphic ages associated with accretion cluster between 610-590 Ma (191).

66-67. Northwest Congo-North Sao Francisco

Neoproterozoic metasediments and granites are preserved on the northwestern margin of the Congo Craton in the Central African Fold Belt. Granites have been dated between 641-613 Ma and metamorphism between 620-610 Ma marks the demise of the margin (192). The margin extends to the NW margin of the Sao Francisco craton and was reactivated as a dextral transcurrent margin at ca. 570 Ma. On the Sao Francisco craton, rifting occurred at 806 Ma (193) and accommodated deposition of Cryogenian strata of the Vaza Barris Group (194). A Tonian rift basin is present in the Lower Dja Series in Cameroon, which is overlain by Cryogenian passive margin deposits of the Mintom Formation (195). We take rifting at 806-750 Ma, passive margin deposition to 620 Ma, and subduction of the passive margin to 600 Ma.

On the northern margin of the Sao Francisco craton the ~820 Ma Monte Orebe ophiolite is associated with an ocean-continent transition (196). The passive margin includes both Cryogenian glacial deposits and cap carbonates (197), suggesting deposition until at least 635 Ma. An external arc was active from 650-610 Ma (198) with syn-orogenic metamorphism between 610-595 Ma. We take foreland deposition related to continent-continent collision from 615-595 Ma. The Sergipano belt extends to the Rio Preto belt on the NW margin on the Sao Francisco craton and the Oubanguides in Cameroon (199).

68-69. Southwest margin of the Congo

The western margin of the Otavi formed rifted between 770 and 655 Ma, and terminated with Ediacaran collision of the Outjo block and foreland deposition (200). In the Coastal Terrane, peak metamorphism occurred from 650-640 Ma (201), which we suggest is associated with relict subuduction and pre-collisional. Collision is dated by ca. 580-570 Ma syn-kinematic metamorphic granites and 590-570 Ma molasse of the Mulden Group. After the main phase of collision, transcurrent slip and erosion continued from 570-530 Ma, which was followed by rapid exhumation and thus presumably erosion during transtensional reactivation 525-520 Ma (201).

70. Zambezi-Mpanshya

Rift-related magmatism in the Zambezi belt extended from 804-735 Ma, with a passive margin from 735-585 Ma (202). Eclogite in the West Zambezi Belt indicates that subduction was underway by

~659-638 Ma (203). Metamorphic ages constrain ocean basin closure and collision of the Congo and Kalahari cratons by ~585-565. Collision within the Zambezi Belt was ~10-30 Myr before collision in the Damara Belt at ~555-550 Ma (202).

71. Karasuk

In Uganda, a passive margin is preserved in the Karasuk Supergroup with less deformed equivalent strata inboard in the Malagarasi Supergroup, which include Cryogenian glacial deposits of the Bunyoro Group (204). The West Granulite belt, is a continuation of the Malawi suture between the amalgamated ANS terrante and the Tanzania/Congo craton (202), and is marked by the Sekker and Moroto ophiolites. The West Granulite belt records two pulses of high PT metamorphism at ~657-639 Ma and ~635-615 Ma followed by 575-525 Ma sinistral transpression (202). We interpret the 657-639 Ma dates to mark exhumation on the West Granulite suture and the 635-615 Ma dates to record final amalgamation and collision in the East Granulite belt.

72-73. Northwest and northeast margins of the Kalahri

Like the southern Congo margin, rift-related magmatism was widespread after ~805 Ma (202), with passive margin sequences deposited between ~720-570 Ma on the Kalahari craton. On the northwest margin, collision occurred between ~570-515 Ma as defined by the youngest ages from the basal Sijarira Group (202). After collision of the Zimbabwe promontory, the Kalahari craton rotated clockwise and closed the Khomas Ocean during the 555-515 Ma Damara Orogen (202). We define the passive margin termination with deposition of the ~555-535 Ma Nama foreland basins, with metamorphism continuing through ~515 Ma with Kalahari on the lower plate, subducting below the Congo.

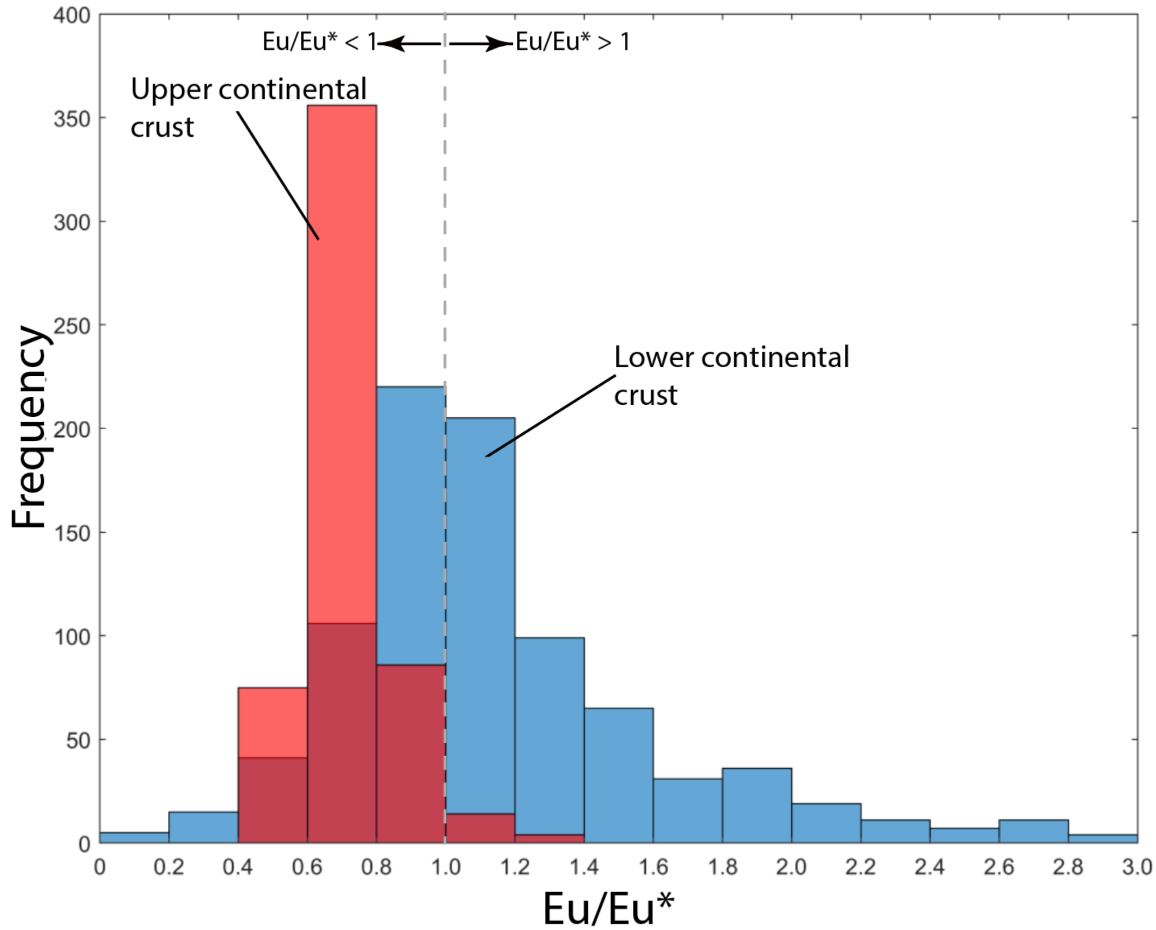

Figure S1. The distribution of Eu anomalies for a compilation of upper continental crust rocks is compared to the Eu anomalies for lower continental crust rocks. A database (205, 206) of granulites (representing lower continental crust) and glacial tillites, loess, greywacke and shale (representing upper continental crust) shows that both continental crustal types exhibit considerable overlap in Eu/Eu* values (Eu/Eu* = $Eu_N/(Sm_N * Gd_N)^{0.5}$, where N represents normalization to primitive mantle from elsewhere (207)), and both type of continental crust exhibit high Eu/Eu* (>1) and low Eu/Eu* (<1) values. Low Eu/Eu* values (i.e., Eu/Eu* < 1) from subducted upper continental crust have been argued to be present in the mantle sources of EM2 OIB, and high Eu/Eu* values (i.e., Eu/Eu* > 1) from lower continental crust were argued to be in EM1 OIB (208), but the overlap in Eu/Eu* between upper and lower continental crust, and Eu/Eu* > 1 in examples from both upper and lower continental crustal rocks, indicate that Eu/Eu* cannot be used to distinguish between recycled upper and lower continental crust contributions in OIB. Note that the distribution of lower continental crust rocks exhibits a long tail of infrequent high Eu/Eu* values that extend off the range shown in the figure.

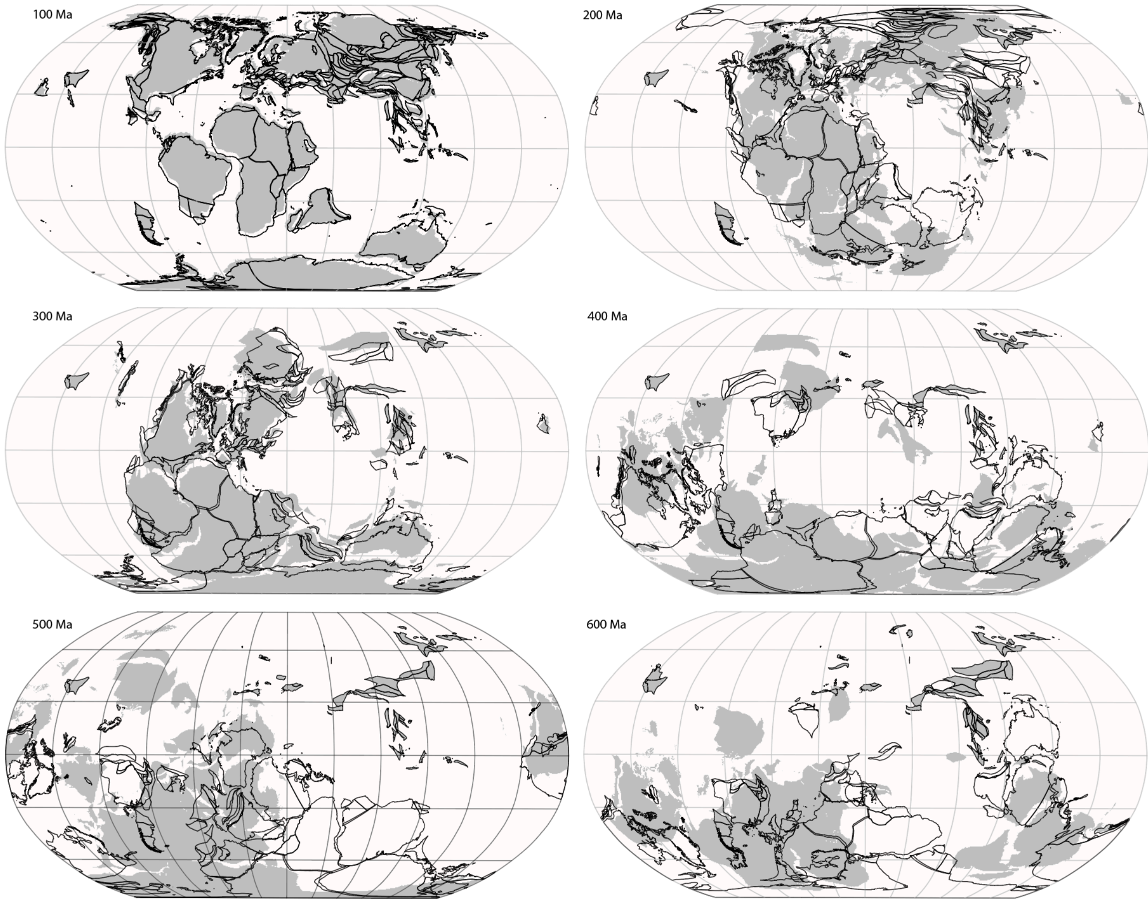

Figure S2. Paleogeographic reconstructions at 100 Myr snapshots back to 600 Ma in mantle reference frame (grey) and paleomagnetic/spin-axis reference frame (black outlines) using rotation files of Torsvik & Cocks (209). Reconstructions were constructed in GPlates with the central meridian set at 30 degrees. For this comparison, the Torsvik & Cocks (209) reconstruction was used because it contains both mantle and paleomagnetic/spin-axis reference frames for the past 600 Ma, whereas the Merdith et al. (210) reconstruction for the past 1000 Ma has only a paleomagnetic/spin-axis reference frame. Nonetheless, the Torsvik & Cocks (209) reconstruction demonstrates that, independent of what reference frame is used, Gondwana and Pangea were constructed predominantly in the southern hemisphere.

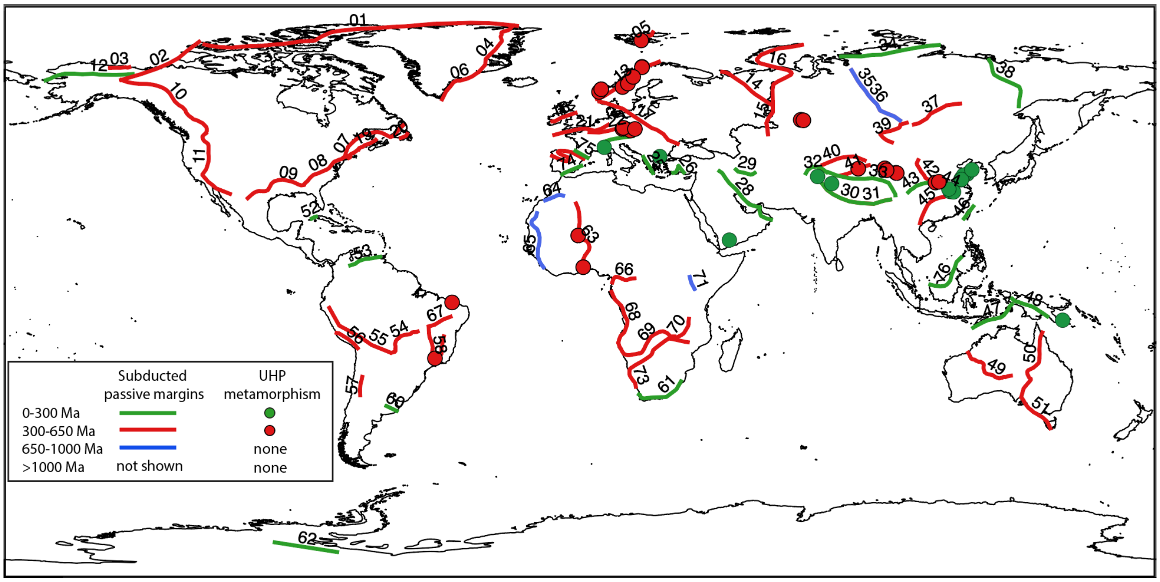

Figure S3. Passive margins and UHP continental metamorphic occurrences plotted on present geography. UHP oceanic metamorphic occurrences are not shown. Passive margins are color coded by age and labeled with their ID numbers as listed in **Dataset S3** and described in the **SI Appendix**. Occurrences of UHP continental metamorphic terranes are shown, color coded by age. Data are from a compilation published elsewhere (211). Passive margin shapefiles are available in the **Dataset S4.**

Dataset S1 (separate file). Data for 58 known hotspots summarized from Jackson et al. (1). The data include surface locations of hotspots, locations for the bases of advected plume conduits at 2850 km (where locations represent averages across four models), average plume conduit distances from the LLSVPs at 2850 km, and hotspot buoyancy fluxes.

Dataset S2 (separate file). Area normalized paleolatitude from 1000-520 Ma. Continental areas were calculated in QGIS, including each of the major cratonic blocks larger than Nigeria-Benin; smaller continents were not included because of uncertainties in their size and paleolatitude (see Methods text). Latitude was extracted from the latitudinal midpoint at 5º at 20 Myr intervals from Merdith et al. (210), with modifications following Eyster et al. (212). See Torsvik et al. (213) for 540-0 Ma.

Dataset S3 (separate file). Passive margins of the past billion years, described in **SI Appendix** text by ID number with references. Passive end is equivalent to collision start. Continent and Plate ID are used for paleogeographic reconstruction in GPlates. Facing direction is the direction of passive margin subduction at the beginning of the orogen. Paleolatitude of the margin at the passive margin end date is to the nearest 5 degrees. Data are used to calculate passive margin lengths in **Dataset S5**.

Dataset S4 (five separate files). Five separate files for use in GPlates software. These files provide the shapefiles for passive margins. The shapefiles are used to generate passive margins that are compiled in **Datasets S3** and **S5**.

Dataset S5 (separate file). Summed length of passive margins and passive margin terminations. Passive margins are calculated in 5 Ma intervals between start and end date. Passive margin terminations are calculated in 5 Ma intervals between passive margin end and collision end date, from **Dataset S3** and the **SI Appendix**. Length in southern or northern hemisphere designates the hemisphere in paleogeographic reconstruction at the time of passive margin end date.

Dataset S6 (separate file). Low temperature/pressure, ultrahigh pressure metamorphism (211) with reconstructed paleolatitudes at 5° resolution from GPlates using Plate IDs and rotation files from Merdith et al. (210), with modifications of Paleozoic terranes in Asia from Domeier (125) and Mesoproterozoic of Laurentia from Swanson-Hysell et al. (28). Petrology references are in Brown & Johnson (211).

Movie S1 (separate file). Provided in .mp4 format. The movie shows passive margin terminations over the past 1 billion years. Passive margins from **Datasets S3 and S5** are shown on a plate reconstruction in 5 Myr frames. Passive margin shapefiles used in the Supplementary Video are available in the **Dataset S4**. The Dupal formation interval (650-300 Ma) is indicated.

SI References

1. M. Jackson, T. Becker, B. Steinberger, Spatial characteristics of recycled and primordial reservoirs in the deep mantle. *Geochemistry, Geophysics, Geosystems* **22**, e2020GC009525 (2021).
2. M. Jackson, T. Becker, J. Konter, Geochemistry and distribution of recycled domains in the mantle inferred from Nd and Pb isotopes in oceanic hot spots: Implications for storage in the large low shear wave velocity provinces. *Geochemistry, Geophysics, Geosystems* **19**, 3496-3519 (2018).
3. S. R. Hart, A large-scale isotope anomaly in the Southern Hemisphere mantle. *Nature* **309**, 753-757 (1984).
4. S. Galer, R. O'nions, Residence time of thorium, uranium and lead in the mantle with implications for mantle convection. *Nature* **316**, 778-782 (1985).
5. B. Steinberger, R. J. O'Connell, Advection of plumes in mantle flow: implications for hotspot motion, mantle viscosity and plume distribution. *Geophysical Journal International* **132**, 412-434 (1998).
6. B. Steinberger, P. Nelson, S. Grand, W. Wang, Yellowstone plume conduit tilt caused by large-scale mantle flow. *Geochemistry, Geophysics, Geosystems* **20**, 5896-5912 (2019).
7. L. Boschi, T. W. Becker, B. Steinberger, On the statistical significance of correlations between synthetic mantle plumes and tomographic models. *Physics of the Earth and Planetary Interiors* **167**, 230-238 (2008).
8. S. W. French, B. Romanowicz, Broad plumes rooted at the base of the Earth's mantle beneath major hotspots. *Nature* **525**, 95-99 (2015).
9. J. Ritsema, a. A. Deuss, H. Van Heijst, J. Woodhouse, S40RTS: a degree-40 shear-velocity model for the mantle from new Rayleigh wave dispersion, teleseismic traveltime and normal-mode splitting function measurements. *Geophysical Journal International* **184**, 1223-1236 (2011).
10. M. Jackson, J. Konter, T. Becker, Primordial helium entrained by the hottest mantle plumes. *Nature* **542**, 340-343 (2017).
11. C. Lu, S. P. Grand, The effect of subducting slabs in global shear wave tomography. *Geophysical Journal International* **205**, 1074-1085 (2016).
12. T. M. Gibson *et al.*, Precise age of Bangiomorpha pubescens dates the origin of eukaryotic photosynthesis. *Geology* **46**, 135-138 (2017).
13. G. P. Halverson, F. A. Macdonald, J. V. Strauss, E. F. Smith, G. M. Cox, Updated definition and correlation of the lower Fifteenmile Group in the central and eastern Ogilvie Mountains. *Yukon Exploration Geology* **XX** (2012).
14. L. M. Heaman, A. N. LeCheminant, R. H. Rainbird, Nature and timing of Franklin igneous events, Canada: Implications for a Late Proterozoic mantle plume and the break-up of Laurentia. *Earth and Planetary Science Letters* **109**, 117-131 (1992).
15. K. Dewing, J. C. Harrison, B. R. Pratt, U. Mayr, A probable late Neoproterozoic age for the Kennedy Channel and Ella Bay formations, northeastern Ellesmere Island and its implications for passive margin history of the Canadian Arctic. *Canadian Journal of Earth Sciences* **41**, 1013-1025 (2004).

16. H. P. Trettin, "The Proterozoic to Late Silurian of Pearya, Chapter 9" in Geology of the Innuitian Orogen and Arctic Platform of Canada and Greenland*,* H. P. Trettin, Ed. (Geological Survey of Canada, 1991), vol. 3, pp. 241-259.
17. D. G. F. Long, Ella Bay Formation: Early Cambrian shelf differentiation in the Franklinian basin, central eastern Ellesmere Island, Arctic Canada. *Canadian Journal of Earth Sciences* **26**, 2621-2635 (1989).
18. F. Surlyk, J. M. Hurst, The evolution of the early Paleozoic deep-water basin of North Greenland. *Geological Society of America Bulletin* **95**, 131-154 (1984).
19. F. A. Macdonald *et al.*, Early Neoproterozoic Basin Formation in Yukon, Canada: Implications for the make-up and break-up of Rodinia. *Geoscience Canada* **39** (2012).
20. H. Zhao *et al.*, New geochronologic and paleomagnetic results from early Neoproterozoic mafic sills and late Mesoproterozoic to early Neoproterozoic successions in the eastern North China Craton, and implications for the reconstruction of Rodinia. *Bulletin* **132**, 739-766 (2020).
21. J. V. Strauss *et al.*, Orogen transplant: Taconic–Caledonian arc magmatism in the central Brooks Range of Alaska. *Bulletin* **129**, 649-676 (2017).
22. F. A. Macdonald, W. C. McClelland, D. P. Schrag, W. P. Macdonald, Neoproterozoic glaciation on a carbonate platform margin in Arctic Alaska and the origin of the North Slope subterrane. *Geological Society of America Bulletin* **121**, 448-473 (2009).
23. G. M. Cox *et al.*, Kikiktat volcanics of Arctic Alaska—Melting of harzburgitic mantle associated with the Franklin large igneous province. *Lithosphere* **7**, 275-295 (2015).
24. J. V. Strauss, F. Macdonald, W. C. McClelland, "Pre-Mississippian stratigraphy and provenance of the North Slope subterrane of Arctic Alaska I: Platformal carbonate rocks of the northeastern Brooks Range and their significance in circum-Arctic evolution" in Circum-Arctic Structural Events: Tectonic Evolution of the Arctic Margins and Trans-Arctic Links with Adjacent Orogens*,* K. Piepjohn, J. V. Strauss, L. Reinhardt, W. McClelland, Eds. (Geological Society of America Special Paper, 2018), vol. 541, pp. 493-524.
25. G. P. Halverson, A. C. Maloof, P. F. Hoffman, The Marinoan glaciation (Neoproterozoic) in northeast Svalbard. *Basin Research* **16**, 297-324 (2004).
26. A. C. Maloof, G. P. Halverson, J. L. Kirschvink, P. F. Hoffman, D. P. Schrag, Inertial interchange true polar wander: combined paleomagnetic, isotopic and stratigraphic evidence from the Neoproterozoic Akademikerbreen Group, Svalbard. *Geological Society of America Bulletin* **118**, 1099-1124 (2004).
27. D. G. Gee, H. Fossen, N. Henriksen, A. K. Higgins, From the early Paleozoic platforms of Baltica and Laurentia to the Caledonide Orogen of Scandinavia and Greenland. *Episodes* **31**, 44-51 (2008).
28. N. L. Swanson-Hysell, J. Ramezani, L. M. Fairchild, I. R. Rose, Failed rifting and fast drifting: Midcontinent rift development, Laurentia's rapid motion and the driver of Grenvillian orogenesis. *Geological Society of America Bulletin* **131**, 913-940 (2019).
29. B. Robert, M. Domeier, J. Jakob, Iapetan Oceans: An analog of Tethys? *Geology* **48**, 929-933 (2020).

30. C. Tegner *et al.*, A mantle plume origin for the Scandinavian Dyke Complex: a "piercing point" for 615 Ma plate reconstruction of Baltica? *Geochemistry, Geophysics, Geosystems* **20**, 1075-1094 (2019).
31. F. A. Macdonald *et al.*, Bridging the gap between the foreland and hinterland II: Geochronology and tectonic setting of Ordovician magmatism and basin formation on the Laurentian margin of New England and Newfoundland. *American Journal of Science* **317**, 555-596 (2017).
32. E. McClellan, E. J. L. Gazel, The Cryogenian intra-continental rifting of Rodinia: Evidence from the Laurentian margin in eastern North America. **206**, 321-337 (2014).
33. E. McClellan, E. Gazel, The Cryogenian intra-continental rifting of Rodinia: Evidence from the Laurentian margin in eastern North America. *Lithos* **206**, 321-337 (2014).
34. C. Ma, D. A. Foster, W. E. Hames, P. A. Mueller, M. G. Steltenpohl, From the Alleghanian to the Atlantic: Extensional collapse of the southernmost Appalachian orogen. *Geology* **47**, 367-370 (2019).
35. C. J. Spencer, A. R. Prave, P. A. Cawood, N. M. Roberts, Detrital zircon geochronology of the Grenville/Llano foreland and basal Sauk Sequence in west Texas, USA. *Geological Society of America Bulletin* **126**, 1117-1128 (2014).
36. C. J. Wall *et al.*, Integrating zircon trace-element geochemistry and high-precision U-Pb zircon geochronology to resolve the timing and petrogenesis of the late Ediacaran–Cambrian Wichita igneous province, Southern Oklahoma Aulacogen, USA. *Geology* (2020).
37. A. Piqué, J. W. Skehan, Late Paleozoic orogenies in western Africa and eastern North America: The diachronous closure of Theic Ocean. *Tectonics* **11**, 392-404 (1992).
38. J. D. Gleason, P. J. Patchett, W. R. Dickinson, J. Ruiz, Nd isotopic constraints on sediment sources of the Ouachita-Marathon fold belt. *Geological Society of America Bulletin* **107**, 1192-1210 (1995).
39. J. Wickham, D. Roeder, G. Briggs, Plate tectonics models for the Ouachita foldbelt. *Geology* **4**, 173-176 (1976).
40. D. P. Moynihan, J. V. Strauss, L. L. Nelson, C. D. Padget, Upper Windermere Supergroup and the transition from rifting to continent-margin sedimentation, Nadaleen River area, northern Canadian Cordillera. *Geological Society of America Bulletin* (2019).
41. G. C. Bond, M. A. Kominz, Construction of tectonic subsidence curves for the early Paleozoic miogeocline, southern Canadian Rocky Mountains; implications for subsidence mechanisms, age of breakup, and crustal thinning. *Geological Society of America Bulletin* **95**, 155-173 (1984).
42. M. Levy, N. Christie-Blick, Tectonic subsidence of the early Paleozoic passive continental margin in eastern California and southern Nevada. *Geological Society of America Bulletin* **103**, 1590-1606 (1991).
43. L. L. Nelson *et al.*, Geochronological constraints on Neoproterozoic rifting and onset of the Marinoan glaciation from the Kingston Peak Formation in Death Valley, California (USA). *Geology* (2020).

44. C. Dehler *et al.*, Synthesis of the 780–740 Ma Chuar, Uinta Mountain, and Pahrump (ChUMP) groups, western USA: implications for Laurentia-wide cratonic marine basins. *Geological Society of America Bulletin* **129**, 607-624 (2017).
45. J. V. Strauss *et al.*, Stratigraphic evolution of the Neoproterozoic Callison Lake Formation: linking the break-up of Rodinia to the Islay carbon isotope excursion. **315**, 881-944 (2015).
46. A. Eyster, F. Ferri, M. D. Schmitz, F. A. Macdonald, One diamictite and two rifts: Stratigraphy and geochronology of the Gataga Mountain of northern British Columbia. *American Journal of Science* **318**, 167-207 (2018).
47. F. A. Macdonald *et al.*, Cryogenian of Yukon. *Precambrian Research* **319**, 114-143 (2018).
48. F. A. Macdonald *et al.*, The Laurentian record of Neoproterozoic glaciation, tectonism, and eukaryotic evolution in Death Valley, California. *Geological Society of America Bulletin* **125**, 1203-1223 (2013).
49. E. C. Turner *et al.*, "Chapter 3. Stratigraphy" in Geology of the central Mackenzie Mountains of the northern Canadian Cordillera, Sekwi Mountain (105P), Mount Eduni (106A), and northwestern Wrigley Lake (95M) map-areas, Northwest Territories, E. Martel, E. C. Turner, B. J. Fischer, Eds. (NWT Geoscience Office, Yellowknife, 2011), vol. 1, pp. 31-192.
50. M. Colpron, J. M. Logan, J. K. Mortensen, U-Pb zircon age constraint for late Neoproterozoic rifting and initiation of the lower Paleozoic passive margin of western Laurentia. *Canadian Journal of Earth Sciences* **39**, 133-143 (2002).
51. F. A. Macdonald *et al.*, The stratigraphic relationship between the Shuram carbon isotope excursion, the oxygenation of Neoproterozoic oceans, and the first appearance of the Ediacara biota and bilaterian trace fossils in northwestern Canada. *Chemical Geology* **362**, 250-272 (2013).
52. J. H. Stewart, Upper Precambrian and Lower Cambrian strata in the southern Great Basin, California and Nevada. *U.S. Geological Survey Professional Paper* **620**, 206 (1970).
53. K. Karlstrom *et al.*, Cambrian Sauk transgression in the Grand Canyon region redefined by detrital zircons. *Nature Geoscience* **11**, 438 (2018).
54. M. T. Smith, W. R. Dickinson, G. Gehrels, Contractional nature of Devonian-Mississippian Antler tectonism along the North American continental margin. *Geology* **21**, 21-24 (1993).
55. D. C. Bradley, Passive Margins through Earth history. *Earth-Science Reviews* **91**, 1-26 (2008).
56. A. Parsons *et al.*, Petrogenesis of the Dunite Peak ophiolite, south-central Yukon, and the distinction between upper-plate and lower-plate settings: A new hypothesis for the late Paleozoic− early Mesozoic tectonic evolution of the Northern Cordillera. (2018).
57. J. Johnson, A. Pendergast, Timing and mode of emplacement of the Roberts Mountains allochthon, Antler orogeny. *Geological Society of America Bulletin* **92**, 648-658 (1981).
58. T. E. Moore *et al.*, "The geology of northern Alaska" in The geology of North America, Volume G-1, The geology of Alaska, G. Phlafker, H. C. Berg, Eds. (The Geological Society of America, Boulder, CO, 1994), pp. 49-140.

59. J. A. Dumoulin, A. G. Harris, C. D. Blome, L. E. Young, Depositional settings, correlation, and age of Carboniferous rocks in the western Brooks Range, Alaska. *Economic Geology* **99**, 1355-1384 (2004).
60. T. E. Moore, P. B. O'Sullivan, C. J. Potter, R. A. Donelick, Provenance and detrital zircon geochronologic evolution of lower Brookian foreland basin deposits of the western Brooks Range, Alaska, and implications for early Brookian tectonism. *Geosphere* **11**, 93-122 (2015).
61. O. Svenningsen, Onset of seafloor spreading in the Iapetus Ocean at 608 Ma: precise age of the Sarek Dyke Swarm, northern Swedish Caledonides. *Precambrian Research* **110**, 241-254 (2001).
62. D. Roberts, The Scandinavian Caledonides: event chronology, palaeogeographic settings and likely modern analogues. *Tectonophysics* **365**, 283-299 (2003).
63. V. Pease *et al.*, Baltica in the Cryogenian, 850–630 Ma. *Precambrian Research* **160**, 46-65 (2008).
64. A. Kuznetsov, A. Bekker, G. Ovchinnikova, I. Gorokhov, I. Vasilyeva, Unradiogenic strontium and moderate-amplitude carbon isotope variations in early Tonian seawater after the assembly of Rodinia and before the Bitter Springs Excursion. *Precambrian Research* **298**, 157-173 (2017).
65. M. A. Pulsipher, C. M. Dehler, U-Pb detrital zircon geochronology, petrography, and synthesis of the middle Neoproterozoic Visingsö Group, Southern Sweden. *Precambrian Research* **320**, 323-333 (2019).
66. E. V. Khain *et al.*, The Palaeo-Asian ocean in the Neoproterozoic and early Palaeozoic: new geochronologic data and palaeotectonic reconstructions. *Precambrian Research* **122**, 329-358 (2003).
67. A. P. Willner, M. Gopon, J. Glodny, V. N. Puchkov, H.-P. Schertl, Timanide (Ediacaran-Early Cambrian) Metamorphism at the Transition from Eclogite to Amphibolite Facies in the Beloretsk Complex, SW-Urals, Russia. *Journal of Earth Science* **30**, 1144-1165 (2019).
68. D. Brown *et al.*, Arc–continent collision in the Southern Urals. *Earth-Science Reviews* **79**, 261-287 (2006).
69. P. Spadea, M. D'Antonio, Initiation and evolution of intra-oceanic subduction in the Uralides: Geochemical and isotopic constraints from Devonian oceanic rocks of the Southern Urals, Russia. *Island Arc* **15**, 7-25 (2006).
70. L. Zonenshain *et al.*, Plate tectonic model of the South Urals development. *Tectonophysics* **109**, 95-135 (1984).
71. A. J. Newell, V. P. Tverdokhlebov, M. J. Benton, Interplay of tectonics and climate on a transverse fluvial system, Upper Permian, Southern Uralian Foreland Basin, Russia. *Sedimentary Geology* **127**, 11-29 (1999).
72. P. Krzywiec, P. Poprawa, M. Mikołajczak, S. Mazur, M. Malinowski, Deeply concealed half-graben at the SW margin of the East European Craton (SE Poland)—Evidence for Neoproterozoic rifting prior to the break-up of Rodinia. *Journal of Palaeogeography* **7**, 88-97 (2018).
73. T. H. Torsvik, E. F. Rehnström, The Tornquist Sea and Baltica–Avalonia docking. *Tectonophysics* **362**, 67-82 (2003).

74. T. Pharaoh, J. Winchester, J. Verniers, A. Lassen, A. Seghedi, The western accretionary margin of the East European Craton: an overview. *Memoirs-Geological Society of London* **32**, 291 (2006).
75. M. D. Thompson, J. L. Crowley, Avalonian arc-to-platform transition in southeastern New England: U-Pb geochronology and stratigraphy of Ediacaran Cambridge “argillite,” Boston Basin, Massachusetts, USA. *American Journal of Science* **320**, 405-449 (2020).
76. E. Landing, R. Nance, M. Thompson, Avalon: Insular continent by the latest Precambrian. *Geological Society of America Special Papers*, 29-64 (1996).
77. C. R. van Staal, S. M. Barr, J. Percival, Lithospheric architecture and tectonic evolution of the Canadian Appalachians and associated Atlantic margin. *Tectonic styles in Canada: the LITHOPROBE perspective. Edited by JA Percival, FA Cook, and RM Clowes. Geological Association of Canada, Special Paper* **49** (2012).
78. A. J. Hartley, J. Otava, Sediment provenance and dispersal in a deep marine foreland basin: the Lower Carboniferous Culm Basin, Czech Republic. *Journal of the Geological Society* **158**, 137-150 (2001).
79. R. Gayer, J. Jones, The Variscan foreland in South Wales. *Proceedings of the Ussher Society* **7**, 177-179 (1989).
80. A. Schäfer, Variscan molasse in the Saar-Nahe Basin (W-Germany), Upper Carboniferous and Lower Permian. *Geologische Rundschau* **78**, 499-524 (1989).
81. M. Narkiewicz, Development and inversion of Devonian and Carboniferous basins in the eastern part of the Variscan foreland (Poland). *Geological Quarterly* **51**, 231-256 (2010).
82. U. Kroner, R. Romer, Two plates—many subduction zones: the Variscan orogeny reconsidered. *Gondwana Research* **24**, 298-329 (2013).
83. U. Linnemann *et al.*, West African provenance for Saxo-Thuringia (Bohemian Massif): did Armorica ever leave pre-Pangean Gondwana?–U/Pb-SHRIMP zircon evidence and the Nd-isotopic record. *International Journal of Earth Sciences* **93**, 683-705 (2004).
84. P. A. Ziegler, S. Cloetingh, R. Guiraud, G. M. Stampfli, Peri-Tethyan platforms: constraints on dynamics of rifting and basin inversion. *Mémoires du Muséum national d'histoire naturelle (1993)* **186**, 9-49 (2001).
85. H. Furnes, M. De Wit, Y. Dilek, Four billion years of ophiolites reveal secular trends in oceanic crust formation. *Geoscience Frontiers* **5**, 571-603 (2014).
86. A. Michard, A. Chalouan, H. Feinberg, B. Goffé, R. Montigny, How does the Alpine belt end between Spain and Morocco? *Bulletin de la Société géologique de France* **173**, 3-15 (2002).
87. E. G. Clavijo, J. M. Catalán, Stratigraphic record of preorogenic to synorogenic sedimentation, and tectonic evolution of imbricate units in the Alcañices synform (northwestern Iberian Massif). *Geological Society of America Special Paper*, 17-36 (2002).
88. P. Degnan, A. Robertson, Mesozoic-early Tertiary passive margin evolution of the Pindos ocean (NW Peloponnese, Greece). *Sedimentary Geology* **117**, 33-70 (1998).
89. E. Bozkurt, J. A. Winchester, M. Satır, The Çele mafic complex: evidence for Triassic collision between the Sakarya and İstanbul Zones, NW Turkey. *Tectonophysics* **595**, 198-214 (2013).

90. A. I. Okay, O. Tüysüz, Tethyan sutures of northern Turkey. *Geological Society, London, Special Publications* **156**, 475-515 (1999).
91. M. Rioux *et al.*, Synchronous formation of the metamorphic sole and igneous crust of the Semail ophiolite: New constraints on the tectonic evolution during ophiolite formation from high-precision U–Pb zircon geochronology. *Earth and Planetary Science Letters* **451**, 185-195 (2016).
92. A. C. Şengör, J. Stock, The Ayyubid Orogen: An ophiolite obduction-driven orogen in the late Cretaceous of the Neo-Tethyan south margin. *Geoscience Canada* **41**, 225-254 (2014).
93. H. S. Moghadam, R. J. Stern, Ophiolites of Iran: Keys to understanding the tectonic evolution of SW Asia:(II) Mesozoic ophiolites. *Journal of Asian Earth Sciences* **100**, 31-59 (2015).
94. R. Tirrul, I. Bell, R. Griffis, V. Camp, The Sistan suture zone of eastern Iran. *Geological Society of America Bulletin* **94**, 134-150 (1983).
95. M. Wilmsen, F. T. Fürsich, K. Seyed-Emami, M. R. Majidifard, J. Taheri, The Cimmerian Orogeny in northern Iran: Tectono-stratigraphic evidence from the foreland. *Terra Nova* **21**, 211-218 (2009).
96. P. M. Myrow *et al.*, Cambrian–Ordovician orogenesis in Himalayan equatorial Gondwana. *Geological Society of America Bulletin* **128**, 1679-1695 (2016).
97. P. Bouilhol, O. Jagoutz, J. M. Hanchar, F. O. Dudas, Dating the India–Eurasia collision through arc magmatic records. *Earth and Planetary Science Letters* **366**, 163-175 (2013).
98. L. Ding *et al.*, The India–Asia collision in north Pakistan: Insight from the U–Pb detrital zircon provenance of Cenozoic foreland basin. *Earth and Planetary Science Letters* **455**, 49-61 (2016).
99. C. R. Martin *et al.*, Paleocene latitude of the Kohistan–Ladakh arc indicates multistage India–Eurasia collision. *Proceedings of the National Academy of Sciences* **117**, 29487-29494 (2020).
100. O. Jagoutz, L. Royden, A. F. Holt, T. W. Becker, Anomalously fast convergence of India and Eurasia caused by double subduction. *Nature Geoscience* **8**, 475 (2015).
101. T. N. Yang, Z. Q. Hou, Y. Wang, H. R. Zhang, Z. L. Wang, Late Paleozoic to Early Mesozoic tectonic evolution of northeast Tibet: Evidence from the Triassic composite western Jinsha-Garzê-Litang suture. *Tectonics* **31** (2012).
102. E. Enkelmann *et al.*, How was the Triassic Songpan-Ganzi basin filled? A provenance study. *Tectonics* **26** (2007).
103. V. Vernikovsky, A. Vernikovskaya, Central Taimyr accretionary belt (Arctic Asia): Meso–Neoproterozoic tectonic evolution and Rodinia breakup. *Precambrian Research* **110**, 127-141 (2001).
104. N. Priyatkina *et al.*, The Proterozoic evolution of northern Siberian Craton margin: a comparison of U–Pb–Hf signatures from sedimentary units of the Taimyr orogenic belt and the Siberian platform. *International Geology Review* **59**, 1632-1656 (2017).
105. S. M. Pelechaty, J. P. Grotzinger, V. A. Kashirtsev, V. P. Zhernovsky, Chemostratigraphic and Sequence Stratigraphic Constraints on Vendian-Cambrian

Basin Dynamics, Northeast Siberian Craton. *Journal of Geology* **104**, 543-563 (1996).
106. L. P. Zonenshain, M. I. Kuzmin, L. M. Natapov, *Geology of the USSR: a Plate-Tectonic Synthesis*, American Geophysical Union Geodynamical Series, 21 (1990), vol. 21, pp. 242.
107. M. Kurapov *et al.*, Late Palaeozoic magmatism of Northern Taimyr: new insights into the tectonic evolution of the Russian High Arctic. *International Geology Review*, 1-23 (2020).
108. A. Kuznetsov, B. Kochnev, I. Vasilyeva, G. Ovchinnikova, The Upper Riphean of the Yenisei Range: Sr Chemostratigraphy and Pb–Pb Age of Limestones of the Tungusik and Shirokaya Groups. *Stratigraphy and Geological Correlation* **27**, 538-554 (2019).
109. A. B. Kuzmichev, E. V. Sklyarov, The Precambrian of Transangaria, Yenisei Ridge (Siberia): Neoproterozoic microcontinent, Grenville-age orogen, or reworked margin of the Siberian craton? *Journal of Asian Earth Sciences* **115**, 419-441 (2016).
110. I. Likhanov, M. Santosh, Neoproterozoic intraplate magmatism along the western margin of the Siberian Craton: Implications for breakup of the Rodinia supercontinent. *Precambrian Research* **300**, 315-331 (2017).
111. N. Kuznetsov *et al.*, Sturtian Glaciation in Siberia: Evidence of Glacial Origin and U-Pb Dating of the Diamictites of the Chivida Formation in the North of the Yenisei Ridge. *Precambrian Research*, 105778 (2020).
112. V. A. Vernikovsky, A. Vernikovskaya, A. Kotov, E. Sal'nikova, V. Kovach, Neoproterozoic accretionary and collisional events on the western margin of the Siberian craton: new geological and geochronological evidence from the Yenisey Ridge. *Tectonophysics* **375**, 147-168 (2003).
113. A. Ariskin *et al.*, The Dovyren Intrusive Complex (Southern Siberia, Russia): Insights into dynamics of an open magma chamber with implications for parental magma origin, composition, and Cu-Ni-PGE fertility. *Lithos* **302**, 242-262 (2018).
114. V. Powerman, A. Shatsillo, N. Chumakov, I. Kapitonov, J. Hourigan, Interaction between the Central Asian Orogenic Belt (CAOB) and the Siberian craton as recorded by detrital zircon suites from Transbaikalia. *Precambrian Research* **267**, 39-71 (2015).
115. S. M. Pelechaty, Stratigraphic evidence for the Siberia-Laurentia connection and Early Cambrian rifting. *Geology* **24**, 719-722 (1996).
116. V. S. Oxman, Tectonic evolution of the Mesozoic Verkhoyansk–Kolyma belt (NE Asia). *Tectonophysics* **365**, 45-76 (2003).
117. U. Bold, J. L. Crowley, E. F. Smith, O. Sambuu, F. A. Macdonald, Neoproterozoic to early Paleozoic tectonic evolution of the Zavkhan terrane of Mongolia: Implications for continental growth in the Central Asian orogenic belt. *Lithosphere* **8**, 729-750 (2016).
118. E. F. Smith, F. A. Macdonald, T. A. Petach, U. Bold, D. P. Schrag, Integrated stratigraphic, geochemical, and paleontological late Ediacaran to early Cambrian records from southwestern Mongolia. *Bulletin* **128**, 442-468 (2015).

119. G. Badarch, W. D. Cunningham, B. Windley, A new terrane subdivision for Mongolia: implications for the Phanerozoic crustal growth of Central Asia. *Journal of Asian Earth Sciences* **21**, 87-110 (2002).
120. B. Xu, Xiao S. Zou H.-B. Chen Y. Li Z.-X. Song B. Liu D.-Y. Zhou C.-M. Yuan X.-L., SHRIMP zircon U-Pb age constraints on Neoproterozoic Quruqtah diamictites in NW China. *Precambrian Research* **168**, 247-258 (2009).
121. R. Ge *et al.*, Neoproterozoic to Paleozoic long-lived accretionary orogeny in the northern Tarim Craton. *Tectonics* **33**, 302-329 (2014).
122. A. R. Carroll, S. A. Graham, E. Z. Chang, C. McKnight, Sinian through Permian tectonostratigraphic evolution of the northwestern Tarim basin, China. *Memoirs-Geological Society of America*, 47-70 (2001).
123. B. Wang *et al.*, Paleozoic tectonics of the southern Chinese Tianshan: insights from structural, chronological and geochemical studies of the Heiyingshan ophiolitic mélange (NW China). **497**, 85-104 (2011).
124. H. Liu, I. D. Somerville, C. Lin, S. Zuo, Distribution of Palaeozoic tectonic superimposed unconformities in the Tarim Basin, NW China: significance for the evolution of palaeogeomorphology and sedimentary response. *Geological Journal* **51**, 627-651 (2016).
125. M. Domeier, Early Paleozoic tectonics of Asia: towards a full-plate model. *Geoscience Frontiers* **9**, 789-862 (2018).
126. S. Xiao *et al.*, Biostratigraphic and chemostratigraphic constraints on the age of early Neoproterozoic carbonate successions in North China. *Precambrian Research* **246**, 208-225 (2014).
127. P. M. Myrow *et al.*, Depositional history, tectonics, and provenance of the Cambrian-Ordovician boundary interval in the western margin of the North China block. *Bulletin* **127**, 1174-1193 (2015).
128. L. Ratschbacher *et al.*, Tectonics of the Qinling (Central China): tectonostratigraphy, geochronology, and deformation history. *Tectonophysics* **366**, 1-53 (2003).
129. B. Burchfiel, C. Zhiliang, L. Yupinc, L. Royden, Tectonics of the Longmen Shan and adjacent regions, central China. *International Geology Review* **37**, 661-735 (1995).
130. B. R. Hacker, L. Ratschbacher, J. Liou, Subduction, collision and exhumation in the ultrahigh-pressure Qinling-Dabie orogen. *Geological Society, London, Special Publications* **226**, 157-175 (2004).
131. J.-H. Ree, M. Cho, S.-T. Kwon, E. Nakamura, Possible eastward extension of Chinese collision belt in South Korea: the Imjingang belt. *Geology* **24**, 1071-1074 (1996).
132. X. Yang *et al.*, The depositional mechanism of organic-rich siliceous shales in Upper Yangtze area: Response to the Kwangsian Orogeny in South China. *Journal of Petroleum Science and Engineering*, 107310 (2020).
133. Y.-J. Xu, P. A. Cawood, Y.-S. Du, Intraplate orogenesis in response to Gondwana assembly: Kwangsian orogeny, South China. *American Journal of Science* **316**, 329-362 (2016).
134. T. Byrne *et al.*, "The arc–continent collision in Taiwan" in Arc-Continent Collision. (Springer, 2011), pp. 213-245.

135. R. Harris, Rise and fall of the Eastern Great Indonesian arc recorded by the assembly, dispersion and accretion of the Banda Terrane, Timor. *Gondwana Research* **10**, 207-231 (2006).
136. A. Q. van Ufford, M. Cloos, Cenozoic tectonics of New Guinea. *AAPG bulletin* **89**, 119-140 (2005).
137. S. L. Baldwin, P. G. Fitzgerald, L. E. Webb, Tectonics of the New Guinea region. *Annual Review of Earth and Planetary Sciences* **40** (2012).
138. W. B. Hamilton, *Tectonics of the Indonesian region* (US Govt. Print. Off., 1979).
139. M. Cloos *et al.*, Collisional delamination in New Guinea: The geotectonics of subducting slab breakoff. *Geological Society of America Special Papers* **400**, 1-51 (2005).
140. H. L. Davies, I. E. Smith, Geology of eastern Papua. *Geological Society of America Bulletin* **82**, 3299-3312 (1971).
141. H. Davies, A. Jaques, Emplacement of ophiolite in Papua New Guinea. *Geological Society, London, Special Publications* **13**, 341-349 (1984).
142. D. C. Greene, Neoproterozoic rifting in the southern Georgina Basin, central Australia: Implications for reconstructing Australia in Rodinia. *Tectonics* **29** (2010).
143. W. V. Preiss, The Adelaide Geosyncline: Late Proterozoic stratigraphy, sedimentation, paleontology and tectonics. *Geological Survey of South Australia Bulletin* **53**, 438 (1987).
144. P. Haines *et al.*, Tracking sediment dispersal during orogenesis: A zircon age and Hf isotope study from the western Amadeus Basin, Australia. *Gondwana Research* **37**, 324-347 (2016).
145. E. L. Martin, W. J. Collins, C. L. Kirkland, An Australian source for Pacific-Gondwanan zircons: Implications for the assembly of northeastern Gondwana. *Geology* **45**, 699-702 (2017).
146. W. Preiss, The Adelaide Geosyncline of South Australia and its significance in Neoproterozoic continental reconstruction. *Precambrian Research* **100**, 21-63 (2000).
147. J. Foden, M. A. Elburg, J. Dougherty-Page, A. Burtt, The timing and duration of the Delamerian Orogeny: correlation with the Ross Orogen and implications for Gondwana assembly. *The Journal of Geology* **114**, 189-210 (2006).
148. C. R. Calver, Isotope stratigraphy of the Neoproterozoic Togari Group, Tasmania. *Australian Journal of Earth Sciences* **45**, 865-874 (1998).
149. C. R. Calver, L. P. Black, J. L. Everard, D. B. Seymour, U-Pb zircon age constraints on late Neoproterozoic glaciation in Tasmania. *Geology* **32**, 893-896 (2004).
150. G. Hagen-Peter, J. Cottle, M. Smit, A. Cooper, Coupled garnet Lu–Hf and monazite U–Pb geochronology constrain early convergent margin dynamics in the Ross orogen, Antarctica. *Journal of Metamorphic Geology* **34**, 293-319 (2016).
151. A. J. Crawford, R. F. Berry, Tectonic implications of Late Proterozoic-Early Palaeozoic igneous rock associations in western Tasmania. *Tectonophysics* **214**, 37-56 (1992).
152. C. Lázaro *et al.*, Fifty-five-million-year history of oceanic subduction and exhumation at the northern edge of the Caribbean plate (Sierra del Convento mélange, Cuba). *Journal of metamorphic Geology* **27**, 19-40 (2009).

153. J. P. Erikson, J. L. Pindell, Analysis of subsidence in northeastern Venezuela as a discriminator of tectonic models for northern South America. *Geology* **21**, 945-948 (1993).
154. R. da Silva Schmitt, R. de Araújo Fragoso, A. S. Collins, "Suturing Gondwana in the Cambrian: the orogenic events of the final amalgamation" in Geology of Southwest Gondwana. (Springer, 2018), pp. 411-432.
155. W. Cao, C.-T. A. Lee, J. S. Lackey, Episodic nature of continental arc activity since 750 Ma: A global compilation. *Earth and Planetary Science Letters* **461**, 85-95 (2017).
156. U. G. Cordani, W. Teixeira, Proterozoic accretionary belts in the Amazonian Craton. *Geological Society of America Memoirs* **200**, 297-320 (2007).
157. C. J. S. d. Alvarenga *et al.*, Isotope stratigraphy of Neoproterozoic cap carbonates in the Araras Group, Brazil. *Gondwana Research* **13**, 469-479 (2008).
158. M. Babinski *et al.* (2008) U-Pb shrimp geochronology and isotope chemostratigraphy (C, O, Sr) of the Tamengo Formation, southern Paraguay belt, Brazil. in *South American Symposium on Isotope Geology* (San Carlos de Bariloche Argentina).
159. B. McGee, A. S. Collins, R. I. Trindade, J. Payne, Age and provenance of the Cryogenian to Cambrian passive margin to foreland basin sequence of the northern Paraguay Belt, Brazil. *Bulletin* **127**, 76-86 (2015).
160. E. B. Hodgin *et al.*, Cannibalization of a late Cambrian backarc in southern Peru: New insights into the assembly of southwestern Gondwana. *Gondwana Research* **92**, 202-227 (2021).
161. A. Mišković *et al.*, Tectonomagmatic evolution of Western Amazonia: Geochemical characterization and zircon U-Pb geochronologic constraints from the Peruvian Eastern Cordilleran granitoids. *Geological Society of America Bulletin* **121**, 1298-1324 (2009).
162. W. A. Thomas, R. A. Astini, Ordovician accretion of the Argentine Precordillera terrane to Gondwana: a review. *Journal of South American Earth Sciences* **16**, 67-79 (2003).
163. M. T. Brown, R. A. Fuck, E. L. Dantas, Isotopic age constraints and geochemical results of disseminated ophiolitic assemblage from Neoproterozoic mélange, central Brazil. *Precambrian Research* **339**, 105581 (2020).
164. M. Babinski, L. C. Vieira, R. I. Trindade, Direct dating of the Sete Lagoas cap carbonate (Bambuí Group, Brazil) and implications for the Neoproterozoic glacial events. *Terra Nova* **19**, 401-406 (2007).
165. J. H. Laux, M. M. Pimentel, E. L. Dantas, R. Armstrong, S. L. Junges, Two Neoproterozoic crustal accretion events in the Brasília belt, central Brazil. *Journal of South American Earth Sciences* **18**, 183-198 (2005).
166. M. M. Pimentel, C. F. Ferreira Filho, A. Armele, Neoproterozoic age of the Niquelândia Complex, central Brazil: further ID-TIMS U–Pb and Sm–Nd isotopic evidence. *Journal of South American Earth Sciences* **21**, 228-238 (2006).
167. C. E. G. De Araujo *et al.*, Ediacaran 2,500-km-long synchronous deep continental subduction in the West Gondwana Orogen. *Nature communications* **5**, 1-8 (2014).
168. M. Heilbron *et al.*, "The Ribeira Belt" in São Francisco Craton, Eastern Brazil. (Springer, 2017), pp. 277-302.

169. B. D. Goscombe, D. R. Gray, Structure and strain variation at mid-crustal levels in a transpressional orogen: a review of Kaoko Belt structure and the character of West Gondwana amalgamation and dispersal. *Gondwana Research* **13**, 45-85 (2008).
170. R. Shone, P. Booth, The Cape Basin, South Africa: A review. *Journal of African Earth Sciences* **43**, 196-210 (2005).
171. O. Catuneanu *et al.*, The Karoo basins of south-central Africa. *Journal of African Earth Sciences* **43**, 211-253 (2005).
172. S. M. Porter, A. H. Knoll, P. Affaton, Chemostratigraphy of Neoproterozoic cap carbonates from the Volta basin, West Africa. *Precambrian Research* **130**, 99-112 (2004).
173. R. Caby, U. Andreopoulos-Renaud, C. Pin, Late Proterozoic arc–continent and continent–continent collision in the Pan-African Trans-Saharan Belt of Mali. *Canadian Journal of Earth Sciences* **26**, 1136-1146 (1989).
174. R. Caby, Terrane assembly and geodynamic evolution of central–western Hoggar: a synthesis. *Journal of African Earth Sciences* **37**, 133-159 (2003).
175. C. E. Ganade *et al.*, Tightening-up NE Brazil and NW Africa connections: New U–Pb/Lu–Hf zircon data of a complete plate tectonic cycle in the Dahomey belt of the West Gondwana Orogen in Togo and Benin. *Precambrian Research* **276**, 24-42 (2016).
176. J. N. Carney *et al.*, Lithostratigraphy, sedimentation and evolution of the Volta Basin in Ghana. *Precambrian Research* **183**, 701-724 (2010).
177. K. Attoh, F. Corfu, P. M. Nude, U-Pb zircon age of deformed carbonatite and alkaline rocks in the Pan-African Dahomeyide suture zone, West Africa. *Precambrian Research* **155**, 251-260 (2007).
178. R. J. Thomas *et al.*, A new lithostratigraphic framework for the Anti-Atlas Orogen, Morocco. *Journal of African Earth Sciences* **39**, 217-226 (2004).
179. E. H. Bouougri *et al.*, Time constraints on Early Tonian Rifting and Cryogenian Arc terrane-continent convergence along the northern margin of the West African craton: Insights from SHRIMP and LA-ICP-MS zircon geochronology in the Pan-African Anti-Atlas belt (Morocco). *Gondwana Research* (2020).
180. J. J. Álvaro *et al.*, Early Neoproterozoic rift-related magmatism in the Anti-Atlas margin of the West African craton, Morocco. *Precambrian Research* **255**, 433-442 (2014).
181. F. Hodel *et al.*, The moroccan Anti-Atlas ophiolites: Timing and melting processes in an intra-oceanic arc-back-arc environment. *Gondwana Research* (2020).
182. S. Samson *et al.*, Geochronological, geochemical, and Nd–Hf isotopic constraints on the origin of Neoproterozoic plagiogranites in the Tasriwine ophiolite, Anti-Atlas orogen, Morocco. *Precambrian Research* **135**, 133-147 (2004).
183. A. Triantafyllou *et al.*, Episodic magmatism during the growth of a Neoproterozoic oceanic arc (Anti-Atlas, Morocco). *Precambrian Research* **339**, 105610 (2020).
184. U. Linnemann, A. Gerdes, M. Hofmann, L. Marko, The Cadomian Orogen: Neoproterozoic to Early Cambrian crustal growth and orogenic zoning along the periphery of the West African Craton—Constraints from U–Pb zircon ages and Hf isotopes (Schwarzburg Antiform, Germany). *Precambrian Research* **244**, 236-278 (2014).

185. A. D. Rooney, D. Selby, J.-P. Houzay, P. R. Renne, Re–Os geochronology of a Mesoproterozoic sedimentary succession, Taoudeni basin, Mauritania: Implications for basin-wide correlations and Re–Os organic-rich sediments systematics. *Earth and Planetary Science Letters* **289**, 486-496 (2010).
186. D. C. Bradley *et al.* (2015) Synthesis of geological, structural, and geochronologic data (phase V, deliverable 53): Chapter A in Second projet de renforcement institutionnel du secteur minier de la République Islamique de Mauritanie (PRISM-II). (US Geological Survey).
187. R. Dallmeyer, J. Lécorché, $^{40}Ar/^{39}Ar$ polyorogenic mineral age record within the central Mauritanide orogen, West Africa. *Geological Society of America Bulletin* **101**, 55-70 (1989).
188. M. Villeneuve, Review of the orogenic belts on the western side of the West African craton: the Bassarides, Rokelides and Mauritanides. *Geological Society, London, Special Publications* **297**, 169-201 (2008).
189. M. Villeneuve, H. Bellon, M. Corsini, J. Le Metour, S. Chatelee, New investigations in southwestern Guinea: consequences for the Rokelide belt (West Africa). *International Journal of Earth Sciences* **104**, 1267-1275 (2015).
190. P. F. Hoffman, F. A. Macdonald, G. P. Halverson, Chemical sediments associated with Neoproterozoic glaciation: iron formation, cap carbonate, barite and phosphorite. *Geological Society, London, Memoirs* **36**, 67-80 (2011).
191. A. Gärtner *et al.*, History of the west African Neoproterozoic ocean: key to the geotectonic history of circum-Atlantic peri-Gondwana (Adrar Souttouf massif, Moroccan Sahara). *Gondwana Research* **29**, 220-233 (2016).
192. J. Tchakounté *et al.*, The Adamawa-Yadé domain, a piece of Archaean crust in the Neoproterozoic central African orogenic belt (Bafia area, Cameroon). *Precambrian Research* **299**, 210-229 (2017).
193. I. P. Guimarães *et al.*, U–Pb zircon ages of orthogneisses and supracrustal rocks of the Cariris Velhos belt: onset of Neoproterozoic rifting in the Borborema Province, NE Brazil. *Precambrian Research* **192**, 52-77 (2012).
194. E. P. Oliveira, B. F. Windley, M. N. Araújo, The Neoproterozoic Sergipano orogenic belt, NE Brazil: a complete plate tectonic cycle in western Gondwana. *Precambrian Research* **181**, 64-84 (2010).
195. V. Caron, G. Mahieux, E. Ekomane, P. Moussango, M. Babinski, One, two or no record of late neoproterozoic glaciation in South-East Cameroon? *Journal of African Earth Sciences* **59**, 111-124 (2011).
196. F. Caxito, A. Uhlein, R. Stevenson, G. J. Uhlein, Neoproterozoic oceanic crust remnants in northeast Brazil. *Geology* **42**, 387-390 (2014).
197. A. N. Sial *et al.*, C-, Sr-isotope and Hg chemostratigraphy of Neoproterozoic cap carbonates of the Sergipano Belt, Northeastern Brazil. *Precambrian Research* **182**, 351-372 (2010).
198. W. Van Schmus, M. Kozuch, B. de Brito Neves, Precambrian history of the Zona Transversal of the Borborema Province, NE Brazil: insights from Sm–Nd and U–Pb geochronology. *Journal of South American Earth Sciences* **31**, 227-252 (2011).
199. E. Oliveira *et al.*, Geologic correlation between the Neoproterozoic Sergipano belt (NE Brazil) and the Yaoundé belt (Cameroon, Africa). *Journal of African Earth Sciences* **44**, 470-478 (2006).

200. P. F. Hoffman, Cusp tectonics: an Ediacaran megakarst landscape and bidirectional mass slides in a Pan-African syntaxis (NW Namibia). *Geological Society, London, Special Publications* **503** (2020).
201. B. Goscombe, M. Hand, D. Gray, J. Mawby, The metamorphic architecture of a transpressional orogen: the Kaoko Belt, Namibia. *Journal of Petrology* **44**, 679-711 (2003).
202. B. Goscombe, D. A. Foster, D. Gray, B. Wade, Assembly of central Gondwana along the Zambezi Belt: Metamorphic response and basement reactivation during the Kuunga Orogeny. *Gondwana Research* (2019).
203. T. John, V. Schenk, K. Mezger, F. Tembo, Timing and PT evolution of whiteschist metamorphism in the Lufilian Arc–Zambezi Belt orogen (Zambia): implications for the assembly of Gondwana. *The Journal of geology* **112**, 71-90 (2004).
204. A. B. Westerhof *et al.*, *Geology and geodynamic development of Uganda with explanation of the 1: 1,000,000 scale geological map* (Geological survey of Finland, 2014).
205. R. L. Rudnick, D. M. Fountain, Nature and composition of the continental crust: a lower crustal perspective. *Reviews of geophysics* **33**, 267-309 (1995).
206. Y. Huang, V. Chubakov, F. Mantovani, R. L. Rudnick, W. F. McDonough, A reference Earth model for the heat-producing elements and associated geoneutrino flux. *Geochemistry, Geophysics, Geosystems* **14**, 2003-2029 (2013).
207. W. F. McDonough, S.-S. Sun, The composition of the Earth. *Chemical geology* **120**, 223-253 (1995).
208. M. Willbold, A. Stracke, Formation of enriched mantle components by recycling of upper and lower continental crust. *Chemical Geology* **276**, 188-197 (2010).
209. T. H. Torsvik, L. R. M. Cocks, *Earth history and palaeogeography* (Cambridge University Press, 2017).
210. A. S. Merdith *et al.*, Extending full-plate tectonic models into deep time: Linking the Neoproterozoic and the Phanerozoic. *Earth-Science Reviews*, 103477 (2020).
211. M. Brown, T. Johnson, Metamorphism and the evolution of subduction on Earth. *American Mineralogist: Journal of Earth and Planetary Materials* **104**, 1065-1082 (2019).
212. A. Eyster, B. P. Weiss, K. Karlstrom, F. A. Macdonald, Paleomagnetism of the Chuar Group and evaluation of the late Tonian Laurentian apparent polar wander path with implications for the makeup and breakup of Rodinia. *Bulletin* **132**, 710-738 (2020).
213. T. H. Torsvik *et al.*, Connecting the deep Earth and the atmosphere. *Mantle Convection and Surface Expressions*, 413-453 (2021).